Charge symmetry breaking in ΛN interaction studied via the γ-ray spectroscopy of ${}^{4}_{\Lambda}$He

A dissertation

by

TAKESHI YAMAMOTO

Submitted to
Department of Physics, Tohoku University
in partial fulfillment of the requirements
for the degree of Doctor of Science

January, 2016

Abstract

A gamma-ray spectroscopy study of ${}^{4}_{\Lambda}$He was performed at the J-PARC K1.8 beam line as the first phase of the J-PARC E13 experiment. By measuring the ${}^{4}_{\Lambda}\mathrm{He}(1^+ \to 0^+)$ gamma transition, we can examine the existence of charge symmetry breaking(CSB) in ΛN interaction by comparing with the mirror hypernucleus, ${}^{4}_{\Lambda}$H. The old experiments suggested large differences in the excitation energies ($E(1^+)-E(0^+)$) as well as the g.s. Λ-binding energies ($B_\Lambda(0^+)$) between the mirror hypernuclei, leading to unexpectedly large CSB in ΛN interaction. However, statistical quality for the ${}^{4}_{\Lambda}\mathrm{He}$ $(1^+ \to 0^+)$ gamma-ray data in the past experiment is insufficient to confirm the existence of a large CSB, and thus more precise measurement of the energy spacing was long awaited. In order to break through this situation, we performed a gamma-ray spectroscopy experiment of ${}^{4}_{\Lambda}$He to measure the transition energy of the Λ-spin doublet states $(1^+, 0^+)$ using germanium(Ge) detectors with an energy resolution of 5 keV.

${}^{4}_{\Lambda}$He hypernuclei were produced by the (K^-, π^-) reaction with a 1.5 GeV/c kaon beam and a liquid ^{4}He target. K^- beams and scattered π^- mesons were particle-identified and momentum-analyzed by the beam line spectrometer and the modified SKS spectrometer (SksMinus), respectively. On the other hand, gamma rays were detected by a newly developed Ge detector array, Hyperball-J, placed around the target. Through coincidence measurement between these spectrometer systems and Hyperball-J, gamma rays from ${}^{4}_{\Lambda}$He hypernuclei were measured.

The J-PARC E13 experiment clearly identified a γ-ray transition from ${}^{4}_{\Lambda}$He produced by the ${}^{4}\mathrm{He}(K^-, \pi^-)$ reaction and determined the energy spacing between the spin-doublet states $(1^+, 0^+)$ to be 1406 $\pm$ 2 (stat.) $\pm$ 2 (syst.) keV. The apparent difference from the ${}^{4}_{\Lambda}$H spacing of 1.09 $\pm$ 0.02 MeV and thus the existence of CSB in ΛN interaction have been confirmed only via the γ-ray measurement. Combined with the emulsion data of $B_\Lambda(0^+)$, the present result indicates a large spin dependence in the CSB effect, by one order of magnitude larger in the 0^+ state energy than in the 1^+ state energy, providing crucial information toward understanding ΛN-ΣN interaction and eventually baryon-baryon interactions.

Contents

List of Figures

List of Tables

Chapter 1

Introduction

Charge symmetry is a basic concept in nuclear physics. This symmetry holds almost exactly in NN interaction; only quite small charge symmetry breaking (CSB) effects have been reported. The CSB effect in NN interaction was studied as an important subject for understanding hadronic interaction. Unlike NN interaction, experimental data indicate an unexpectedly large CSB effect in ΛN interaction reflected in structures of A=4 mirror Λ hypernuclei ($^{4}_{\Lambda}$H and $^{4}_{\Lambda}$He). The present work reaffirms this observation by providing more solid experimental foundation. The study of the observed large CSB effect in ΛN interaction is a good test for our current framework of baryon-baryon interaction.

In this chapter, the studies of charge symmetry in NN interaction and then CSB effects in Λ hypernuclei reported by the past studies will be discussed. The physics motivation of the present work is given at the end.

1.1 Charge symmetry and CSB in NN interaction

Charge symmetry

Charge symmetry is a general concept in the nuclear and hadronic systems. Under charge symmetry, hadronic state is invariant with respect to a rotation around y axis by 180° in isospin (T) space, which corresponds to an interchange of u and d quarks. For example, p–n and Σ^{+}–Σ^{-} pairs are identical under charge symmetry (see Fig. 1.1). Actually, charge symmetry is slightly broken due to the mass difference between u and d quarks, resulting in the mass difference in p–n and Σ^{+}–Σ^{-} pairs. Charge symmetry also holds in hadronic interaction as well as nuclear structure. On the other hand, charge independence is a more general concept in strong interaction, in which hadronic state is invariant under any rotation in isospin space (for example, Σ^{+}–Σ^{0}–Σ^{-} isospin triplet is identical under charge independence).

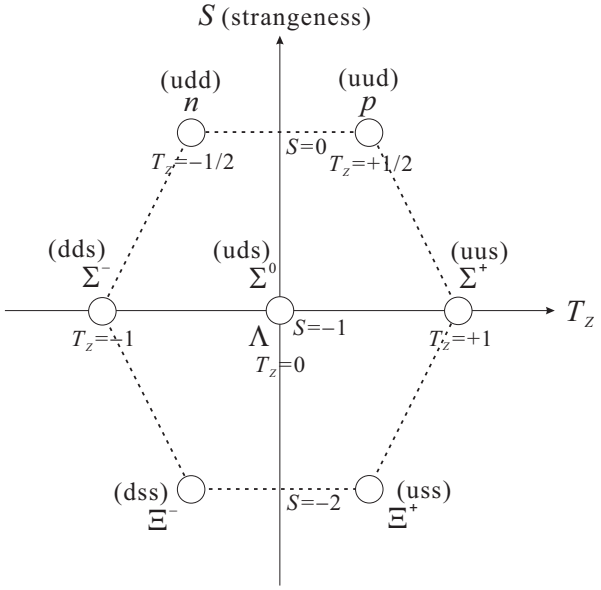

Figure 1.1: The baryon octet in the $SU_f(3)$ symmetry with spin 1/2. S and T_z denote strangeness and z component of isospin, respectively.

CSB in NN interaction

NN force can be characterized by introducing isospin T, where a proton and a neutron are assigned z-axis projection of isospin (T_z) $+1/2$ and $-1/2$, respectively. pp ($T_z = +1$) and nn ($T_z = -1$) forces belong to the $T = 1$ multiplet, while pn ($T_z = 0$) force has both $T = 0$ and 1 multiplet components. Charge symmetry is a general property in the nuclear force, that p-p and n-n forces which are related to each other by 180° rotation around T_y axis in the isospin space is equivalent. Charge independence, on the other hand, is a more general isospin symmetry ; in which p-p, n-n and p-$n(T = 1)$ forces are equal.

Charge symmetry holds almost exactly for atomic nuclei; in fact only quite small CSB effects were reported (G. A. Miller summarized the CSB effect in the NN interaction in Ref. [1]). In NN interaction and ordinary nuclei, effects of CSB have been observed, and two examples will be mentioned here.

(1) If the charge symmetry holds exactly, the pp and nn scattering lengths should be equal without the Coulomb effects. The scattering lengths corrected for the Coulomb effects are reported as $a_{pp}^N = -17.3 \pm 0.4$ fm and $a_{nn}^N = -18.8 \pm 0.3$ fm. The difference between them ($a_{pp}^N - a_{nn}^N = 1.5 \pm 0.5$ fm) is considered to originate from the CSB effect in strong interaction.

(2) The binding-energy difference between ^{3}H and ^{3}He is given as $\Delta B = B(^3\mathrm{He}) - B(^3\mathrm{H}) = -764$ keV. ^{3}He is less bound than ^{3}H because of the repulsion of two protons in

^{3}He with the Coulomb interaction. From an exact three-body calculation applied to the A=3 nuclear system, the contribution of the Coulomb interaction to the binging energy difference was estimated to be $\Delta B = -693 \pm 19 \pm 5$ keV [2], where the first uncertainty comes from the error in the form factors and the second reflects model dependence of the meson-exchange corrections to the measured form factors. The remaining difference of $\Delta B = -71 \pm 24$ keV was attributed to the CSB contribution in strong interaction.

The origin of such CSB effects is expected to originate from the current mass difference between u quark ($M_u = 2.3^{+0.7}_{-0.5}$ MeV) and d quark ($M_d = 4.8^{+0.5}_{-0.3}$ MeV), $\Delta M_{ud} = M_u - M_d \cong -2.5$ MeV. This difference leads to the differences in the hadron mass, for example, the mass difference between proton and neutron of about 0.1% ($\Delta M_{pn} = M_p(938.27 \text{ MeV}) - M_n(939.56 \text{ MeV}) = -1.29$ MeV). In addition, the asymmetry in the ud quark mass causes the isospin mixing in mesons, such as $\pi^0(T{=}1)-\eta(T{=}0)$ and $\rho^0(T{=}1)-\omega(T{=}0)$ mixing. The effect of this isospin mixing appears in NN CSB interaction with an opposite contribution between pp and nn interaction because of the different sign in the $\pi^0 NN$ coupling constant ($g_{\pi^0 pp} = -g_{\pi^0 nn}$) while the same sign in the ηNN coupling constant in $\pi^0 - \eta$ mixing, for example. Meson-exchange models claimed that $\rho^0 - \omega$ mixing has a larger effect on NN CSB interaction than $\pi^0 - \eta$ mixing. The observed CSB effects in the ^{3}He-^{3}H masses can be explained by $\rho^0 - \omega$ mixing [1].

1.2 Λ hypernuclear structure and CSB in ΛN interaction

ΛN interaction has been indirectly studied through the structure of single Λ hypernuclei instead of direct ΛN scattering due to difficulties of such scattering experiments associated with the short lifetime of Λ. This is not the case in studies of NN interaction.

The first observation of a Λ hypernucleus was reported by an experiment using nuclear emulsion method [3]. Later, Λ hypernuclei were studied in more detail by reaction spectroscopy using reactions such as the $n(K^-, \pi^-)\Lambda$ and the $n(\pi^+, K^+)\Lambda$ reactions with an energy resolution of ∼2 MeV. Recently, the energy resolution was improved to ∼0.6 MeV by employing the $p(e, e' K^+)\Lambda$ reaction with an advantage of intensive primary e^- beams which allow for the use of a thin target. From these studies, the strength of the central (spin-independent) part of ΛN interaction was determined. On the other hand, the spin-dependent part of ΛN interaction was studied via γ-ray spectroscopy using NaI detectors and then germanium (Ge) detectors. A better energy resolution of <0.1 MeV was essential to resolve a small energy spacing of spin-doublet structures [for example, 26 keV for $^{16}_{\Lambda}\mathrm{O}(1^-_1, 0^-)$ [4]]. The spin-dependent ΛN interaction lifts energy degeneracy between doublet states with an opposite alignment between "core" nucleus spin (J) and

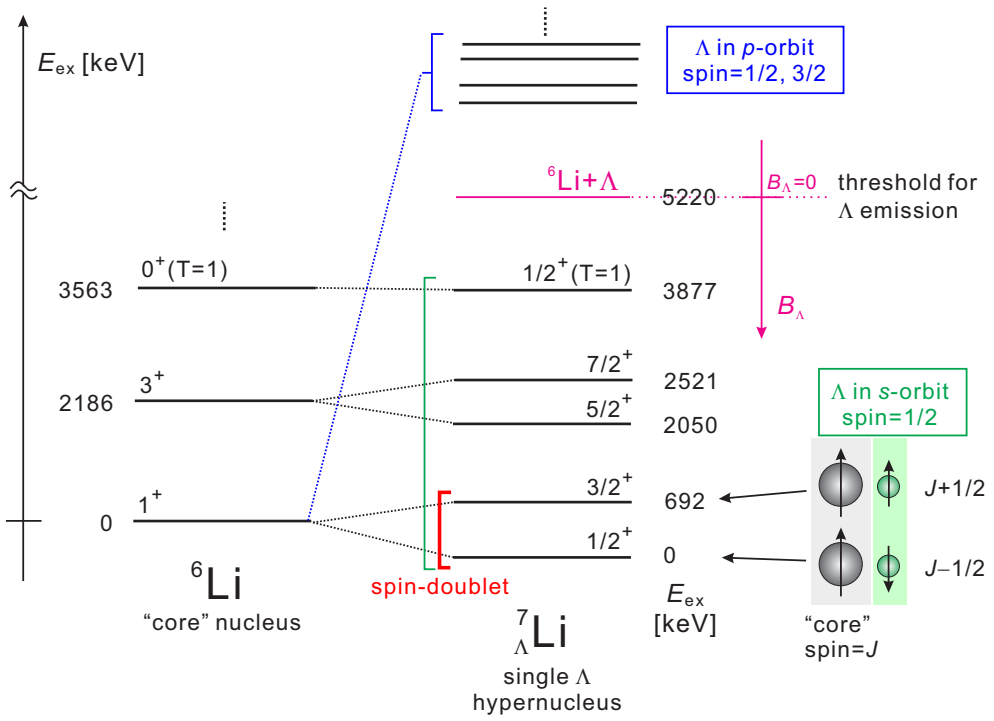

Figure 1.2: Level scheme of $^7_\Lambda$Li and its "core" nucleus. The spin-doublet structure appears from the spin-dependent part of the ΛN interaction. The excitation energies were measured by γ-ray spectroscopy experiments using Ge detectors [5, 6].

a Λ spin (1/2), $J \pm 1/2$, when $J \neq 0$. Figure 1.2 shows the level scheme of $^7_\Lambda$Li, one of the best studied hypernuclei, together with its "core" nucleus. The structure of $^7_\Lambda$Li was first studied via reaction spectroscopy. Subsequently, its fine structure such as spin-doublet was measured via the γ-ray spectroscopy experiments using a Ge detector array constructed in the Hyperball project [5, 6].

ΛN-ΣN coupling interaction

In ΛN interaction (S(strangeness) $= -1$ sector), ΛN-ΣN coupling may have a larger effect than NN-ΔN mixing in the $S = 0$ sector because of its smaller mass difference of $M_\Sigma - M_\Lambda \cong 80$ MeV compared to $M_\Delta - M_N \cong 300$ MeV. (The mixing effect is expected to increase further in the $S = -2$ sector with the much smaller mass difference of $M_{\Lambda\Lambda} - M_{\Sigma N} \cong 30$ MeV.) Experimental and theoretical studies of the p-shell hypernuclei indicate a significant contribution of ΛN-ΣN coupling on hypernuclear structures (see Ref. [7], for example).

The one-pion exchange is forbidden in ΛN interaction from isospin conservation. On the other hand, with a two-pion exchange, ΛN-ΣN conversions in two-body channel

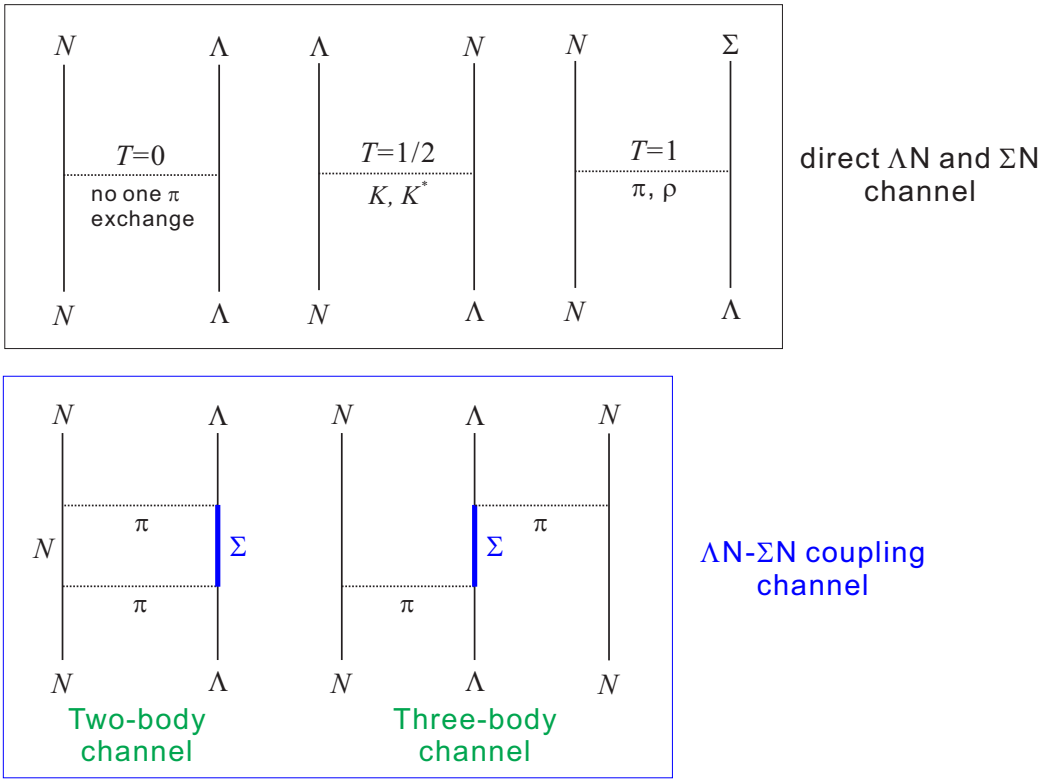

Figure 1.3: Diagrams for the direct ΛN and ΣN channels (top) and the ΛN-ΣN coupled channels (bottom). The one-pion exchange is forbidden in the direct ΛN interaction due to isospin conservation. With two-pion exchange, ΛN-ΣN conversion is allowed. The diagram for the three-body ΛNN interaction via ΛN-ΣN conversion is illustrated in the bottom right.

and three-body channel are allowed as illustrated in Fig. 1.3. Y. Akaishi claimed that this three-body ΛN-ΣN coupling channel plays an important role in the hypernuclear structure [8] as described in Section 6.4.

CSB effect in ΛN interaction

The charge symmetry should also hold in ΛN interaction and Λ hypernuclei; Λp and Λn interactions and Λ binding energies (B_Λ) between a pair of mirror Λ hypernuclei such as ${}^{4}_{\Lambda}$H and ${}^{4}_{\Lambda}$He should be identical under this symmetry. The binding energy is defined as $B_\Lambda = M_{core} + M_\Lambda - M_{HYP}$, where M_{HYP}, M_{core}, and M_Λ denote the mass of a hypernucleus, of the "core" nucleus, and of Λ, respectively. It should be noted that B_Λ does not directly involve any Coulomb interactions and the CSB effect in NN interaction. First, there is no direct Coulomb interaction between charge-neutral Λ and N. Second, the binding energy of the "core" nucleus, in which the CSB effect in NN

interaction appears, is canceled out in $M_{core} - M_{HYP}$. It means that the CSB effect in ΛN interaction can be studied almost directly from the difference of B_Λ in mirror hypernuclei.

There has been a long standing CSB puzzle, however, for ΛN interaction; the reported differences in B_Λ are notably large in the A=4 hypernuclear systems, having yet to be theoretically explained (see the next section).

The CSB effects reported for some *s*- and *p*-shell hypernuclei are listed in Table 1.2.1, where all the measured B_Λ values of the ground state, B_Λ(g.s.), listed are reported from emulsion experiments [9, 10]; the B_Λ(g.s.) values of A$\leq$15 hypernuclei were measured by experiments using the emulsion technique, employing K^- stopped in nuclear emulsion stacks and absorbed by nuclei in emulsion. Only in the A=4 hypernuclei, ${}^{4}_{\Lambda}$H/${}^{4}_{\Lambda}$He, a significant difference of 350 $\pm$60 keV in B_Λ(g.s.) was observed. It is noted that B_Λ(g.s.) values of ${}^{12}_{\Lambda}$C and ${}^{12}_{\Lambda}$B were 10.80 $\pm$0.18 MeV [11] and 11.37 $\pm$0.06 MeV, respectively, showing also a large CSB effect of ΔB_Λ=$-$0.57 $\pm$0.19 MeV. However, a recent systematic study suggests that the quoted emulsion value of $B_\Lambda({}^{12}_{\Lambda}\mathrm{C})$ should be shifted by $\sim$+0.5 MeV [12], which would give no significant CSB effect.

Table 1.2.1: B_Λ differences in the ground state of the *s*- and *p*-shell mirror hypernuclei measured by emulsion experiments [10] [see Ref. [11] for $B_\Lambda({}^{12}_{\Lambda}\mathrm{C})$]. Unit is in keV.

mirror hypernuclei	ΔB_Λ(g.s.)
${}^{4}_{\Lambda}$He$-{}^{4}_{\Lambda}$H	+350 $\pm$ 60
${}^{8}_{\Lambda}$Be$-{}^{8}_{\Lambda}$Li	+40 $\pm$ 60
${}^{9}_{\Lambda}$B$-{}^{9}_{\Lambda}$Li	$-$210 $\pm$ 220
${}^{10}_{\Lambda}$B$-{}^{10}_{\Lambda}$Be	$-$220 $\pm$ 250
${}^{12}_{\Lambda}$C$-{}^{12}_{\Lambda}$B	($-$570 $\pm$ 190)

1.3 Unexpectedly large CSB manifestation in A=4 hypernuclei

The A=4 hypernuclear systems have drawn considerable interests related to CSB in ΛN interaction. The existing experimental data for the ground-state B_Λ and the excitation energies of ${}^{4}_{\Lambda}$H and ${}^{4}_{\Lambda}$He suggest a much larger ΛN CSB effect than NN in A=3 ordinary mirror nuclei. Because no direct Coulomb interaction arises in ΛN interaction, the CSB effect in ΛN strong interaction should be reflected almost directly in the B_Λ difference in A=4 mirror hypernuclei. Theoretically, it is easier to calculate these hypernuclei in exact few-body calculation frameworks.

Figure 1.4 shows level schemes of the mirror hypernuclei, ${}^{4}_{\Lambda}$H and ${}^{4}_{\Lambda}$He. The ground

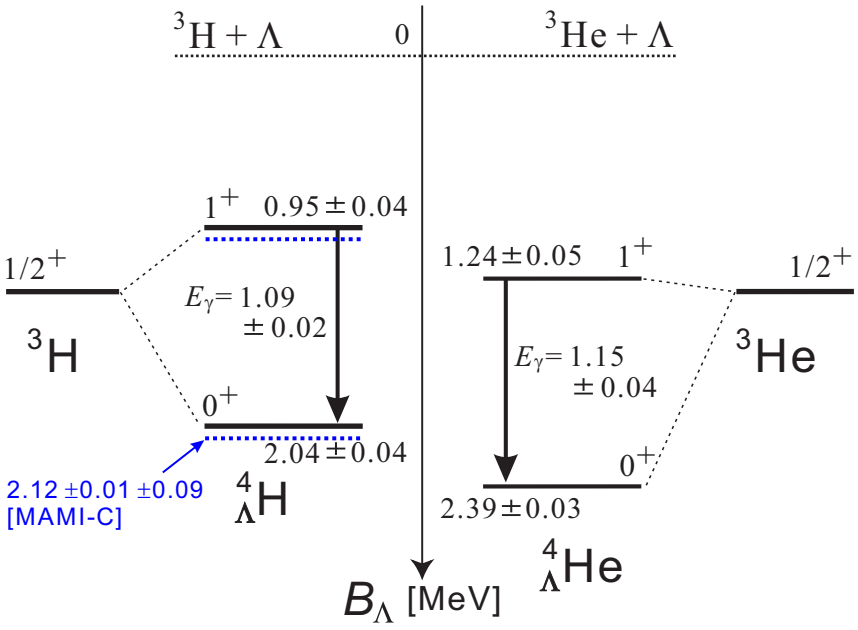

Figure 1.4: Level schemes of the mirror hypernuclei, $^4_\Lambda$H and $^4_\Lambda$He. Λ binding energies (B_Λ) of $^4_\Lambda$H(0^+) and $^4_\Lambda$He(0^+) are taken from the past emulsion experiments [9]. $B_\Lambda(^4_\Lambda\mathrm{He}(1^+))$ and $B_\Lambda(^4_\Lambda\mathrm{H}(1^+))$ are obtained using the past γ-ray data [13, 14, 15]. Recently, $B_\Lambda(^4_\Lambda\mathrm{H}(0^+)) = 2.12 \pm 0.01$ (stat) $\pm$ 0.09 (syst) MeV was obtained with an independent technique [16].

Table 1.3.1: Reported Λ binding energies (B_Λ) of $^4_\Lambda$H/$^4_\Lambda$He. Unit is in MeV.

	Ground state (0^+)	1st-excited state (1^+)
with emulsion data [9]		
$^4_\Lambda$H	2.04 ±0.04	0.95 ±0.04
$^4_\Lambda$He	2.39 ±0.03	1.24 ±0.05
$\Delta B_\Lambda[^4_\Lambda\mathrm{He}-^4_\Lambda\mathrm{H}]$	+0.35 ±0.05	+0.29 ±0.06
with MAMI-C data [16]		
$^4_\Lambda$H	2.12 ±0.10	1.03 ±0.10
$\Delta B_\Lambda[^4_\Lambda\mathrm{He}-^4_\Lambda\mathrm{H}]$	+0.27 ±0.11	+0.21 ±0.11

0^+ state and the 1st excited 1^+ state are the members of the spin-doublet, and a major part of its energy spacing originates from the Λ spin - "core" spin interaction. Only these two states are below the Λ emission threshold (B_Λ=0) and particle bound, and thus the ($1^+ \rightarrow 0^+$) γ-transition is allowed. The spin assignment for the ground state [$J_{g.s.} = 0$] was made using helium bubble chamber technique [17]. The angular distribution of pions from the $^4_\Lambda$H→^{4}He+π^- weak decay with respect to the recoil momentum direction of the hypernucleus was found to be isotropic, indicating the 0^+ spin of $^4_\Lambda$He(g.s.) [18]. This spin assignment is supported by an analysis for the branching ratio of the weak decay [19].

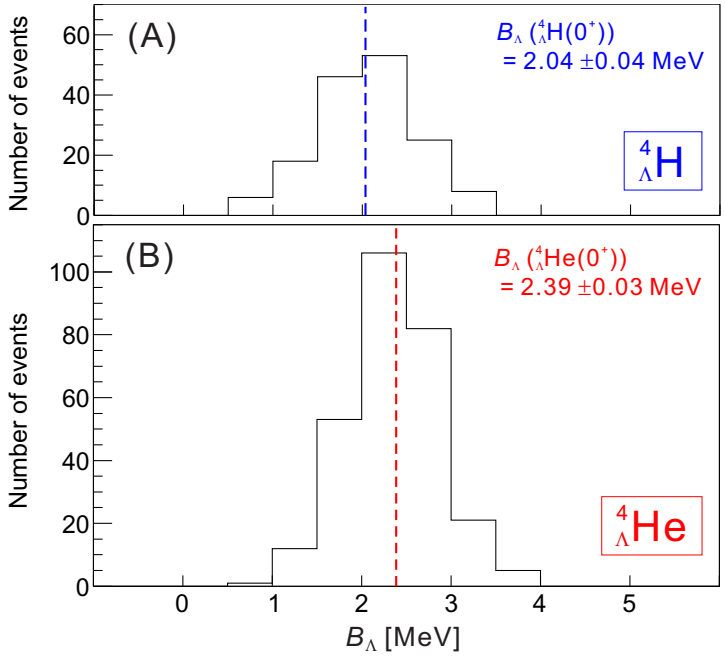

Figure 1.5: $B_\Lambda(0^+)$ distribution for $^4_\Lambda$H (spectrum (A)) and $^4_\Lambda$He (spectrum (B)) measured by emulsion experiments [9]. Reported mean values are $B_\Lambda(^4_\Lambda\mathrm{H}(0^+))$=2.04 ± 0.04 MeV and $B_\Lambda(^4_\Lambda\mathrm{He}(0^+))$=2.39 ± 0.03 MeV.

The B_Λ values of the ground state of A≤15 hypernuclei were measured by emulsion experiments. Old emulsion experiments reported B_Λ of the ground states of $^4_\Lambda\mathrm{H}(0^+)$ and $^4_\Lambda\mathrm{He}(0^+)$ to be 2.04 ± 0.04 MeV and 2.39 ± 0.03 MeV, respectively (see Fig. 1.5) [9]. The B_Λ difference was $\Delta B_\Lambda(0^+) = B_\Lambda(^4_\Lambda\mathrm{He}(0^+)) - B_\Lambda(^4_\Lambda\mathrm{H}(0^+)) = 0.35 \pm 0.05$ MeV, indicating a large CSB effect in ΛN interaction. On the other hand, the B_Λ values for the 1^+ state were reported to be $B_\Lambda(^4_\Lambda\mathrm{H}(1^+))$=0.95 ±0.04 MeV and $B_\Lambda(^4_\Lambda\mathrm{He}(1^+))$=1.24 ±0.05 MeV via the measurements of the $1^+ \to 0^+$ γ-ray transition (see Appendix A for a detailed description of these γ-ray measurements). The difference in $B_\Lambda(1^+)$ is 0.29 ± 0.06 MeV, which also indicates a large CSB effect. In comparison, the difference in the excitation energies of the 1^+ states (ΔE_{ex}=0.06 ±0.05 MeV) was sizable but relatively small. The reported B_Λ values and their differences are summarized in Table 1.3.1.

1.4 Theoretical studies for CSB effect in $^4_\Lambda$H/$^4_\Lambda$He

Theoretical efforts have been made since the 1960s [20] to account for the $\Delta B_\Lambda(0^+)$ value, but contemporary quantitative studies all fail to give a $\Delta B_\Lambda(0^+)$ value larger than 100 keV. For example, a 4-body $YNNN$ coupled-channel calculation with $Y = \Lambda$ and Σ using the widely-accepted baryon-baryon interaction model (NSC97e) was performed by

A. Nogga in the 2000s. The comparison between this calculation and the experimental data is summarized in Table 1.4.1. Nogga suggested that there are four components that are responsible for the CSB energy shift on the 0^+ state. These are

- the difference in Σ mass (m_Σ) leading to +47-keV CSB energy difference as $\Delta T^{CSB}_{M_\Sigma} = (P_{\Sigma^+} - P_{\Sigma^-}) \cdot (m_{\Sigma^-} - m_{\Sigma^+})$ (this effect is slightly suppressed by a change in the momentum dependent part of the kinetic energy),

- a contribution of strong CSB YN interaction originating from the mass differences of the baryons and mesons and Λ-Σ^0 conversion, leading to +44-keV CSB energy difference,

- a change of Coulomb interaction in pp pairs, leading to -9-keV CSB energy difference, due to a change in the structure of the "core" nucleus induced by a hyperon,

- an additional Coulomb interaction between $\Sigma^+ p$ and $\Sigma^- p$ pairs leading to -7-keV CSB energy difference.

They reported that inclusion of the ΛN-ΣN channel (as illustrated in Fig. 1.6) with the mass differences has a larger effect on the CSB impact than the contribution from Coulomb interaction. Although they pointed out the importance of a ΛN-ΣN mixing effect, the calculation gives a total CSB effect of $\Delta B_\Lambda(0^+) \sim +70$ keV, which is much smaller than the experimental result of $\Delta B_\Lambda(0^+)$=350 $\pm$50 keV. They also reported a calculation with the NSC89 interaction model. The result shows a larger CSB energy difference of $\sim$350 keV, which originates from a larger Σ mixing probability than the NSC97 model. It failed, however, to reproduce the excitation energy of the 1^+ states; the calculated excitation energy was 2.06 MeV for ${}^{4}_{\Lambda}\mathrm{He}(1^+)$ which is much larger than the experimental result of $E_{\mathrm{ex}}({}^{4}_{\Lambda}\mathrm{He}(1^+))$=1.15 $\pm$0.04 MeV. They discussed that an inclusion of the ΛN-ΣN channel makes strong spin dependence and that the energy splitting of $(0^+, 1^+)$ would be strongly affected by the ΛN-ΣN mixing. This study, therefore, suggests that both values of $B_\Lambda(0^+)$ and $B_\Lambda(1^+)$ are sensitive to the ΛN-ΣN mixing.

Experimentally, the old emulsion data for the $B_\Lambda(0^+)$ value was questioned because systematic errors are not well evaluated and no theoretical calculation has reproduced the existing data. In addition, the old data for the excitation energy of ${}^{4}_{\Lambda}\mathrm{He}(1^+)$ using NaI counters were statistically insufficient to discuss the CSB effect. Therefore, re-examinations of the existing data with modern techniques have been awaited.

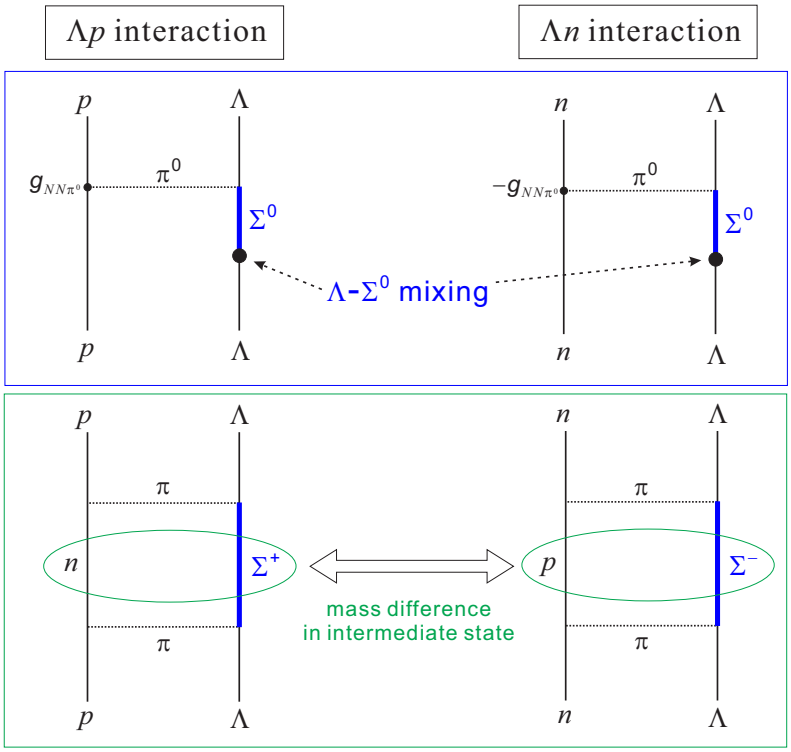

Figure 1.6: Diagrams for the CSB Λ-Σ^0 mixing channels (top) and the CSB ΛN-ΣN coupled channels (bottom).

Table 1.4.1: Comparison between the four-body calculation by A. Nogga [21] (calc. I: with the NSC97e interaction model, calc Ⅱ: with the NSC89 model) and the experimental data. Unit is in MeV.

	exp. data	calc.Ⅰ [21] NSC97e	calc.Ⅱ [21] NSC89
Λ binging energy			
$B_\Lambda(^4_\Lambda\mathrm{H}(0^+))$	2.04 ±0.04	1.47	1.80
$B_\Lambda(^4_\Lambda\mathrm{H}(1^+))$	0.95 ±0.04	0.73	
$B_\Lambda(^4_\Lambda\mathrm{He}(0^+))$	2.39 ±0.03	1.54	2.14
$B_\Lambda(^4_\Lambda\mathrm{He}(1^+))$	1.24 ±0.05	0.72	
excitation energy			
$E_{\mathrm{ex}}(^4_\Lambda\mathrm{H}(1^+))$	1.09 ±0.02	0.74	
$E_{\mathrm{ex}}(^4_\Lambda\mathrm{He}(1^+))$	1.15 ±0.04	0.82	2.06
$\Delta B_\Lambda = B_\Lambda(^4_\Lambda\mathrm{He}) - B_\Lambda(^4_\Lambda\mathrm{H})$			
$\Delta B_\Lambda(0^+)$	+0.35 ±0.05	0.07	0.34
$\Delta B_\Lambda(1^+)$	+0.29 ±0.05	−0.01	

1.5 Experimental improvement for the measurement of $B_\Lambda(0^+)$

Recently, MAMI-C group reported an experimental value of $B_\Lambda(^4_\Lambda\mathrm{H}(0^+))$ with a new technique using decay pions [16]. In the experiment, $^4_\Lambda$H was produced as a hyperfragment

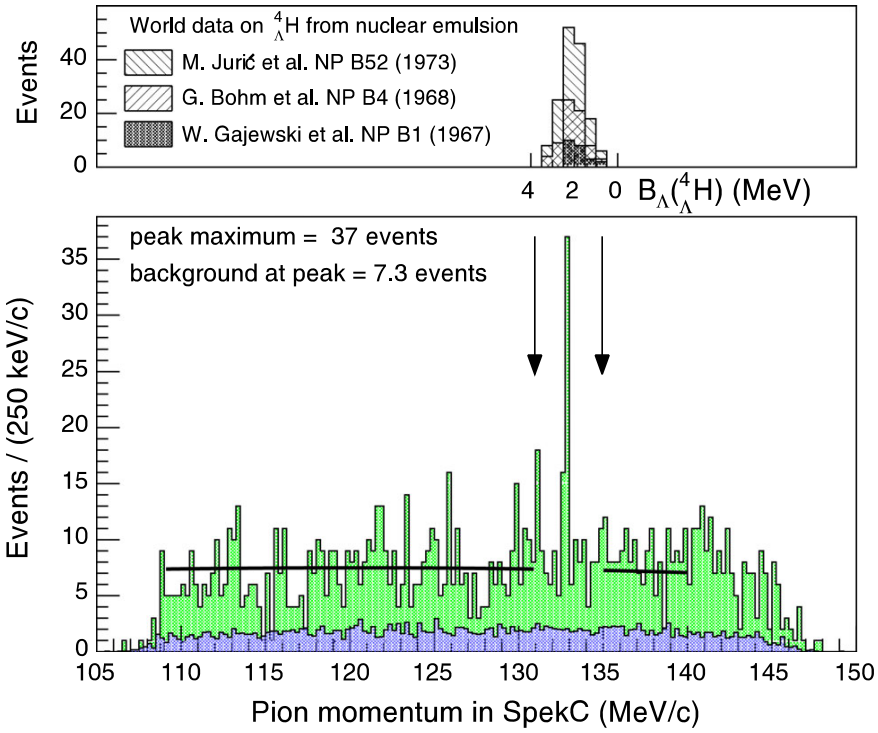

Figure 1.7: Measured π^- momentum in the $^4_\Lambda\mathrm{H} \to {}^4\mathrm{He} + \pi^-$ weak decay [16] (bottom spectrum). The obtained $B_\Lambda(^4_\Lambda\mathrm{H}(0^+))$ is 2.12 $\pm$ 0.01 (stat) $\pm$ 0.09 (syst) MeV. The reported B_Λ value is consistent with the emulsion value as shown in the top spectrum.

via the $^9\mathrm{Be}(e, e'K^+)$ reaction. The π^- momentum in the $^4_\Lambda\mathrm{H} \to {}^4\mathrm{He} + \pi^-$ weak decay was more precisely measured as shown in Fig. 1.7, and the new $B_\Lambda(^4_\Lambda\mathrm{H}(0^+))$ value was obtained as 2.12 $\pm$ 0.01 (stat) $\pm$ 0.09 (syst) MeV. By comparing it with the result of the emulsion experiments, $B_\Lambda(^4_\Lambda\mathrm{H}(0^+))$=2.04 $\pm$ 0.04 MeV, the statistical error in the measured B_Λ value was reduced owing to its good π^- momentum resolution. A rather large systematic error ($\pm$0.09 MeV) comes from the calibration, but the MAMI-C group is now trying to reduce this systematic error. The reported $B_\Lambda(^4_\Lambda\mathrm{H}(0^+))$ value is consistent with the emulsion value. The obtained B_Λ value and a difference from that of $^4_\Lambda$He are also summarized in Table 1.3.1.

On the other hand, a measurement of $B_\Lambda(^4_\Lambda\mathrm{He}(0^+))$ other than the emulsion method and with a energy precision of better than 0.1 MeV for the study of CSB effect is difficult. The reasons for this difficulty are

- no two body π^- decay channel (the main channel is $^4_\Lambda\mathrm{He} \to {}^4\mathrm{He} + \pi^0$), making the decay π^- spectroscopy unrealistic,

- contamination from the 1^+ state, which is populated via the spin-flip Λ production, causes a serious problem in missing mass spectroscopy (especially with the $(e, e'K^+)$

reaction in which the 1^+ state is expected to be predominantly populated),

- lack of calibration method in the (K^-, π^-) or the (π^+, K^+) reactions without referring to the emulsion data, because free neutrons are not available as a target.

Because of these difficulties, a precise measurement of $B_\Lambda(^4_\Lambda\mathrm{He}(0^+))$ without using emulsion has yet to be realized.

1.6 Old γ-ray spectroscopic experiment of $^4_\Lambda$H/$^4_\Lambda$He

The B_Λ difference for the excited 1^+ states provides additional important information on the spin-dependent CSB effect from which the origin of CSB can be studied. The B_Λ values for the 1^+ state are obtained from the $1^+ \to 0^+$ γ-ray transition energies.

The $^4_\Lambda$H γ ray has been measured three times, and the weighted average of the excitation energies (E_{ex}) of $^4_\Lambda\mathrm{H}(1^+)$ was 1.09 $\pm$ 0.02 MeV. These three measurements are

- $E_{\mathrm{ex}}(^4_\Lambda\mathrm{H}(1^+))$=1.09 $\pm$ 0.03 MeV reported by M. Bedjidian *et al.* (1976) [13],
- $E_{\mathrm{ex}}(^4_\Lambda\mathrm{H}(1^+))$=1.04 $\pm$ 0.04 MeV reported by M. Bedjidian *et al.* (1979) [14],
- $E_{\mathrm{ex}}(^4_\Lambda\mathrm{H}(1^+))$=1.114 $\pm$ 0.030 MeV reported by A. Kawachi (1997) [15].

The average value of $E_{\mathrm{ex}}(^4_\Lambda\mathrm{H}(1^+))$ seems to be statistically accurate; three independent experiments show almost consistent E_{ex} values with enough statistics. In addition, other past experiments reports hints of unassigned γ-ray at $\sim$1.09 MeV (see Section 6.1), which may support the average value of $E_{\mathrm{ex}}(^4_\Lambda\mathrm{H}(1^+))$. The description of these experiments will be given in Appendix A.

On the other hand, observation of the $^4_\Lambda$He γ ray has been reported only once, which claimed the $(1^+, 0^+)$ energy spacing of

- $E_{\mathrm{ex}}(^4_\Lambda\mathrm{He}(1^+))$=1.15 $\pm$ 0.04 MeV, by M. Bedjidian *et al.* (1979) [14].

These results also lead to an unexpectedly large CSB effect in the 1^+ state with $\Delta B_\Lambda(1^+)$ = 0.29 $\pm$ 0.06 MeV, while a difference in the excitation energies was found to be small, namely $\Delta E_{\mathrm{ex}} = E_{\mathrm{ex}}(^4_\Lambda\mathrm{He}(1^+)) - E_{\mathrm{ex}}(^4_\Lambda\mathrm{H}(1^+)) = +0.06 \pm 0.05$ MeV. The reported values of the excitation energy of the 1^+ state are listed in Table 1.6.1 and Fig. 1.8.

However, the $^4_\Lambda$He γ-ray spectrum obtained by the past experiment is statistically insufficient as shown in Fig. 1.9 (b) and (c), and the identification of the $^4_\Lambda$He hyperfragment appears not conclusive (see Appendix A for description of the previous experiment). Therefore, we proposed a new experiment with current techniques to re-examine the excitation energy of $^4_\Lambda\mathrm{He}(1^+)$.

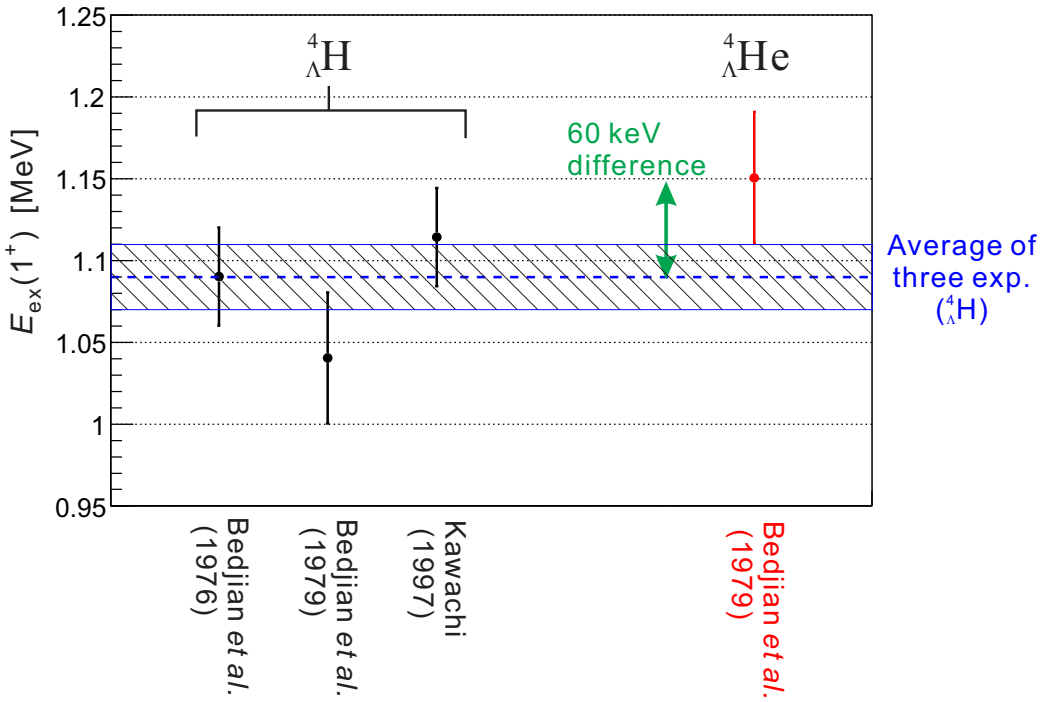

Figure 1.8: Reported excitation energies of 1^+ states of $^4_\Lambda$H/$^4_\Lambda$He.

Table 1.6.1: Reported γ-ray energies for $^4_\Lambda$H/$^4_\Lambda$He. Unit is in MeV. A difference in the averaged energies was ΔE_{ex}=0.06 $\pm$ 0.05 MeV.

	$^4_\Lambda$H($1^+ \to 0^+$)	$^4_\Lambda$He($1^+ \to 0^+$)
M. Bedjidian *et al.* (1976) [13]	1.09 $\pm$0.03	-
M. Bedjidian *et al.* (1979) [14]	1.04 $\pm$0.04	1.15 $\pm$0.04
A. Kawachi (1997) [15]	1.114 $\pm$0.030	-
Weighted average	1.09 $\pm$0.02	1.15 $\pm$0.04

1.7 Purpose of the present work - precise measurement of $E_{ex}(^4_\Lambda\mathrm{He}(1^+))$

We performed a γ-ray spectroscopic experiment of $^4_\Lambda$He at Japan Proton Accelerator Research Complex (J-PARC) [22, 23, 24]. The single past experiment [14] which measured the $E_{ex}(^4_\Lambda\mathrm{He}(1^+))$ suffers from problems summarized below,

- insufficient statistical significance of the 1.15-MeV peak (less than 3σ) due to the energy resolution of the NaI detector [12% (FWHM) at 0.98 MeV] as well as the Doppler broadening responsible for the 50$\sim$100-keV peak width [25],

- ambiguity in identifying hyperfragments,

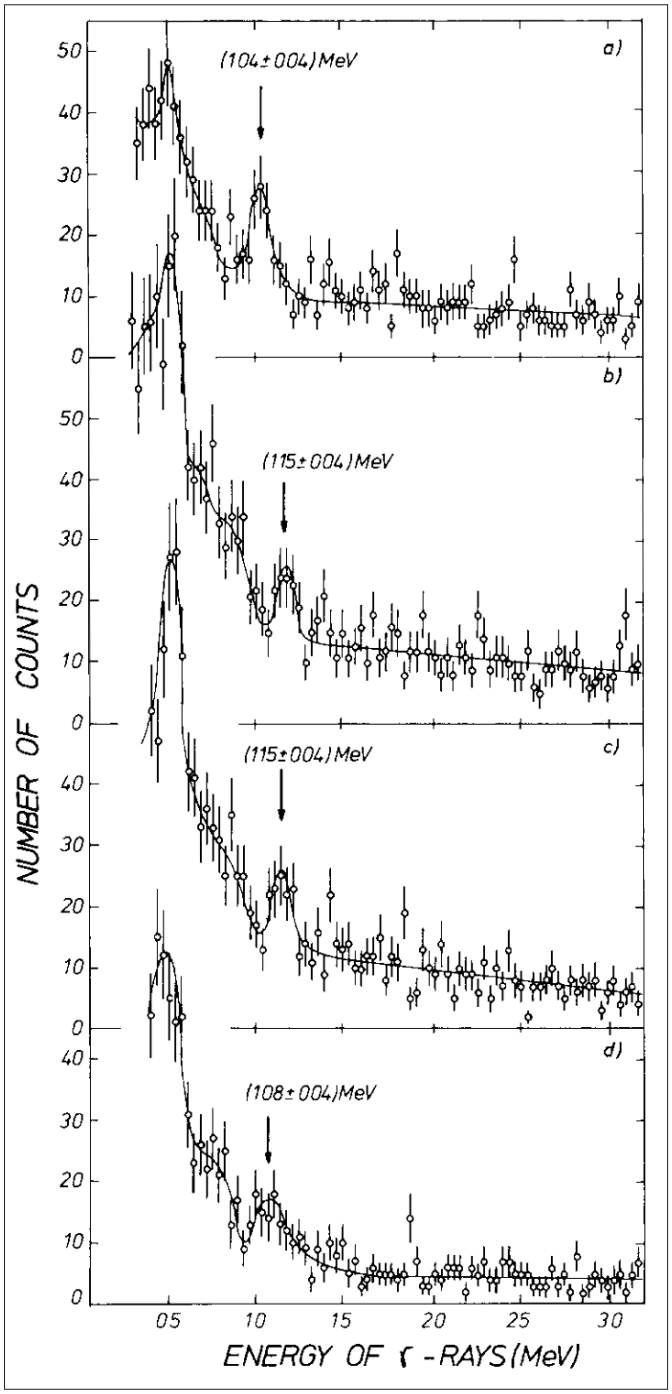

Figure 1.9: γ-ray energy spectra reported by M. Bedjidian *et al.* (1979) [14]; (a) summed spectrum for the ^{6}Li and ^{7}Li target after selecting a charged pion with a kinetic energy (E_{kin}) of 48–58 MeV, (b) same as (a) but selecting π^{0} with E_{kin} = 45–85 MeV, (c) spectrum of the ^{6}Li target only by selecting π^{0} with E_{kin} = 200–400 MeV, (d) spectrum of the ^{7}Li target only by selecting π^{0} with E_{kin} = 100–180 MeV. See Appendix A for a detailed description of the experiment.

  - indirect production as hyperfragments following the stopped K^- absorption on ^{7}Li,
  - selection of a kinetic energy of π^0 from the ${}^{4}_{\Lambda}\mathrm{He}\rightarrow{}^{4}\mathrm{He} + \pi^0$ weak decay by measuring an opening angle between two γ rays from $\pi^0 \rightarrow \gamma\gamma$,

- difficulty in energy calibration due to a possible gain shift of the NaI detector for change of crystal temperature.

The present experiment achieved much higher sensitivity with the following features. The comparison between the present and the past experiment is summarized in Table 1.7.1 and Table 1.7.2. In the present experiment, the 1^+ excited state of ${}^{4}_{\Lambda}\mathrm{He}$ was directly produced via the in-flight ${}^4\mathrm{He}(K^-,\pi^-)$ reaction with $p_K = 1.52$ GeV/c taking advantage of a high intensity K^- beam. The ${}^{4}_{\Lambda}\mathrm{He}$ production was tagged by magnetic spectrometers with missing mass analysis. By taking coincidence with the (K^-,π^-) reaction, γ rays were measured using Ge detectors with an energy resolution of 0.5% (FWHM) at 1 MeV. Furthermore, Doppler broadening of the γ-ray peaks can be reduced by event-by-event correction combined with the in-flight (K^-,π^-) reaction analysis. The peak shape after the Doppler-shift correction can be used to confirm that the γ-ray is emitted from the hypernucleus. A continuous energy calibration during the data-taking

Table 1.7.1: Comparison between the present and the past experiment.

	Present experiment	M. Bedjidian *et al.*[14]
Peak energy [keV]	1406 ±2(stat.) ±2(syst.)	1150 ± 40
Energy resolution	0.5% (at 1 MeV)	12% (at 0.98 MeV)
Doppler broadening	100 keV (FWHM)	50-100 keV (FWHM)
Doppler correction	Yes	No
(peak width after correction)	14 keV (FWHM)	-
Statistical significance	7.4σ	$<3\sigma$
Hypernuclear production	direct production	hyperfragment
	[in-flight ${}^{4}_{\Lambda}\mathrm{He}(K^-,\pi^-)$]	[stopped K^- with ^{6,7}Li]
Detected particles	K^-,π^-,γ	$K^-_{(\mathrm{stopped})}$, $\pi^0 \rightarrow \gamma\gamma$, γ

Table 1.7.2: Comparison in identification methods of hypernuclei between the present and the past experiment.

Present experiment	(1) missing mass analysis for tagging direct ${}^{4}_{\Lambda}\mathrm{He}$ production. (2) peak shape analysis after the Doppler-shift correction. (3) comparison between obtained yield of ${}^{4}_{\Lambda}\mathrm{He}(0^+$ and $1^+)$ and that of DWIA calculation.
M. Bedjidian *et al.*[14]	(1) tagging π^0 from the ${}^{4}_{\Lambda}\mathrm{He}\rightarrow{}^{4}\mathrm{He} + \pi^0$ weak decay [with selecting kinetic energy of π^0].

period can remove problems from gain drifts. Finally, obtained yield of the ${}^{4}_{\Lambda}$He(1^+ and 0^+) can be used to assign a γ-ray peak by comparing it with the expected yield from a DWIA calculation [26].

With these experimental advances, the present work succeeded in conclusively measuring the γ-ray transition energy to be 1406 $\pm$2 (stat.) $\pm$2 (syst.) keV, which supersedes the previously reported energy of 1150 $\pm$40 keV [14] and established the level scheme of ${}^{4}_{\Lambda}$He.

Chapter 2

Experiment

2.1 Overview of the experiment

A γ-ray spectroscopic experiment (J-PARC E13) was carried out at the K1.8 beam line in the J-PARC Hadron Experimental Facility [27]. The ^{4}He(K^-, π^-) reaction was used to produce $^4_\Lambda$He(1^+), which was populated via the spin-flip component of the elementary process, $K^- + n \to \Lambda + \pi^-$. A beam momentum of 1.5 GeV/c was chosen considering the elementary cross section of the spin-flip Λ production (see Fig.2.1) and the available beam intensity. A 2.8 g/cm^2-thick liquid ^{4}He was used as the experimental target. Incident K^- and outgoing π^- mesons were particle-identified and momentum-analyzed by the beam line spectrometer and the Superconducting Kaon Spectrometer (SKS) [28] (SksMinus setup), respectively. In addition, γ rays were detected by a Ge detector array (Hyperball-J) surrounding the target. Through a coincidence measurement between these spectrometer systems and Hyperball-J, γ rays from hypernuclei were measured. In total, 2.3×10^{10} kaons were irradiated to the target during $\sim$5 days beam time.

2.2 J-PARC K1.8 beam line

The J-PARC K1.8 beam line was constructed to carry out missing-mass spectroscopy of hypernuclei both for $S = -1$ and -2 sectors and exotic hadrons [28]. Secondary meson beams are produced at a primary target (Au, 66 mm thickness) placed at the most upstream in Hadron Experimental Facility (see Fig.2.2) by irradiating proton beam from J-PARC 30-GeV synchrotron. Secondary beams are delivered to the K1.8 beam line which was designed to provide separated pions and kaons with the momentum up to 2 GeV/c having $\pm3\%$ momentum bite. The K1.8 beam line is illustrated in Fig.2.3. For the kaon beam, good K/π separation with reasonable intensities is realized by removing pion contamination using two electrostatic separators (ESS1, ESS2) with a length of 6 m each and with mass slits installed at downstream of each separator. Furthermore,

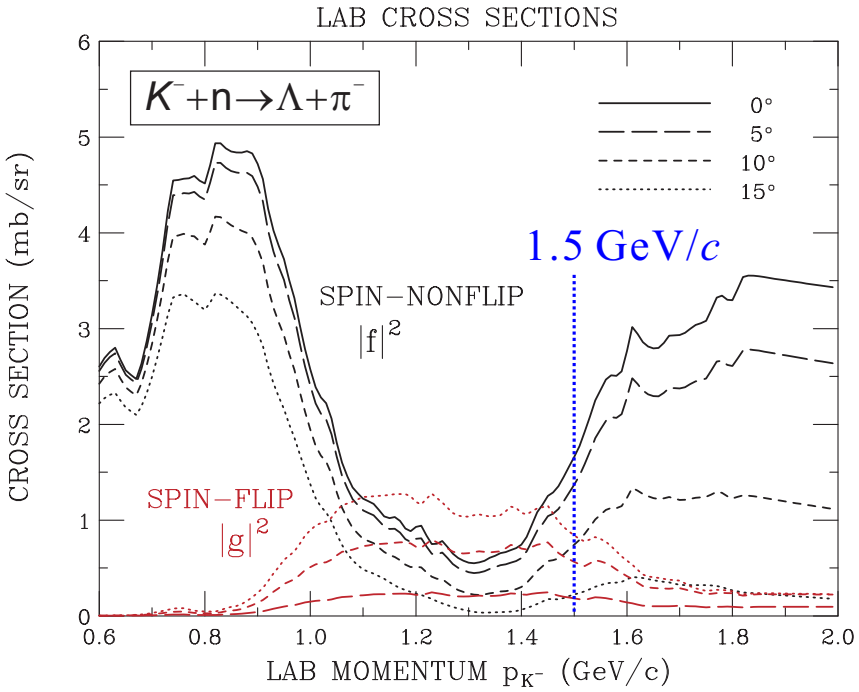

Figure 2.1: The cross section of the $K^- + n \to \Lambda + \pi^-$ reaction as a function of the beam momentum based on a analysis of experimental data with bubble chamber technique [26]. The beam momentum of 1.5 GeV/c was selected because of the relatively large spin-flip cross section at p_{K^-}=1.0–1.5 GeV/c region as well as the beam intensity.

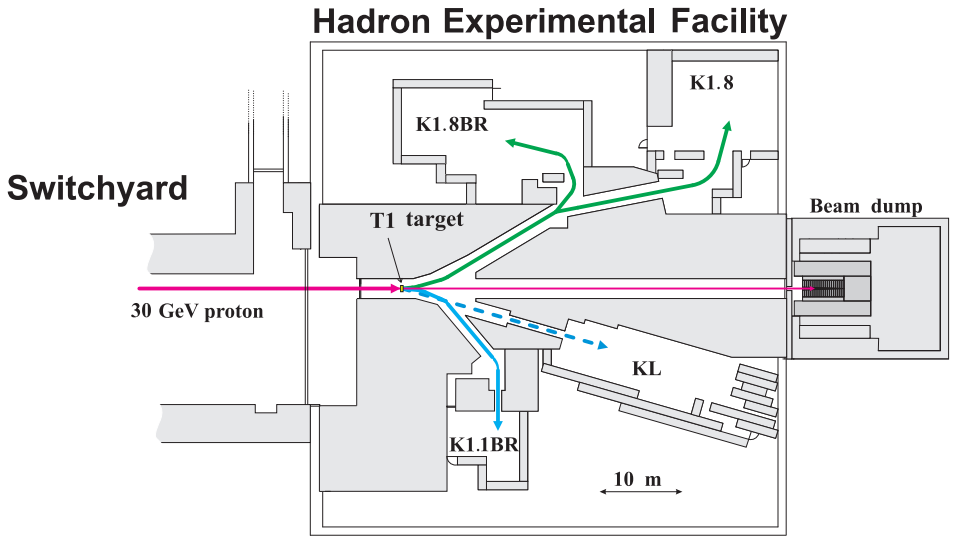

Figure 2.2: Schematic view of J-PARC Hadron Experimental Facility [27].

intermediate focus (IF) slits reject cloud pions generated near the primary target. The length between the primary target and the experimental target is ∼46 m.

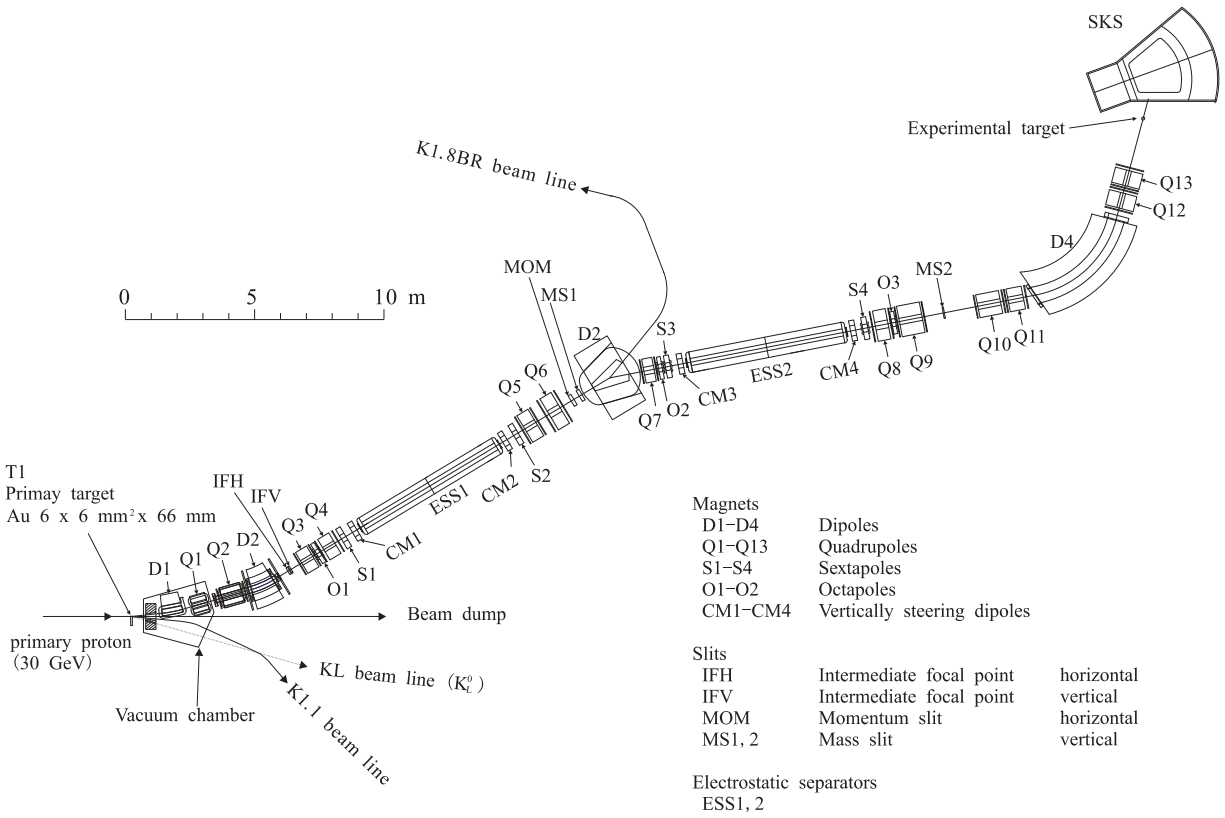

Figure 2.3: Schematic view of the J-PARC K1.8 beam line [27].

At the experimental period, the repetition rate of the beam spill was 6.0 s, and the beam duration time was 2.1 s. Typically, 2.5×10^{13} protons per spill were irradiated on the primary target in the 24-kW accelerator operation. ESS1 and ESS2 were operated at $\pm$250 kV applied over the 10-cm gap. The beam tuning for K^- was carried out so as to maximize hypernuclear production yield considering the K^- intensity with reasonable K^-/π^- ratio. The scanned parameters are (1) currents for all the Dipole-, Quadrupole-, Sextapole-magnets, (2) currents for the correction magnets installed at both ends of each ESS1 and ESS2, (3) opening widths of the IF slits and the mass slits. With the optimized beam line magnet parameters, the K^- intensity at the experimental target was 3 $\times 10^5$ per spill with a K^-/π^- ratio of 2–3 for $p_{K^-} = 1.5$ GeV/c. The contamination of $\overline{p}$ in K^- beam is negligibly small. A typical beam size at the experimental target is 2.4 cm (horizontal) $\times$ 0.5 cm (vertical) in rms as shown in Fig. 2.4. The specification of the K1.8 beam line is summarized in Table 2.2.1, and the experimental beam condition is summarized in Table 2.2.2.

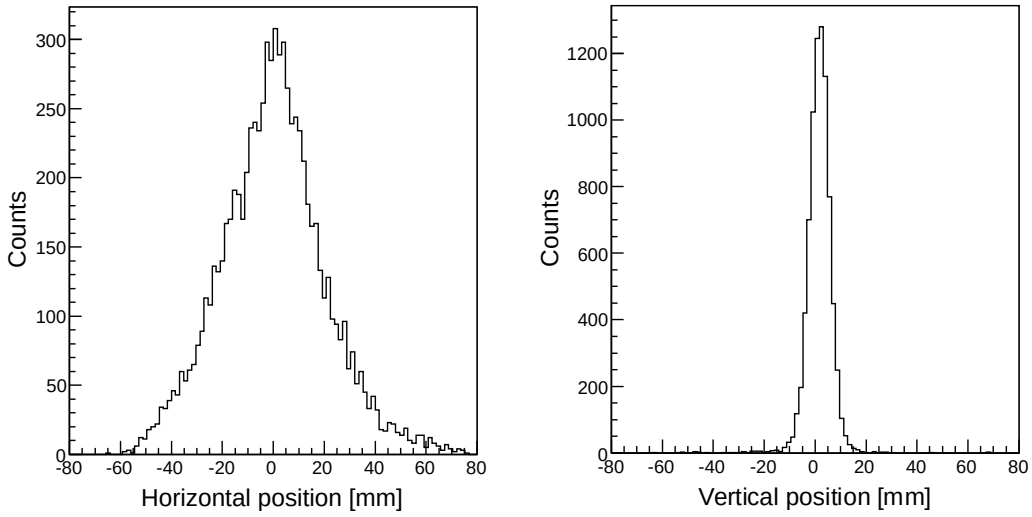

Figure 2.4: Typical beam profile at the experimental target.

Table 2.2.1: Specifications of the K1.8 beam line.

Maximum momentum	2.0 GeV/c
Production target	gold
Target thickness	66 mm
Production angle	6°
Momentum bite	±3%
Beam line length	46 m

Table 2.2.2: Experimental beam condition.

Primary proton momentum	30 GeV/c
Primary proton intensity	2.5×10^{13} /spill
Repetition cycle	6 s
Spill length	2.1 s
Secondary K^- momentum	1.52 GeV/c
Secondary K^- intensity	$\sim 3 \times 10^5$ /spill
K^-/π^-	2–3

2.3 Spectrometer system

Events from the ^{4}He$(K^-, \pi^-)^4_\Lambda$He reaction were identified by two magnetic spectrometers; incident kaons and scattered pions were particle identified and momentum analyzed by the beam line spectrometer and the SksMinus spectrometer, respectively, in order to calculate missing mass for the ^{4}He$(K^-, \pi^-)X$ kinematics. Figure 2.5 shows the experimental setup.

2.3.1 Beam line spectrometer

For the momentum-analysis of beam particles, the beam line spectrometer consists of QQDQQ magnets, detectors for time-of-flight (BH1,2) and tracking (BFT, BC3,4). The incident K^- momentum was reconstructed using a third-order beam transport matrix with a hit position in BFT at the upstream of the magnets and a straight track measured by BC3 and BC4 at the downstream. In order to minimize the multiple scattering effect on the momentum resolution, the beam line spectrometer was designed so that the $< x|\theta >$ term of the transport matrix is almost zero. In addition, the beam pipe in QQDQQ magnets was vacuated with SUS windows of 0.1 mm thickness. The designed momentum resolution is 3.3×10^{-3} (FWHM) with the position accuracy of 0.2 mm (rms) for a measured beam trajectory [28]. Specifications of the beam line spectrometer are listed in Table 2.3.1.

Table 2.3.1: Specifications of the beam line spectrometer.

Momentum resolution	3.3×10^{-4} (FWHM)
Maximum momentum	2.0 GeV/c
Bending angle	60°
Flight path	11.2 m
Effective length (D4)	4 m

Counters for particle identification

Even thought beam particles were separated by the electrostatic separators, particles $(e^-, \mu^-, \pi^-, \bar{p}, ...)$ other than K^- were contaminated in the beam and transported to the experimental target. Therefore, the beam line spectrometer has to be equipped with counters for particle identification. Incident kaons were particle-identified by aerogel Čerenkov counters at the trigger level and by the time-of-flight method in the off-line analysis.

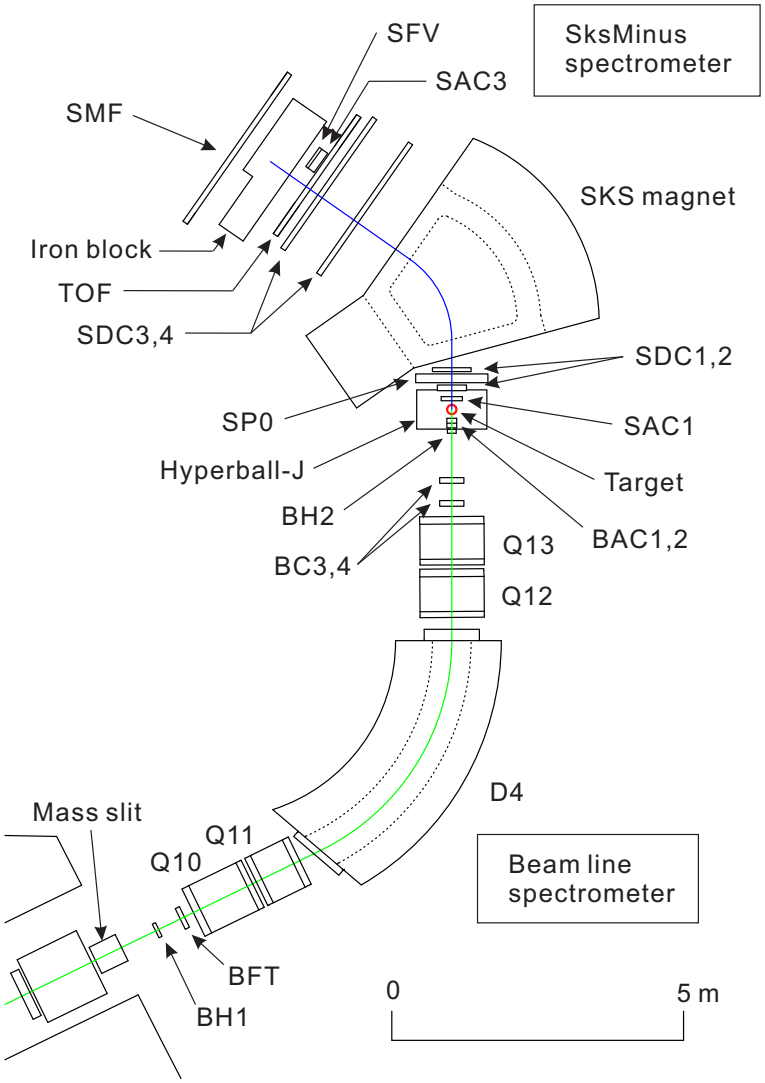

Figure 2.5: Schematic view of the K1.8/SksMinus spectrometers. The beam line spectrometer consists of QQDQQ magnets and tracking detectors (scintillation fiber detector: BFT, drift chambers: BC3–4). Plastic scintillation (BH1,2, TOF, SFV) and aerogel Čerenkov counters (BAC1,2, SAC1,3) are used for the trigger. SksMinus consists of superconducting dipole magnet (SKS), drift chambers (SDC1–4) and decay-particle suppression counters (SMF, SP0). In the γ-ray spectroscopic experiment, γ rays from hypernuclei are detected by a Ge detector array (Hyperball-J) placed around the target in coincidence with the (K^-, π^-) reaction. SFV and SAC3 are located at the beam-through region for p_K =1.8 GeV/c in the figure.

Time-of-flight counters

BH1 and BH2 are plastic scintillation counters which are horizontally segmented. Beam particles were identified by the time-of-flight method with a typical flight length of 11 m (BH1–BH2). The corresponding time difference between kaon and pion is 1.8 ns with a momentum of 1.5 GeV/c. Figure 2.6 shows a time-of-flight (=BH2−BH1) distribution

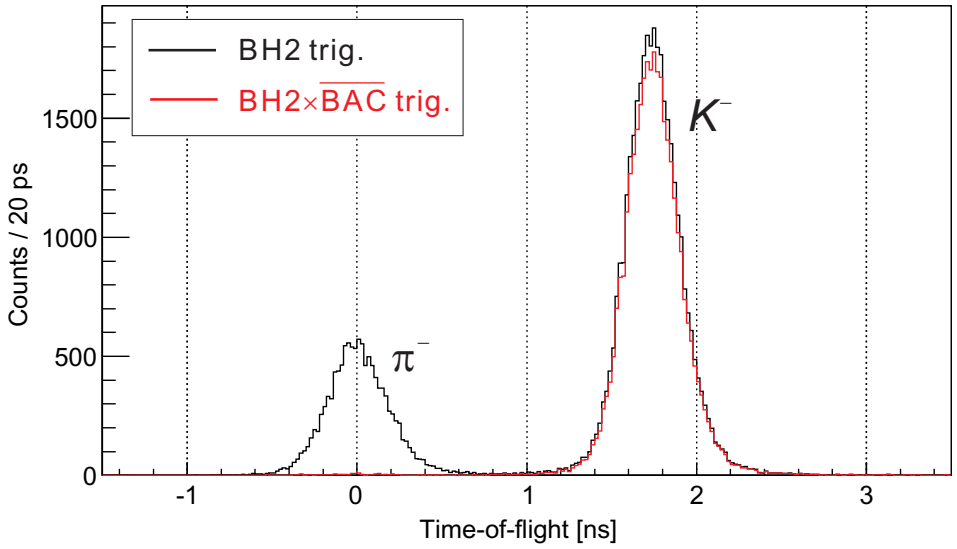

Figure 2.6: A time-of-flight (=BH2−BH1) distribution with a typical beam condition. Black and red lines show the distributions with the BH2×$\overline{\text{BAC1}}$ × $\overline{\text{BAC2}}$ trigger, respectively.

with a typical beam condition. The time-of-flight resolution is 155 ps (rms) for the K^- peak. BH2 is used as a timing reference counter for all other detectors. For BH2, photomultiplier tubes (PMTs) are mounted only on the bottom side in order to avoid interference with the cryogenic system of the liquid He target. Specifications of these counters are listed in Table 2.3.2.

Aerogel Čerenkov counters

Threshold-type aerogel Čerenkov counters (BAC1 and BAC2) were installed at the upstream of the experimental target. These counters are placed as close to the target as possible to minimize contamination from beam K^- decay events in the trigger. Figure 2.7 shows the refractive index threshold for Čerenkov radiation as a function of momentum. The refractive index was chosen to be 1.03, corresponding to the threshold momentum of 0.6 GeV/c for pions and 2.0 GeV/c for kaons. Figure 2.8 shows a schematic view of BAC1,2. BACs cover 160 × 52 mm^2 area with a 66-mm thick silica aerogel radiator, of which length was optimized. Polytetrafluoroethylene $(CF_2)_n$ was chosen as an inner diffused-type reflector. For BACs, three 2" fine-mesh type PMTs, Hamamatsu H6614-70UV, were connected to the radiator directly. By summing up analog signals from PMTs before discriminators, K/π separation was improved. Two counters (BAC1 and BAC2) were used because beam pions that were miss-identified as kaons directly increase the trigger rate. The beam K^- trigger ("K_{in} trigger") was defined as BH2×$\overline{\text{BAC1}}$ × $\overline{\text{BAC2}}$

Table 2.3.2: Specifications of counters for particle identification

Detector	Effective area W × H × T [mm]	Spec.	PMT (Hamamatsu)
BH1	170 × 66 × 5	11 segments, double-side readout, booster	H6524MOD
BH2	111 × 50 × 8	5 segments, single-side readout, booster	H6524MOD
BAC1	160 × 57 × 66	1 segment, 3 PMTs readout	H6614-70UV
BAC2	160 × 57 × 66	1 segment, 3 PMTs readout	H6614-70UV
SAC1	342 × 80 × 66	1 segment, 5 PMTs readout	H6614-70UV
TOF	2240 × 1000 × 30	32 segments, double-side readout	H1949
SFV	400 × 200 × 8	6 segments, single-side readout	H3167
SAC3	400 × 200 × 120	1 segment, 16 PMTs readout	R6681
SP0	1200 × 1100 × 8 (×8 layers)	6 segments, 8 layers, double-side readout	R980
SMF	2800 × 1400 × 40	28 segments, double-side readout	H1949, H6410

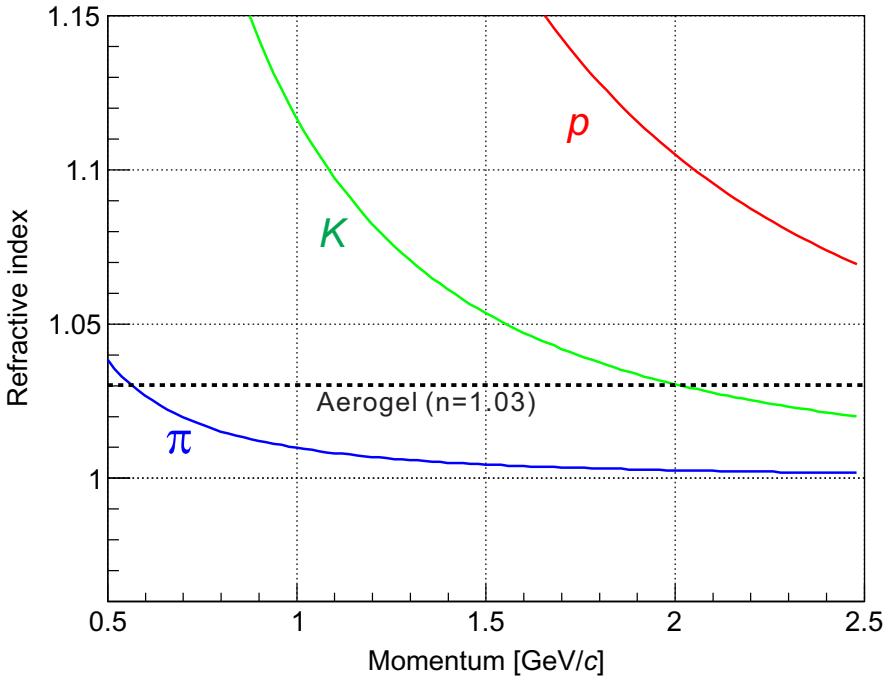

Figure 2.7: Threshold of refractive index for Čerenkov radiation as a function of momentum. Silica aerogel of n=1.03 was chosen as a radiator for K/π separation at ∼1.5 GeV/c.

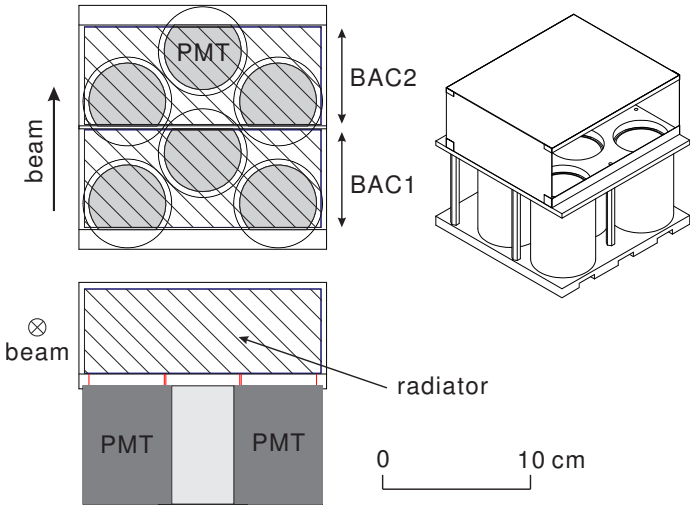

Figure 2.8: Schematic view of BAC1,2. An effective area is 160 × 52 mm^2 with a 66-mm thick silica aerogel radiator (n = 1.03). Three 2" fine-mesh type PMTs, Hamamatsu H6614-70UV, are connected on the radiator directly.

(see Section 2.5 for description of the trigger system). In a typical beam condition with p_{K^-} = 1.5 GeV/c, the $K_{\rm in}$ trigger efficiency was more than 95% with a π^- beam miss-identification ratio of less than 3% in the trigger level as shown together in Fig. 2.6. The numbers of photo-electron were measured to be ∼20 par detector.

Tracking detectors

One scintillation fiber counter (BFT) and two multi-wire drift chambers (BC3,4) were used to measure the beam particle track. BFT was placed at the upstream of the QQDQQ magnets, and BC3,4 were placed at the downstream of these magnets. The momenta of the beam particles were determined by using track information from these detectors. Table 2.3.3 shows specifications of the tracking detectors. BFT was a set of 1 mmϕ scintillation fibers arranged horizontally in two layers(xx') as shown in Fig. 2.9 [29]. Multi-Pixel Photon Counter (MPPC) devices were connected to each fiber. The drift chambers, BC3,4, have six layers of sense-wire plane ($xx'uu'vv'$). x, u and v denote a vertical wire plane and a wire plane tilted by ± 15°, respectively. BC3,4 have a drift length of 1.5 mm with a typical position resolution of 0.2 mm (σ) for a sense plane as shown in Fig. 2.10. These detectors were designed to be operational in high rate beam conditions. The gas mixture used was Ar: C_4H_{10}: Methylal = 76: 20: 4 at atmospheric pressure.

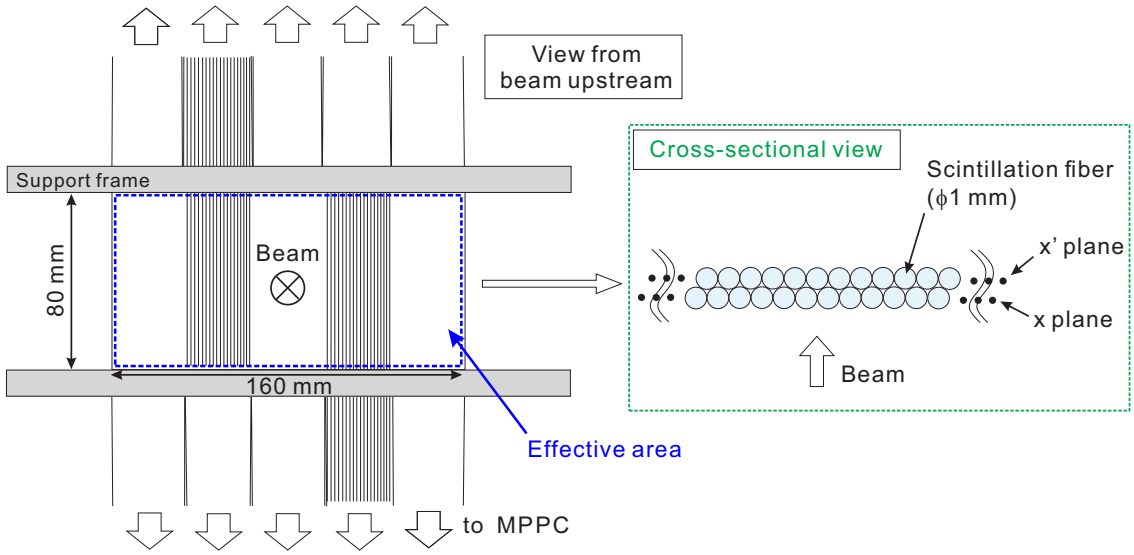

Figure 2.9: Schematic view of BFT. BFT was a set of 1 mmϕ scintillation fibers arranged horizontally in two layers(xx'). MPPC devices were connected to each fiber.

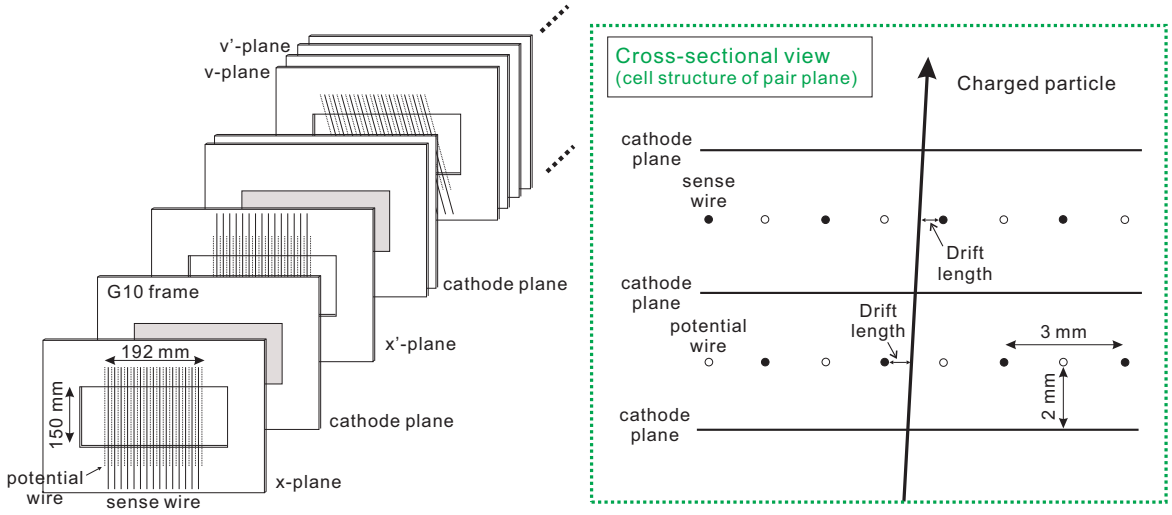

Figure 2.10: Schematic view of BC3.

2.3.2 Scattered particle spectrometer with SKS (SksMinus setting)

Scattered π^- mesons were particle-identified and momentum-analyzed by the magnetic spectrometer called SksMinus. SksMinus was designed for γ-ray spectroscopy via the (K^-, π^-) reaction. A wide solid angle of the scattered particle spectrometer is essential for the coincidence experiment. Therefore, we chose the superconducting kaon spectrometer (SKS) magnet, which was used for reaction spectroscopy experiments at the

Table 2.3.3: Specifications of the tracking detectors. BFT is a scintillation fiber detector and others are drift chambers. Typical position resolutions for a sense plane are listed.

Detector	Effective area W × H [mm]	Planes	Tilted angle (x, x') [deg.]	Diameter [mm]	resolution σ[mm]
BFT	160 × 80	xx'	0	1.0	0.15
Detector	Effective area W × H [mm]	Planes	Tilted angle (x, u, v) [deg.]	Drift length [mm]	resolution σ[mm]
BC3	192 × 150	$xx'vv'uu'$	0, +15, −15	1.5	0.20
BC4	192 × 150	$uu'vv'xx'$	0, +15, −15	1.5	0.20
SDC1	400 × 150	$xx'vv'uu'$	0, +15, −15	2.5	0.20
SDC2	560 × 150	$uu'xx'$	0, +15, −15	2.5	0.15
SDC3	2140 × 1140	$vxuvxu$	0, +30, −30	10.0	0.25
SDC4	2140 × 1140	$vxuvxu$	0, +30, −30	10.0	0.25

KEK K6 beam line [30] as well as at the J-PARC K1.8 beam line [31], with a modified detector configuration from the original setup [30]; (1) an incident angle with respect to the magnet edge is shallower, (2) detectors have a larger effective area to accept non focused trajectories of scattered particles as shown in Fig.2.11. The features of SksMinus are listed as follow:

- a wide momentum acceptance to cover a momentum range of 1.1–2.0 GeV/c which allows us to change the K^- beam momentum without modifying the spectrometer setup,
- a wide angular acceptance (0–20°) which allows for identification of directly populated states of hypernuclei from angular distribution, $\theta_{K\pi}$, characterized by angular momentum transfer, $(\Delta L = 0, 1, 2, \cdots)$,
- good missing mass resolution (∼5 MeV(FWHM)) to select hypernuclear production events,
- equipped with counters for particle identification which distinguish between kaons and pions in the on-line and the off-line levels, and
- equipped with detectors to suppress background events from decay of beam K^-.

SksMinus achieves a good momentum resolution of 0.3% (FWHM) and a large solid angle of 100 msr. Kaons and pions can be identified using threshold-type Čerenkov counters and time-of-flight counters. Furthermore, two types of background suppression detectors, namely SP0 and SMF, for beam kaon decay events were introduced. Specifications of SksMinus are summarized in Table 2.3.4.

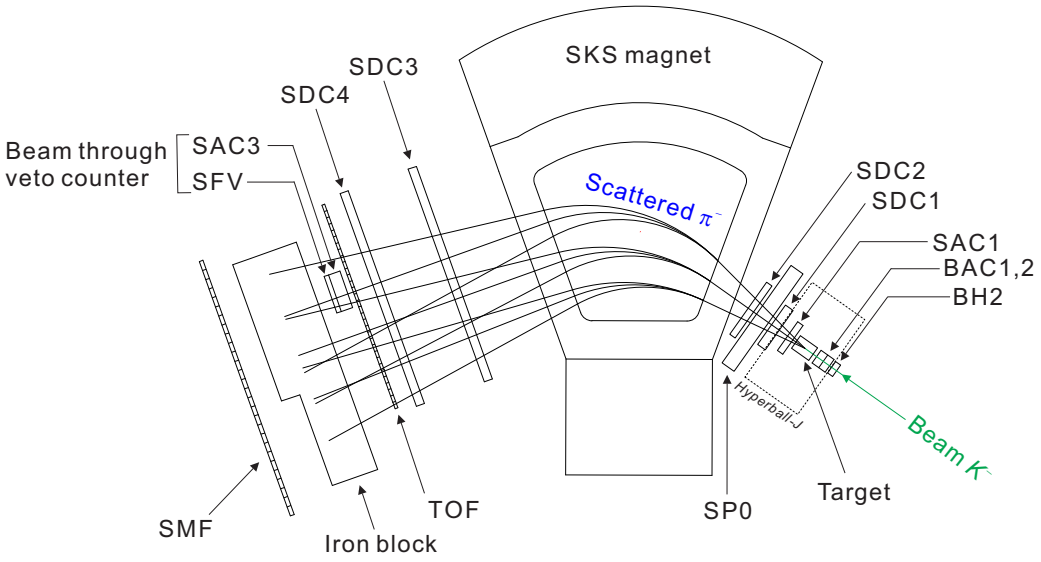

Figure 2.11: Schematic view of the SksMinus setup. Plastic scintillation (BH2, TOF, SFV) and aerogel Čerenkov counters (BAC1,2, SAC1,3) are used for the trigger. SksMinus consists of superconducting dipole magnet (SKS), drift chambers (SDC1–4) and decay-particle suppression counters (SMF, SP0). SFV and SAC3 are located at the beam-through region for p_K =1.8 GeV/c in the figure.

Table 2.3.4: Specifications of SksMinus.

Momentum acceptance	1.1 $\sim$ 2.0 GeV/c
Momentum resolution	0.3% (for 1.5 GeV/c)
Bending angle	55° (for 1.5 GeV/c)
Magnetic field (at center)	2.5 T
Solid angle	100 msr
Flight path	$\sim$ 5 m

SksMinus consisted of a superconducting dipole magnet, four sets of drift chambers (SDC1,2,3,4), three kinds of trigger counters (SAC1, TOF, beam-through veto counter) and two kinds of counters for K^- beam decay suppression (SP0 and SMF) as shown in Fig.2.5. SksMinus accepts scattering angles of $\pm$20° in the horizontal direction and $\pm$5° in the vertical direction. In the hypernuclear γ-ray experiment, the SKS magnet was operated at 2.5 T (400 A) in which scattered particles were bent by about 55° horizontally for a momentum of 1.4 GeV/c, which is typical value for pions produced in the ^{4}He$(K^-,\pi^-)^4_\Lambda$He reaction with a 1.5 GeV/c beam. Figure 2.12 shows the acceptance probability map of SksMinus as a function of the scattered particle momentum and the scattering angle which is estimated by a Monte Carlo simulation using the Geant4 code [32]. This system covered a momentum range of 1.1–2.0 GeV/c and 0°–20° scatter-

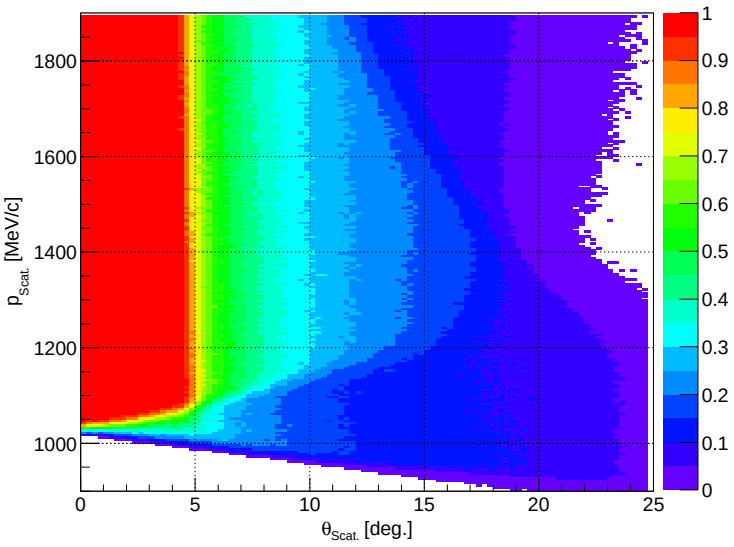

Figure 2.12: Accept probability map of the SksMinus as a function of the scattering angle ($\theta_{K\pi}$) and the momentum ($p_{scat.}$) of scattering particles. The spectrometer has a angular acceptance of 0°–20° and a momentum acceptance of 1.1–2.0 GeV/c.

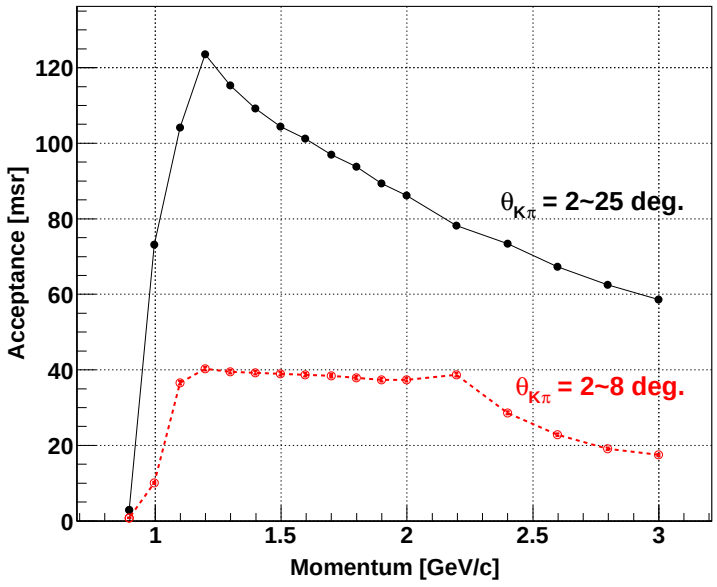

Figure 2.13: Solid angle of the SksMinus for the hypernuclear production kinematics as a function of the beam momentum, shown for all scattering angles (black solid line) and forward angles (red dotted line).

ing angles. Figure 2.13 shows the solid angle of SksMinus for hypernuclear production kinematics as a function of the beam momentum; the forward angles less than 2° were

excluded because events in this region will be rejected in the off-line analysis due to a worse vertex resolution and thus a larger background ratio than the other angles. The system had a solid angle of ∼100 msr for hypernuclear production at p_{K^-}=1.5 GeV/c, for $\theta_{K\pi} > 2^\circ$. Because of the wide momentum acceptance, this spectrometer can be utilized for hypernuclear production via the (K^-, π^-) reaction with a wide beam K^- momentum range of 1.2–2.1 GeV/c. The wide angular acceptance allowed for measurement of angular distribution of scattered π^- without changing the magnet position. The trajectory of scattered π^- was reconstructed by the Runge-Kutta method [33] based on position information measured by the drift chambers at upstream (SDC1,2) and downstream (SDC3,4) of the SKS magnet using the magnetic field distribution calculated by the TOSCA code [34]. The design value of the momentum resolution is 0.2%. The magnetic field was monitored with a NMR probe during the data taking to correct for the fluctuation of the actual field. The SKS pole gap is filled with He gas contained in a bag with 16 μm-thick Mylar windows to reduce multiple scattering.

Counters for particle identification

In order to identify the (K^-, π^-) reaction events from a huge amount of background events such as the beam K^- passing-through events, SksMinus has counters for particle identification. Scattered pions were particle-identified by a aerogel Čerenkov counter (SAC1) in the trigger level and by time-of-flight method in the off-line analysis.

Time-of-flight counters

TOF is a set of plastic scintillation counters which is horizontally segmented. Scattered particles were identified by the time-of-flight method with a typical flight length of 5 m (BH2–TOF). Corresponding time difference between kaon and pion was ∼0.7 ns for a momentum of 1.5 GeV/c. The specification of TOF is listed in Table 2.3.2.

Aerogel Čerenkov counters

A threshold-type aerogel Čerenkov counter (SAC1) was installed at the downstream of the experimental target. The refractive index was 1.03. Figure 2.14 shows a schematic view of SAC1. SAC1 covers a 342 × 80 mm^2 area with a 66-mm thick silica aerogel radiator. Polytetrafluoroethylene $(CF_2)_n$ was chosen as inner diffused-type reflector. Five 2" fine-mesh type PMTs, Hamamatsu H6614-70UV, were connected to the radiator directly. The analog signals from the five PMTs were summed up before discriminators.

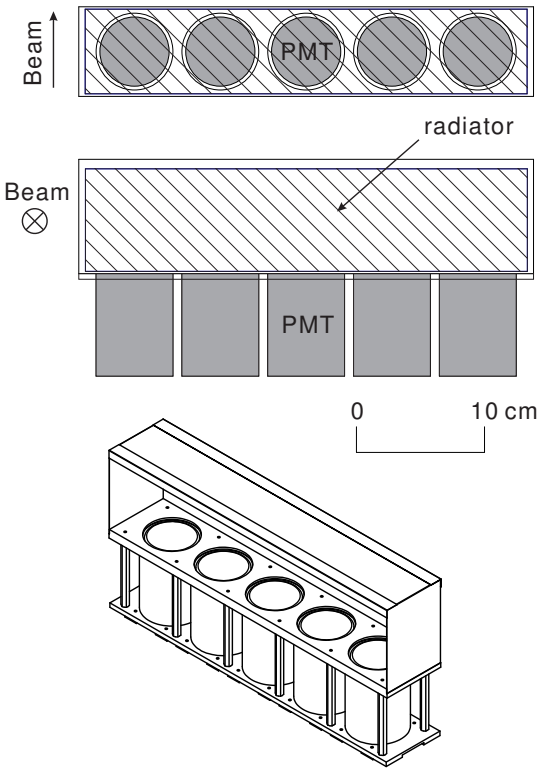

Figure 2.14: Schematic view of SAC1. An effective area was 342 × 80 mm^2 with a 66-mm thick silica aerogel radiator ($n = 1.03$). Five 2" fine-mesh type PMTs, Hamamatsu H6614-70UV, were connected on the radiator directly.

Tracking detectors

The drift chambers SDC1 and SDC2 were placed at the upstream of the SKS magnet. SDC1, 2 had a drift length of 2.5 mm with a position resolution of less than 0.2 mm (σ). SDC1 had six layers of the sense-wire plane ($xx'uu'vv'$) and SDC2 had four layers of the sense-wire plane ($uu'xx'$). x, u and v denote a vertical wire plane and a wire plane tilted by $\pm$ 15°, respectively.

The drift chambers SDC3 and SDC4 were placed at the downstream of the SKS magnet. SDC3, 4 had a drift length of 10 mm with a position resolution of 0.25 mm (σ). Both SDC3 and SDC4 had six layers of the sense-wire plane ($vxuvxu$). x, u and v denote a vertical wire plane and a wire plane tilted by $\pm$ 30°, respectively. SDC3,4 were previously used in BNL [4] and PSI [35], respectively.

The gas mixture in use is Ar:C_4H_{10}:Methylal = 76:20:4 for SDC1,2 and Ar:C_2H_6 = 50:50 for SDC3,4 at atmospheric pressure. These detectors had effective areas wide enough to cover the scattered particle profile with scattering angles of 0–20°. Specifications of SDCs are summarized in Table 2.3.3.

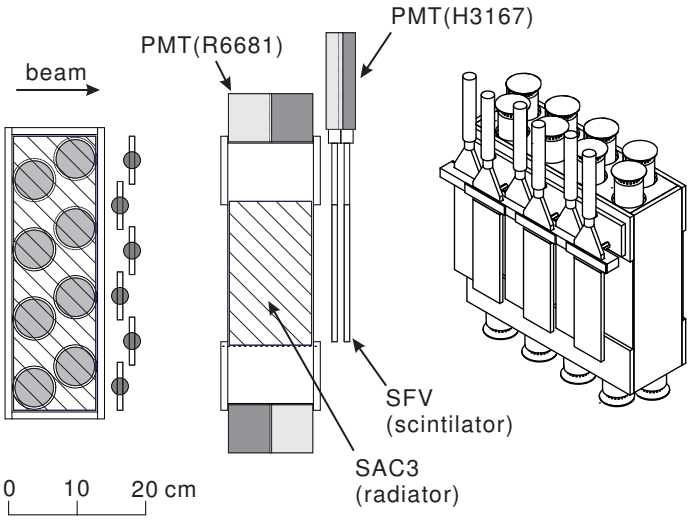

Figure 2.15: Schematic view of the beam-through veto counter (SFV and SAC3). SFV is a segmented plastic scintillation counter, and SAC3 is an aerogel Čerenkov counter using silica aerogel radiator ($n = 1.028$).

Beam-through veto counter

The "beam-through veto counter" system was introduced to suppress kaons miss-identified as pions by SAC1 instead of using two sets of SAC counters. The system was placed at the downstream of all the tracking detectors to reduce amount of material on the scattered particle trajectory. The system consisted of a scintillator hodoscope (SFV) and an aerogel Čerenkov counter (SAC3). Kaon beam-through events were suppressed at the trigger level, while scattered pions which passed through the counter were not masked by using SAC3 hit information. Figure 2.15 shows a schematic view of the beam-through veto counter. SFV is a segmented plastic scintillation counter with an effective area of 400×200 mm^2 which covers the kaon beam size. SAC3 is an aerogel Čerenkov counter and distinguishes between kaons and pions using $n = 1.028$ silica aerogel with a thickness of 120 mm. The aerogel radiator and the PMTs for SAC3 were previously used in the Belle experiment [36]. The analog signals from the PMTs were summed up as for the other ACs. The K^- beam-through trigger logic was defined as SFV $\times \overline{\text{SAC3}}$.

2.3.3 Beam-decay suppression detectors

Beam kaons decay in two dominant channels, $K^- \to \pi^- + \pi^0$ (21%) and $K^- \to \mu^- + \overline{\nu_\mu}$ (64%). When kaons decay between BACs and SAC1, they are identified as the (K^-, π^-) events in the trigger level. Such events constitute a large amount of fake triggers. In addition, these events cannot be eliminated in the missing mass as well as in the γ-ray spectrum. Figure 2.16 shows correlation between the momentum and the scattering an-

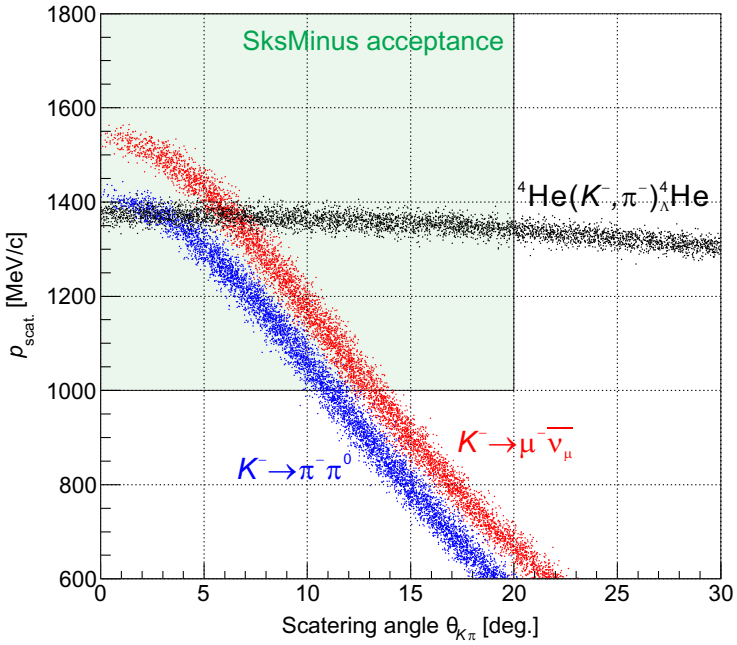

Figure 2.16: Correlation between $p_{scat.}$ and $\theta_{K\pi}$ for hypernuclear production [^{4}He(K^-,π^-)$^4_\Lambda$He] events and beam kaon decay events with p_K=1.5 GeV/c. Decay events kinematically overlap with hypernuclear production events in the forward angle region (0–7°).

gle ($\theta_{K\pi}$) for hypernuclear production and beam kaon decays at p_{K^-}=1.5 GeV/c. In scattering angles of 0–7°, the decay events overlap with the hypernuclear production events, and thus they can not be separated kinematically. Because the number of the K^- decay events is much larger than that of the hypernuclear production events, contamination from the decay events is a serious problem as in previous experiments using the (K^-,π^-) reaction [4, 37]. For this reason, the decay suppression counters (SP0, SMF) were introduced to suppress the background events due to the beam K^- decay.

SP0 can reject $K^- \to \pi^- + \pi^0$ decay events by tagging an electromagnetic shower caused by high energy γ rays from π^0 decay. Figure 2.17 shows a schematic view of SP0. The detector consisted of 8 layers of segmented plastic scintillators (t=8 mm) with lead plates (t=4 mm) as converter in between. The number of layers and their thickness were optimized by Monte Carlo simulation. The response of the whole detector was measured in advance with $e^\pm$ and neutron beams. The effective area was 1200 × 1100 mm^2 with a 400 × 120 mm^2 hole for scattered π^- to go through. Electromagnetic showers from $\pi^0 \to 2\gamma$ hit 5 layers on average while other hadronic particles from hypernuclear decay hit less than 2 layers, typically. Therefore, $K^- \to \pi^- + \pi^0$ decay events are suppressed by selecting the number of hit layers larger than 3 or 4 with a small chance of miss-

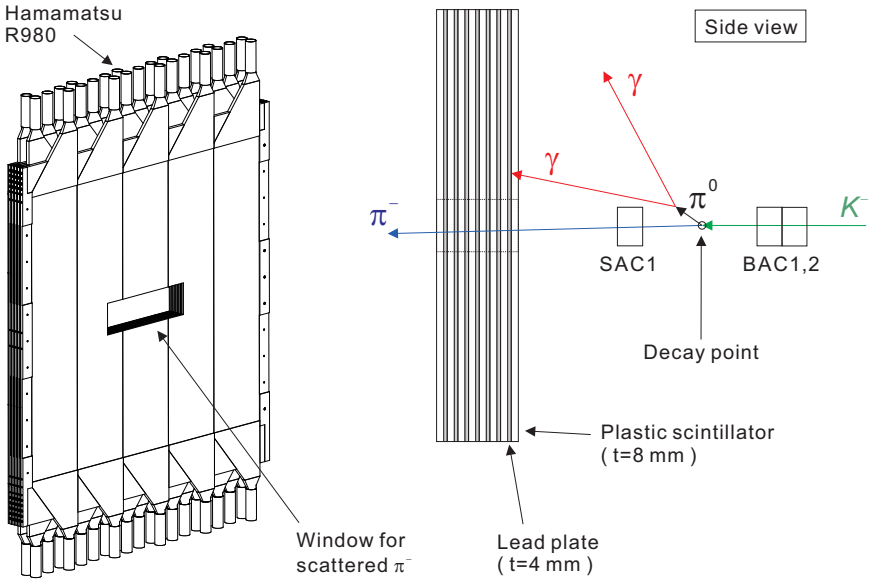

Figure 2.17: Schematic view of SP0. The detector consists of 8 layers of segmented plastic scintillators (t=8 mm) with lead plates (t=4 mm) between each scintillator layer as a converter. The effective area is 1200 × 1100 mm^2 with a 400 × 120 mm^2 hole corresponding to the acceptance of scattered π^-.

identification to other particles. Hypernuclear decay events with the π^0 emission are also rejected by SP0. However, the loss of hypernuclear events is small due to a low branching ratio of π^0 emission channel in hypernuclear decay. Signals of each scintillator segment were read out by PMTs (Hamamatsu R980). Those scintillation counters were the ones previously used at KEK [38].

SMF can reject $K^- \to \mu^- + \overline{\nu_\mu}$ decay events by distinguishing μ^- and the scattered π^- from hypernuclear production reaction. SMF consists of 50–70 cm-thick iron blocks and a lucite Čerenkov counter hodoscope. μ^- passes through the iron block while π^- is absorbed with hadronic interactions. Therefore, the decay events can be suppressed by detecting outgoing μ^- at the downstream of the iron block. Figure 2.18 shows distribution for a stopped/absorbed position of the scattered π^- and μ^- in an infinite thickness of iron. The size of the iron block was determined to optimize the μ^-/π^- separation. The hodoscope, which was previously used in other experiments at J-PARC [31, 39, 40, 41], consists of 28 vertical segments with an effective area of 2800 × 1400 mm^2. Signals of each segment are read out by PMTs (Hamamatsu H1949 and H6410) on the top and bottom ends. It is noted that some neutrons and γ rays caused by absorption of π^- in the iron block hit to the hodoscope and lead a overkill of π^- (see Section 3.9 about the overkill ratio).

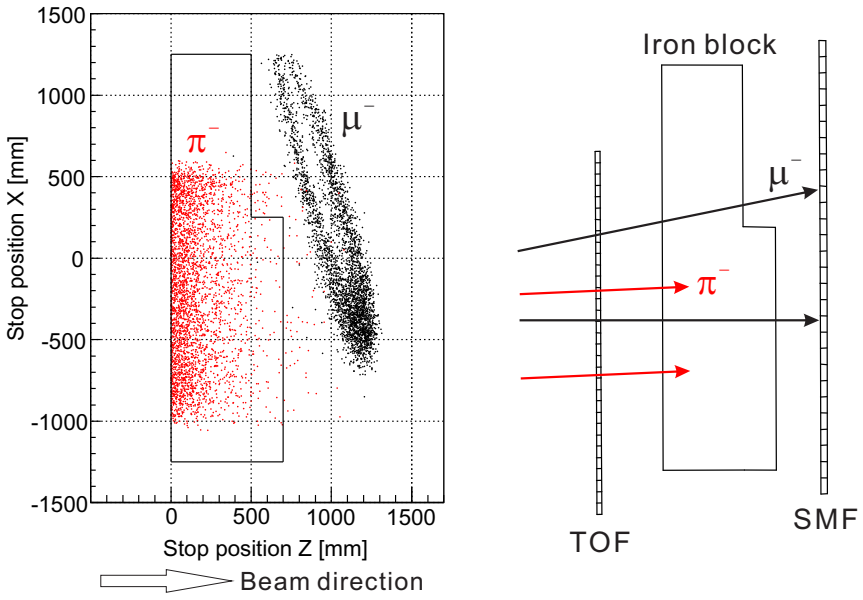

Figure 2.18: Simulated stopped/absorbed position of μ^- from the K^- decay (black points) and π^- from the hypernuclear production (red points) in iron. Particles are incident in +z direction, and z=0 corresponds to the iron block surface. Shape of the iron block was optimized as shown in the solid line considering passing-through probability for pions and muons. Two lines appear in the μ^- distribution which come from muons go to right side and left side of the SKS magnet.

2.4 Hyperball-J

Hyperball-J is a newly developed Ge detector array for hypernuclear γ-ray spectroscopy [42]. The array can be used under high intensity hadron beam conditions by adopting mechanical cooling of the Ge detectors [43]. The array consisted of 27 Ge detectors in total, equipped with PWO counters surrounding each Ge crystal to suppress background events such as Compton scattering and high energy photons from π^0 decay.

Figure 2.19 shows a schematic view of the lower half of Hyperball-J and Ge + PWO detector units. Figure 2.20 shows the detector arrangement of Hyperball-J. There are four types of a Ge + PWO detector unit (B-, E-, C-, L-type). In the original design, each half of Hyperball-J (the upper half and the lower half) had one set of the B-type detector unit, four sets of the E-type detector unit, two sets of the C-type detector unit and four sets of the L-type detector unit. In total, 32 Ge detectors can be mounted to Hyperball-J (16 detectors for each half). The detector units were mounted to vertically movable frames, which allow for various detector arrangement.

In the present experiment, the detector configuration of Hyperball-J was arranged so

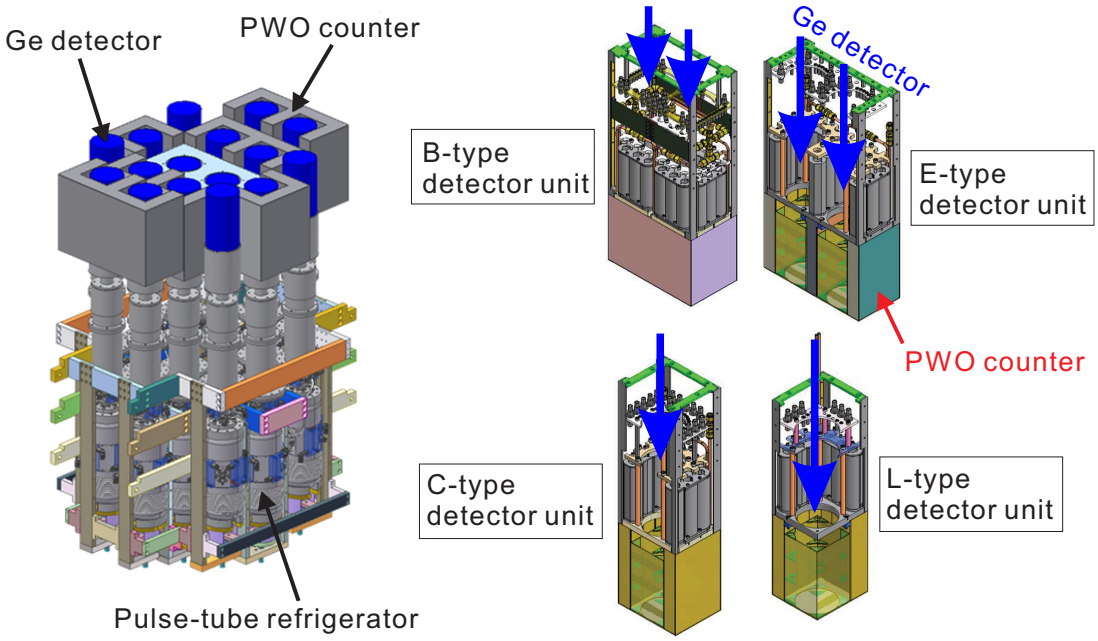

Figure 2.19: Schematic view of the lower half of Hyperball-J and the Ge + PWO detector units. The array consists of Ge detectors cooled by a pulse-tube refrigerator and of PWO counters.

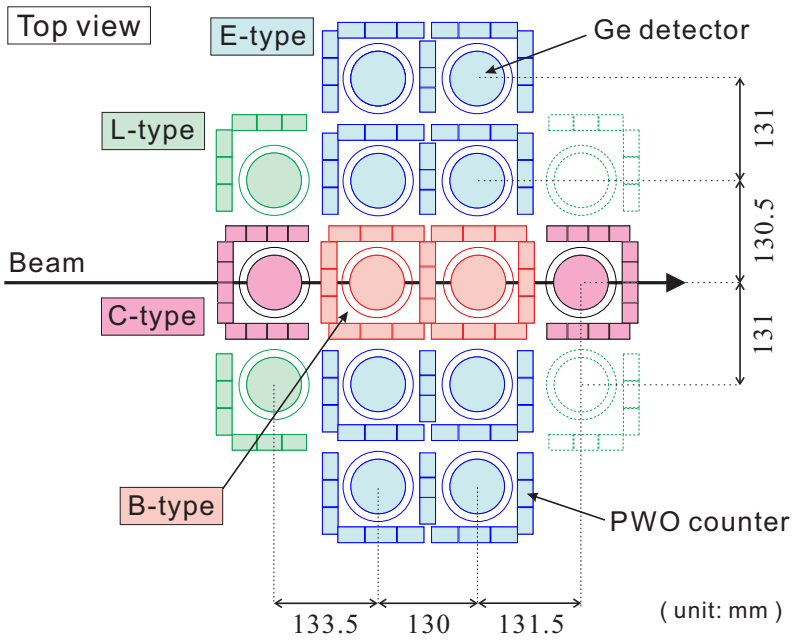

Figure 2.20: Schematic view of the Hyperball-J detector configuration.

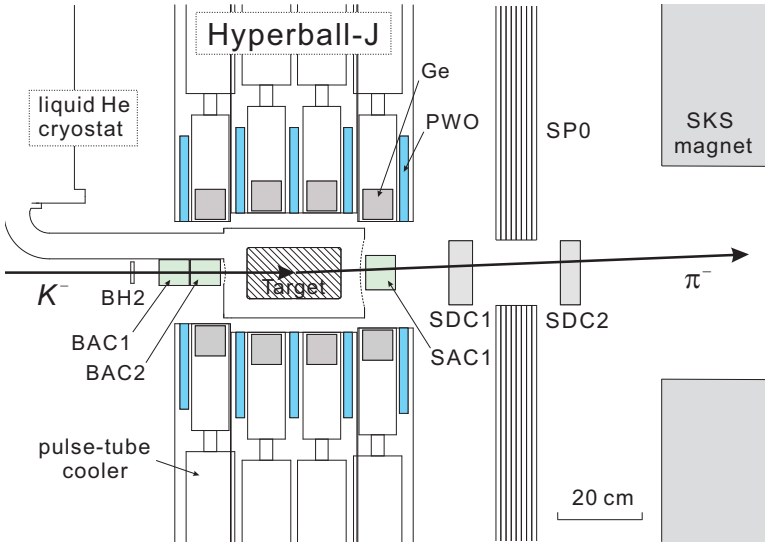

Figure 2.21: Schematic side view of the detector system around the experimental target.

as to avoid interferences between Hyperball-J detectors, trigger counters and a cryogenic system of the liquid helium target. Figure 2.21 shows a schematic side view of the detector system around the experimental target. Differences between the standard configuration and the present setting are listed below.

- Four L-type detector (downstream side) units were not installed.
- All of the C- and L-type units were moved vertically by 5–7 cm away from beam plane.

The distance between a Ge detector housed in the B-type unit and the target was 14 cm. The Ge crystals covered a total solid angle of $0.24\times4\pi$ sr for the source point at the center.

2.4.1 Ge detectors

The Ge detectors were of coaxial type with a typical size of $\phi 70 \times 70^L$ mm^3. The relative efficiency with respect to a ϕ3"×3" NaI(Tl) counter was ∼60%. Features of the Ge detectors are listed in Table 2.4.1.

Mechanical cooling

The array can be used in a high intensity hadron beam condition by introducing mechanical cooling of a Ge detector [43]. In the experiments using high energy hadronic beams, fast neutrons, having a kinetic energy of the order of MeV, displace Ge atoms after nuclear scattering, leading to lattice defects in crystal structure. With a damaged

Table 2.4.1: Specifications of the Ge detectors.

Crystal	N-type (closed end shape)
Preamplifier	transistor-reset type
Detector gain	50 mV/MeV
Reset energy	∼120 MeV/reset
Crystal size	$\phi 70 \times 70^L$ mm^3 (250 cm^3)
Relative efficiency	60%
Window in front of the crystal	Al (t=1 mm)
Cooling method	mechanical cooling with a pulse-tube refrigerator
Crystal temperature	73 K (typical)
Thermometer	Pt100

crystal, the energy resolution of the Ge detector becomes worse due to hole trapping nature of the defects resulting in incomplete charge collection. The effect of radiation damage on a Ge detector can be restrained by keeping crystal temperature lower than 80 K [44]. Therefore, we have developed mechanically-cooled Ge detectors with a lower crystal temperature than that by liquid nitrogen cooling (∼90 K). Figure 2.22 shows a schematic view of the Ge detector unit. A pulse-tube refrigerator (PTR) which is manufactured by Fuji Electric Co. Ltd. was coupled to the Ge crystal. Water cooling of the PTR compressor increases its cooling power. We have succeeded in cooling the crystal down to ∼70 K by using a mechanical pulse-tube refrigerator of our choice, which is lower than the LN_2 cooling by 20 K and sufficient for our purpose. Because of low mechanical vibrations of PTR, the Ge sensor-cooler unit has comparable energy resolution with that of the LN_2 cooling. Furthermore, without a dewar, dense placement of Ge detectors has become possible with adjustable geometry.

Reset-type preamplifier

All of the Ge detectors were equipped with a transistor-reset type preamplifier in order to operate them in a high energy deposit rate (∼0.2 TeV/s). In the experiment using high energy beams, high energy particles in the beam halo and scattered beams off the target could pass through the Ge detectors. The energy deposit of such a charged particle in a Ge crystal is ∼70 MeV and is extremely larger than that of nuclear γ ray (0–8 MeV). The transistor-reset type preamplifier is suitable for use in such a condition, while a resistive-feedback type preamplifier can not be used because of saturation of the preamplifier output signal. The transistor-reset type preamplifier reset their output signal to the base line level when overload of the output signal is detected. The overload energy threshold was adjusted to 120 MeV by using a large capacitance feedback capacitor. With our readout electronics, a dead time of ∼30 μs followed after each reset triggered

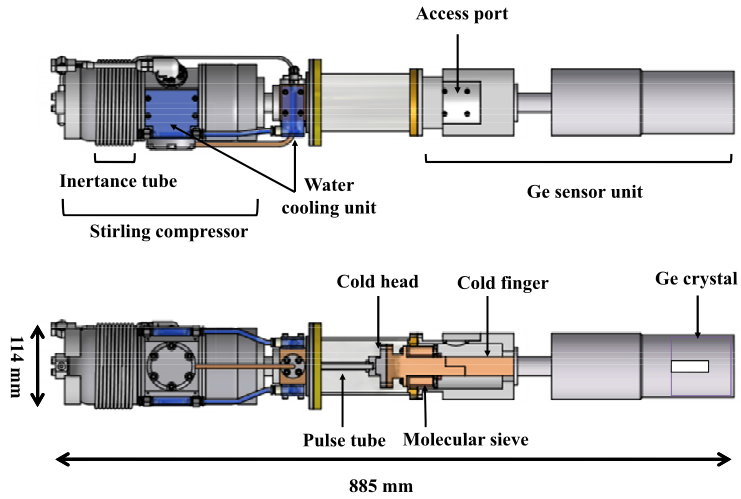

Figure 2.22: Schematic view of the mechanically-cooled Ge detector. A PTR was coupled to the Ge sensor. Water cooling of PTR increases its cooling power.

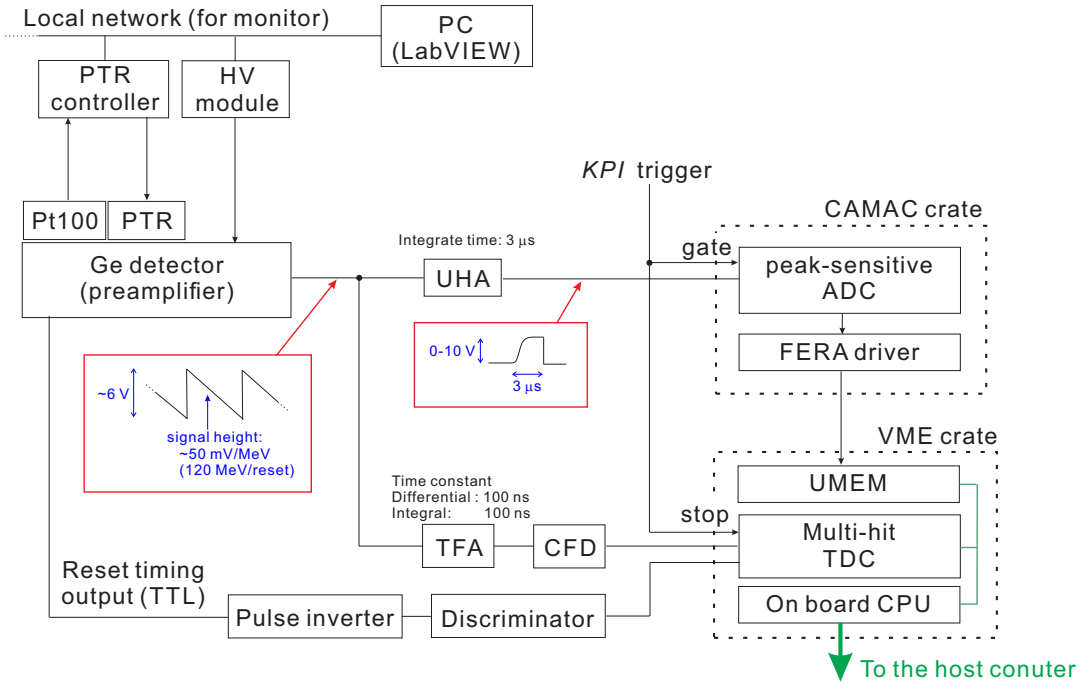

Figure 2.23: Block diagram for the Ge detector read-out and the control system.

by every 120-MeV energy deposit accumulated in a Ge crystal.

Readout electronics

The readout electronics connected to the preamplifier were also specialized in use under the high counting and energy deposit rate conditions. Figure 2.23 shows a block diagram of the readout circuit for a Ge detector. The Ultra-High-rate Amplifier (UHA, ORTEC 973U, integration time = 3 μs) was used as a main amplifier for reading out energy. In UHA, the output signal from the preamplifier was processed with $\sim$0.5 μs shaping time and then integrated with a 3-μs integration time. The dead time of the amplifier, therefore, due to signal pile up was 6 μs. The module outputs a Count-Rate-Monitor (CRM) TTL logic signal which was used for a Ge detector self-trigger. The output signal from UHA was digitized by a peak-sensitive ADC with a 13 bit resolution (ORTEC AD413A). For the timing information, the output signal from the preamplifier was processed through a fast Timing Filter Amplifier (TFA, ORTEC 579, differential/integration time = 100/100 ns), and a constant fraction discriminator (CFD, ORTEC 934). The timing information was digitized by a multi-hit TDC (Notice TDC64M).

The digitized data from the ADC modules were sent to a FERA driver module via FERA bus and then to a Universal MEMory module (UMEM). The information stored in UMEM and the multi-hit TDCs was transfered to a host computer via VME bus. See Section 2.6 for the descriptions of the data acquisition system.

Control system

We have also developed a Hyperball-J control system based on the network communication (TCP/IP protocol) and the GUI programming language, LabVIEW. This system is capable of remote control of the Hyperball-J components including the bias HV of the Ge detectors and the pulse-tube refrigerators and it constantly monitors the Ge crystal temperature. Bias shutdown function is incorporated into the control system for protecting the detector from high leakage currents with a rising crystal temperature.

2.4.2 PWO counters

All of the Ge detectors were surrounded by scintillation counters to suppress background events such as Compton scattering, high-energy γ rays from π^0 decay and high energy charged particles passing through the Ge crystal. $PbWO_4$ (PWO) crystal was used as a scintillator. Characteristics of the PWO scintillator are listed in Table 2.4.2. The PWO crystal has a large density of 8.28 g/cm^3 and a large effective atomic number, which gives efficient suppression of background γ rays. The PWO scintillator has a much shorter decay constant than conventional BGO scintillator. This is the reason why we adopted PWO; over suppression due to long decay constant of BGO scintillator is a

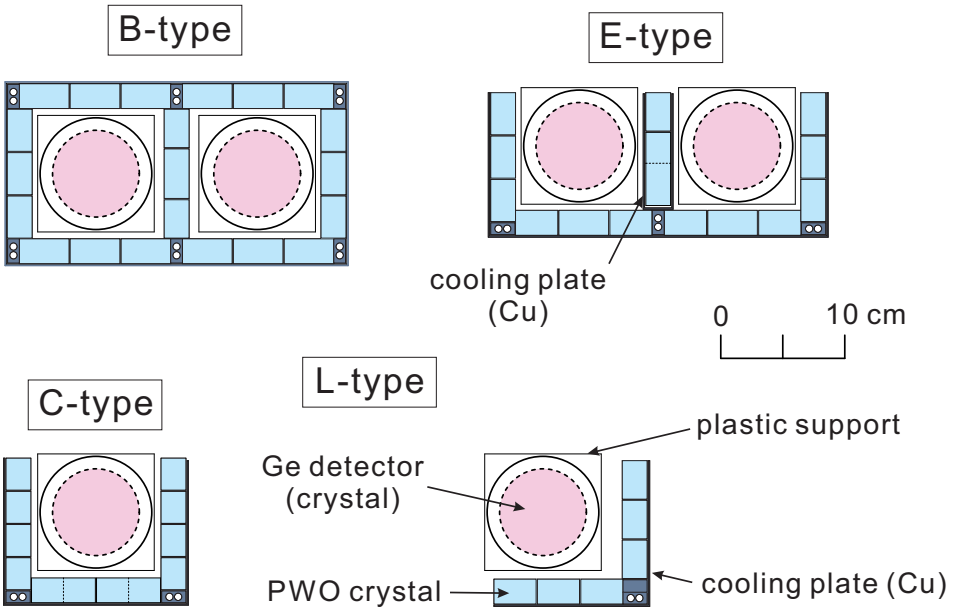

Figure 2.24: Configurations of Ge + PWO detector units.

Table 2.4.2: Characteristics of the BGO and PWO scintillator. γ reaction probabilities are for 1-MeV γ ray with 20 mm thickness.

	BGO	PWO
Composition	$Bi_4Ge_3O_{12}$	$PbWO_4$
Effective atomic number	75	76
Density [g/cm^3]	7.23	8.28
Radiation length [cm]	1.12	0.89
Decay constant [ns]	300	$\sim$6
Relative light yield [NaI=100]	15	1
γ reaction probability [%]	62	66

serious problem in high counting rate conditions. However, a light yield of PWO is much smaller than that of BGO. Therefore, we increased the light yield about four times by doping a rare-earth element and by cooling the PWO crystal to $\sim$0 C°. In order to cool down the PWO crystal, copper plates cooled by coolant were made contact to the PWO crystals. In the present experiment, typical crystal temperature was 10–13 C°, below which the PWO casing started dewing in an air-conditioned tent housing of Hyperball-J.

The configurations of the Ge + PWO detector unit are illustrated in Fig.2.24. Each Ge detector was surrounded by 12 pieces of the PWO crystals in the B-type detector units, 8 pieces in the E-type units, 9 pieces in the C-type units and 10 pieces in the L-type units.

2.4.3 LSO pulser

A Lu_2SiO_5 (LSO) scintillator was installed adjacent to each of the Ge detectors and used as a triggerable calibration source, we call it "LSO pulser". The crystal contains ^{176}Lu, with a natural abundance of 2.6%, which has a half life time of 3.76×10^{10} y and emits 202 keV and 307 keV γ rays. The LSO pulser provides a timing signal for γ-ray emissions from ^{176}Lu by detecting a β ray. Through a β-γ coincidence measurement between a LSO pulser and a Ge detector, we can discern γ rays from ^{176}Lu efficiently even in the in-beam period. Data taken both during beam spill and off the beam spill were used to monitor the performance of the Ge detectors over the beam time. These data were taken with a stand-alone data-acquisition system (see Section 2.7), independent of the HD-DAQ system described in Section 2.6.

A LSO crystal of ϕ1cm$\times0.1^L$ cm was connected to PMT, Hamamatsu H3164-10. With this crystal size, the decay rate of ^{176}Lu was of the order of 100 Bq, and a typical peak count rate of 202 keV and 307 keV γ rays in a Ge detector was $\sim$1 Hz. With the LSO pulser system, a typical in-beam live time of the Ge detectors was measured to be 96% by taking a ratio of the ^{176}Lu γ-ray yields between the on-beam-spill and the off-beam-spill periods.

2.5 KPI Trigger

To select true (K^-,π^-) reaction events from a large amount of backgrounds such as (K^-,K^-) and (π^-,π^-) events, the trigger system of SksMinus was constructed as described in the following. Figure 2.25 shows the trigger logic diagram for the (K^-,π^-) reaction. In the trigger level, beam kaons ($K_{\rm in}$) and scattered pions ($\pi_{\rm out}$) are defined as

$$\begin{aligned} K_{\rm in} &= {\rm BH2}\times\overline{\rm BAC1}\times\overline{\rm BAC2} \\ \pi_{\rm out\ upstream} &= {\rm BH2}\times{\rm SAC1} \\ \pi_{\rm out\ downstream} &= {\rm TOF}\times\overline{({\rm SFV}\times\overline{\rm SAC3})}. \end{aligned}$$

The pion contamination in the kaon beam was rejected by taking an anti-coincidence of BACs with BH2. BH1 did not join the trigger due to its extremely high single rate caused by scattered particles off the mass slit. The scattered pion was selected by taking a coincidence of SAC1 with BH2. Kaons which were miss-identified as pions by SAC1 were partly rejected by the beam-through veto counter (SFV and SAC3). Scattered pions were unaffected by the use of the SAC3 hit information.

Then, the (K^-,π^-) reaction trigger (KPI) is defined as

$$KPI = K_{\rm in}\times\pi_{\rm out\ upstream}\times\pi_{\rm out\ downstream}.$$

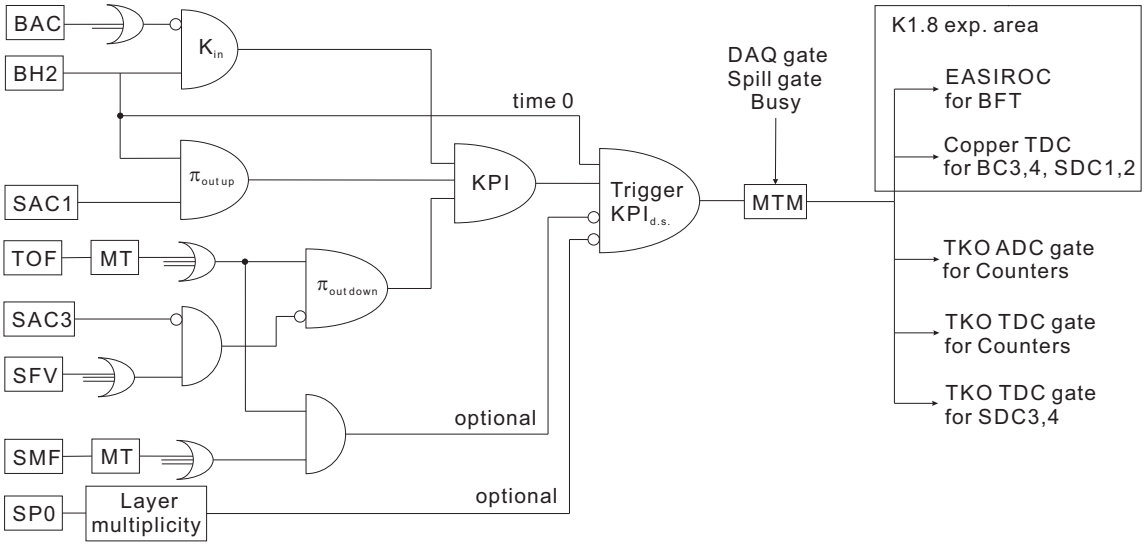

Figure 2.25: Trigger logic diagram for the (K^-, π^-) reaction.

SP0 and SMF may be included in the trigger in order to reduce the beam K^- decay events. Decay suppressed trigger $KPI_{\rm d.s.}$ is defined as

$$KPI_{\rm d.s.} = KPI \times \overline{\rm SP0_{multiplicity}} \times \overline{\rm TOF \times SMF}.$$

SP0 is not used in the trigger for ${}^{4}_{\Lambda}$He hypernuclear production because of a large branching ratio of π^0 emission decay channel (52% for ${}^{4}_{\Lambda}$He [45]), higher than the heavier hypernuclei (12% for ${}^{12}_{\Lambda}$C [46]). The remaining contamination was removed in the off-line analysis based on the time-of-flight in BH1–BH2 and BH2–TOF and the momentum measured by SKS. For monitoring of the detector performance, the BH2 prescaled trigger was made in the data acquisition trigger during the data taking period. The rates of these triggers and the prescale factors are listed in Table 2.5.1.

Table 2.5.1: The rates and prescale factors of the triggers. The beam duration time was 2.1 s for a beam spill.

Trigger	BH2	$K_{\rm in}$	$\pi_{\rm out\ upstream}$	$\pi_{\rm out\ downstream}$	KPI	$KPI_{d.s.}$
Rate [$\times 10^3$/spill]	∼490	∼340	∼140	∼280	3.7	1.6
Prescale factor	∼13000	-	-	-	-	1

2.6 Data acquisition system

A network-based data-taking system (HD-DAQ) [47] was used for the SksMinus spectrometer system. Figure 2.26 shows a block diagram of the data acquisition system. Signals of the trigger counters and SDC3, 4 are digitized with TKO TDC/ADC modules

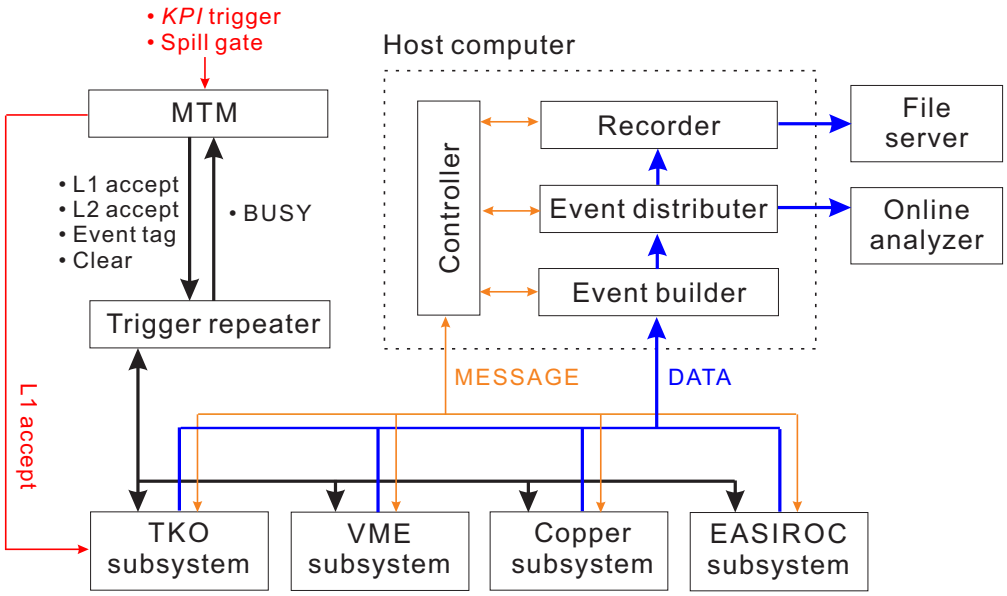

Figure 2.26: Block diagram of the data acquisition system.

and TKO TDC (Dr.TⅡ) modules, respectively. The TKO system was previously used in the KEK experiments [30]. Digitized signals are transfered to a VME memory module (VME-SMP), a VME-CPU module and a host computer in sequence. The timing information of BFT is digitized with EASIROC (Extended Analogue Silicon PM Integrated Read-Out Chip) modules [48] which were recently developed for MPPC readout. The timing information of the BC3, 4 and SDC1, 2 hits was digitized by the multi-hit TDC installed in the COPPER modules [49]. The BFT, BC3, 4 and SDC1, 2 data on the EASIROC and the COPPER modules were transfered to server computers and then to the host computer. The data-acquisition cycle was processed event by event.

The network-based data-taking system employed a DAQ software using TCP/IP protocol and a trigger/tag distribution system. For building up an event by combining data sets coming from different modules, the Master Trigger Module (MTM) distributes the event and spill numbers to a Receiver Module (RM) in each node. These numbers were transported together with digitized raw data to the host computer. MTM also manages busy signals for all the nodes. The data transfered from each module to the host computer were processed at first by the Event builder. Then they were transfered to the Event distributer and to the file server as well as to the on-line analyzer. A typical data size for one event was 2.8 kB. The data-taking efficiency was 70% for the (K^-, π^-) reaction with a trigger rate of 1.7×10^3/spill ($\sim$800 Hz).

2.7 Ge detector self-triggered data

The self-triggered data for the calibration and monitoring of the Ge detectors were taken in the beam-spill period and off the beam-spill period. Figure 2.27 shows a block diagram of the self-triggered data system.

Ge self trigger (off-beam-spill)

The Ge self-triggered data were taken off the beam-spill period (∼4 s), which were used for a correction of Ge detector gain drift. In general, Ge detector gain depends on the crystal temperature. With the mechanical cooling of Ge detectors, cooling power and thus of the crystal temperature is affected by a change in room temperature and the cryostat vacuum. The detector gain shifts according to the crystal temperature in our Ge detectors. The trigger for the off-beam-spill data was made with the CRM signals from the 973U modules. In the self-triggered data, γ-ray peaks from normal nuclei, such as a β delayed nucleus having a lifetime longer than the order of 1 s and daughter nuclei of the Th-series decay chain, were used for the calibration. A bundled thorium dioxide

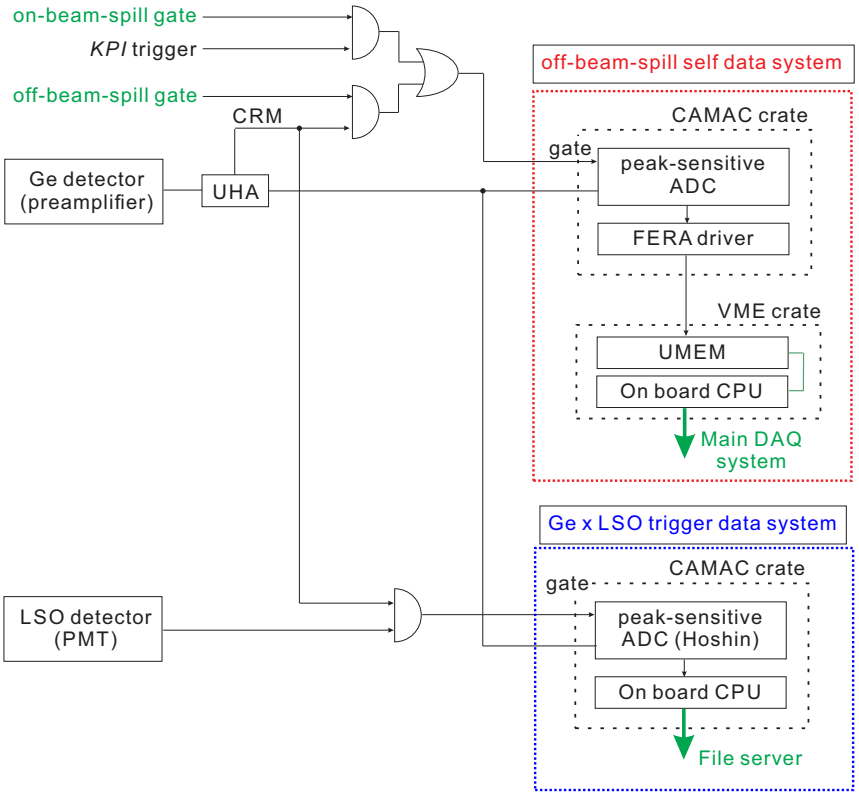

Figure 2.27: Block diagram of the self-triggered data system.

tungsten (ThO_2-W) sticks, of which size was ϕ10 mm$\times$60^L mm, was installed near the Ge detector as a reference γ-ray source, that emits 0.5–2.6 MeV γ rays. A typical weight of the ThO_2-W sticks was 40 g for a bundle, where containing ratio of ThO_2 was 2%. ThO_2-W sticks were wrapped by a 1 mm-thick lead sheet to shield low energy (<200 keV) γ rays. The single rate of the Ge detectors was increased by about 150 Hz with the ThO_2-W sticks placed near the Ge detectors.

Ge×LSO trigger (on- and off-beam-spill)

The Ge×LSO trigger data were taken in both on-beam-spill and off-beam-spill periods, which were used to monitor the live time of the Ge detectors by comparing peak counts of 202 keV and 307 keV γ rays between the on-beam-spill and off-beam-spill period after considering the efficiency of the data acquisition system. The trigger was made from a Ge CRM signal coincident with a corresponding LSO signal. The energy information of the Ge detectors was digitized by a peak-sensitive ADC module (HOSHIN), and the time difference between a Ge detector and a LSO detector was digitized by a TDC module. These data were transported to the file server by the on-board CPU module.

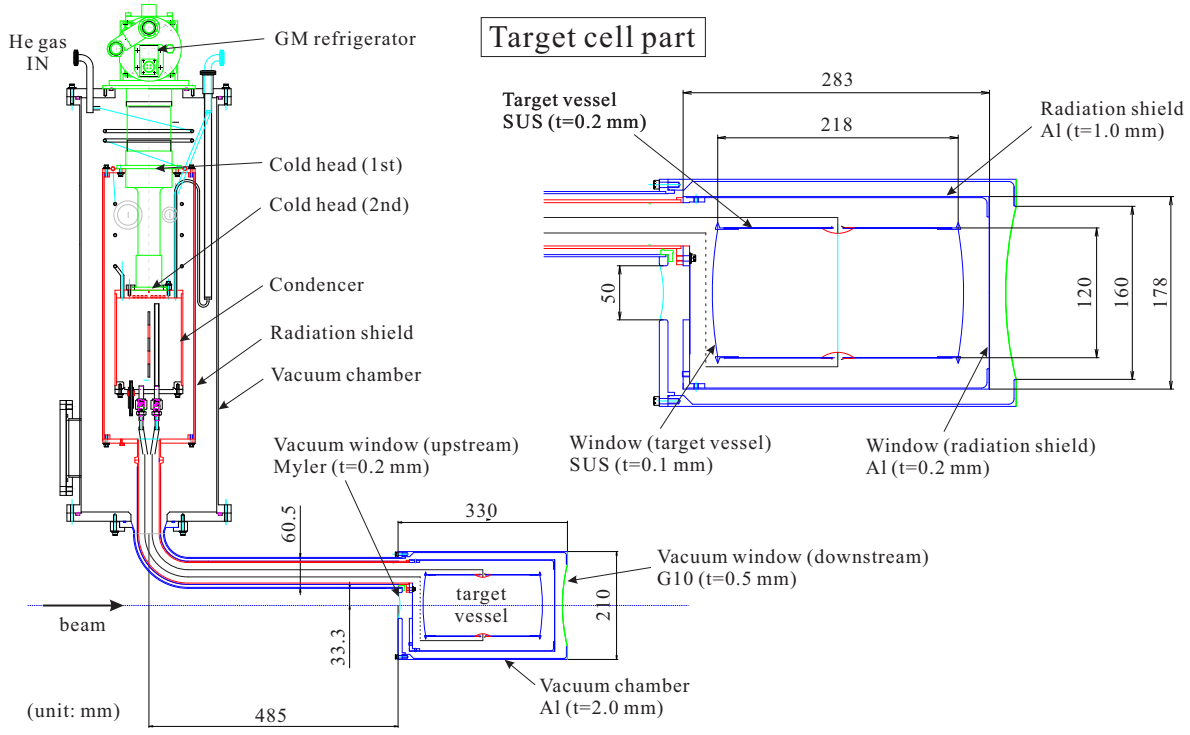

Figure 2.28: Schematic view of the liquid ^{4}He target system.

Table 2.7.1: Specifications of the liquid ^{4}He target system.

Size	$\phi 120 \times 218^L$ mm^3
Capacity	2466 cm^3
Target cell	stainless steel(t=0.2 mm ,cylinder) and (t=0.1, end cup)
Radiation shield	Al(t=0.2 mm, cylinder), Al(t=0.2 mm, end cup)
Vacuum chamber window	Mylar(t=0.3 mm, upstream),
	G10(t=0.5 mm, downstream)
Vacuum	$\sim 8 \times 10^{-6}$ Pa
Helium temperature	4.4 K
Helium gas pressure	0.103 MPa
Liq. helium density	0.125 g/cm^3
liq. ^{4}He thickness	2.8 g/cm^2

2.8 Target

In order to obtain a large yield of hypernuclear production events, a long liquid ^{4}He target was used. We decided the target thickness to be of $\sim$3 g/cm^2, corresponding to the length of 230 mm, to keep the missing mass resolution of $\sim$5 MeV (FWHM). Furthermore, a longer length of the target causes a loss of effective solid angle of Hyperball-J and an increase of contamination from beam K^- decay with a longer distance between BACs and SAC1.

Figure 2.28 shows a schematic view of the liquid ^{4}He target system. The target vessel was made of stainless steel (SUS) with a thickness of t=0.2 mm for cylindrical part and t=0.1 mm for an entrance and exit windows. We selected stainless steel as a material so that its large size vessel has enough mechanical strength in the low temperature condition. The diameter of the vessel was ϕ120 mm in order to cover a horizontally-wide beam K^- profile. The length of the vessel was 218 mm. In the operation condition, the target length became slightly ($\sim$ 10 mm) longer due to inflation of the SUS window in the vacuum chamber. The density of liquid helium was monitored by measuring its temperature and the gas pressure. The stability of the liquid Helium density was $\Delta\rho/\rho < 10^{-5}$ over the experimental period. Specifications of the liquid ^{4}He target system are listed in Table 2.7.1.

2.9 Data summary

The total beam time we used for the data taking with the ^{4}He target was about 130 hours. In total, 2.3×10^{10} kaons were irradiated on the ^{4}He target. We also took reference data with an empty target vessel and without the target vessel. In the empty target vessel run, we took data with the KPI trigger to check the contamination from material

other than helium. With a polyethylene (CH_2, 2.9 g/cm^2) target, we took data of the $p(K^-, \pi^-)\Sigma^+$ and ^{12}C$(K^-, \pi^-)^{12}_{\Lambda}$C reactions for validating the missing mass analysis. With a thin plate (t=3 mm) of stainless steel target, we took data of beam particle scattering events for estimation of the reaction vertex resolution. Without any material at the target position, beam particles were let through both the beam line spectrometer and SksMinus for calibration of these magnetic spectrometers. This beam-through data was taken with the BH2 trigger. The data acquired in the experiment are summarized in Table 2.9.1.

Table 2.9.1: The data summary.

Target	Beam momentum [GeV/c]	Number of K^-
Liquid ^{4}He	1.5	2.3×10^{10}
Emptied target vessel	1.5	6.0×10^8
Polyethylene (CH_2)	1.5	1.0×10^9
Stainless steel (t=3 mm)	1.5	8.7×10^7
No target installed (beam-through)	1.8, 1.5, 1.37, 1.2	-

Chapter 3

Analysis I - the (K^-, π^-) reaction

The analysis procedure is separated into two parts: the analysis of the magnetic spectrometers and the analysis of the Ge detectors. In the former, the hypernuclear production events were tagged by the spectrometer system. In the latter, γ-ray spectrum was obtained with Hyperball-J. The analysis of the magnetic spectrometers, the beam line spectrometer and SksMinus, is described in this chapter. The analysis of the Ge detector is described in the next chapter.

3.1 Outline

The hypernuclear production events were identified by tagging true (K^-, π^-) reaction events from particle identification and calculating mass of a produced hypernucleus ($M_{\rm HY}$) as a missing mass for the ^{4}He$(K^-, \pi^-)X$ kinematics. The mass is calculated by the following equation in the laboratory frame

$$M_{\rm HY} = \sqrt{(E_K + M_{\rm target} - E_\pi)^2 - (p_K^2 + p_\pi^2 - 2p_K p_\pi \cos\theta_{K\pi})},$$

where E_K and p_K are the energy and the momentum of the beam K^-. Similarly, E_π and p_π are those of the scattered π^-. $M_{\rm target}$ is the mass of the target nucleus (^{4}He), and $\theta_{K\pi}$ is the angle between the measured momentum vector of the K^- and that of the π^-. True ^{4}He(K^-, π^-) events were also selected with the reaction vertex point information.

The off-line analysis procedure of the (K^-, π^-) reaction for data from the magnetic spectrometers is listed below:

- particle identification with the time-of-flight counters,
- local tracking of the drift chambers,
- momentum reconstruction for beam K^-,
- momentum reconstruction of scattered π^-,

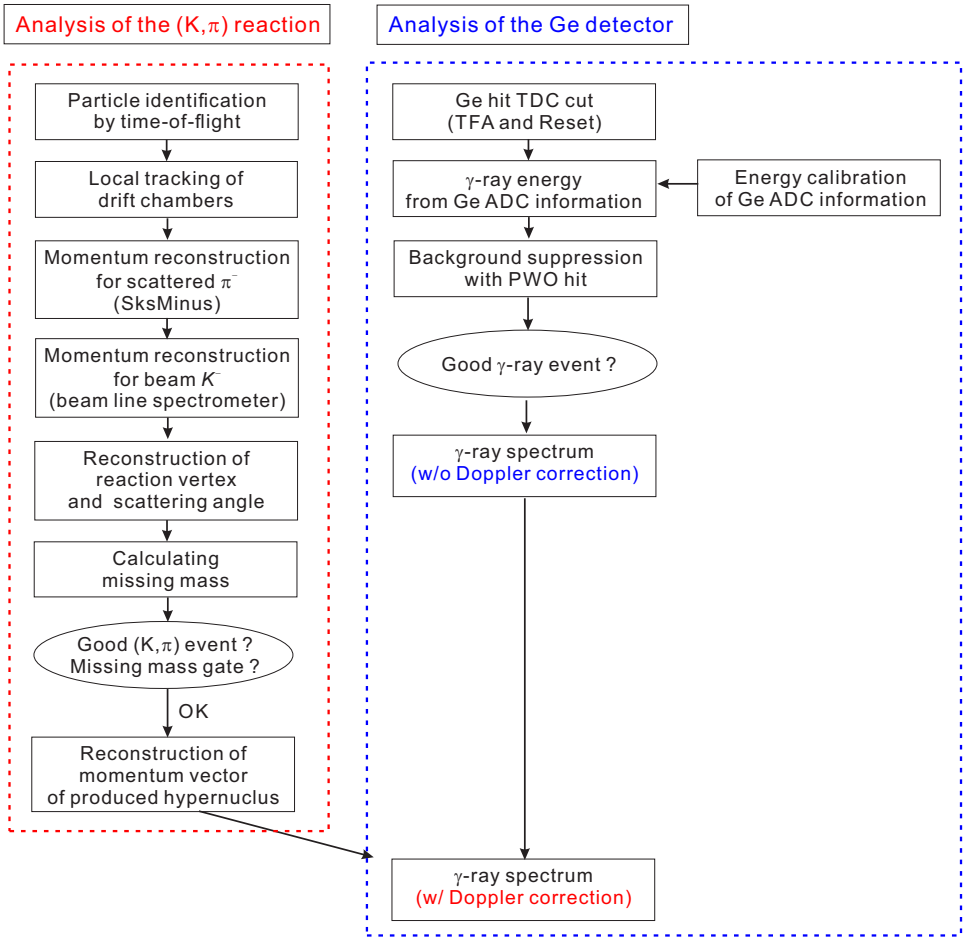

Figure 3.1: The analysis procedure for the obtained data.

- reaction vertex and scattering angle ($\theta_{K\pi}$) reconstruction,
- calculation of missing mass,
- calculation of velocity of a produced hypernucleus and reconstruction of its momentum vector.

The analysis procedure is illustrated in Fig. 3.1.

3.2 Analysis of incident particle

3.2.1 Momentum reconstruction for beam particle

The momentum of the beam particle was reconstructed from the data of the fiber scintillation counter (BFT, installed at the upstream of QQDQQ magnets) and the drift

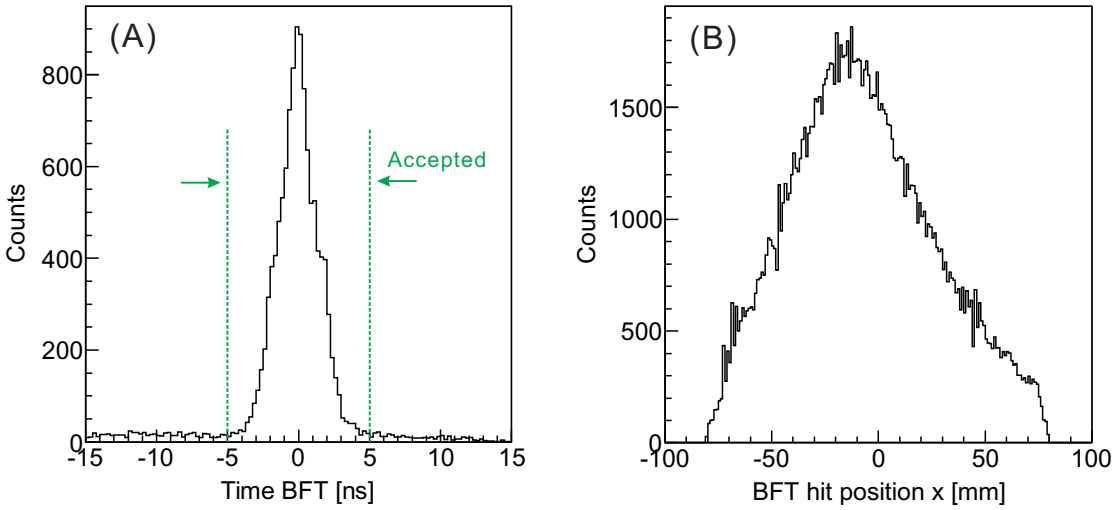

Figure 3.2: (A) Time distribution of BFT (BH2−BFT) and (B) hit profile of BFT for beam K^- mesons.

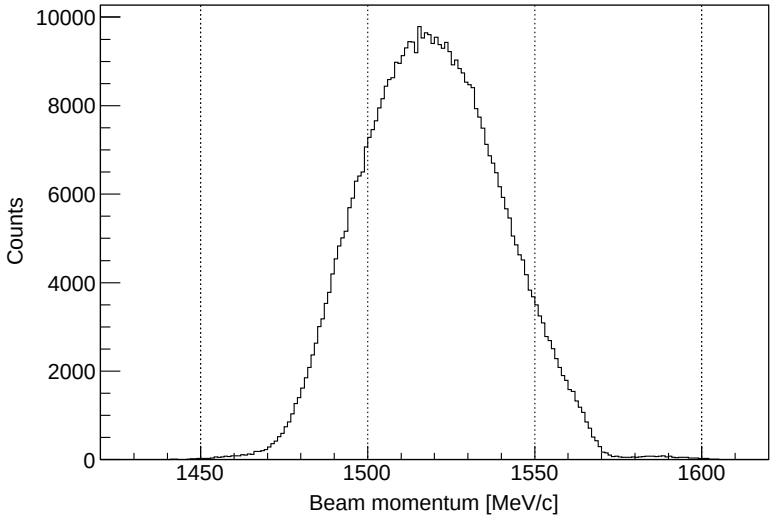

Figure 3.3: Momentum distribution of beam K^- measured by the beam spectrometer. The beam momentum was set at 1.5 GeV/c.

chambers (BC3,4, installed at the downstream of the magnets), using the third-order transport matrix for the beam line spectrometer.

A clustering analysis of BFT provides a horizontal position of beam kaon trajectory at the upstream of QQDQQ magnets. Figure 3.2 shows a time distribution and a hit profile of BFT for beam K^- mesons. Events with a single cluster hit within a time gate of ±5 ns was accepted. BFT made the time gate much shorter that that for previously

used MWPCs (∼100 ns) [31]. The yield loss after the BFT analysis was ∼7%, which came from a shortage of the effective area and the multiplicity cut. A local straight track was reconstructed from measured positions in BC3 and BC4 by the least χ^2 fitting method, where number of degree of freedom (NDF) is 8 (=12 [number of layers of the sense wire plane] −4 [parameters]). In the local tracking, tracks with minimum χ^2 values of more than 20 were rejected as a fake track. Events with a single track was accepted. The yield loss due to the BC3,4 tracking was ∼2%. The track information obtained with the local tracking of BC3,4 was used as an incident vector of K^- for calculation of a scattering angle $\theta_{K\pi}$.

A momentum of the beam particle was uniquely calculated with the transport matrix using a horizontal position (x) at the upstream of QQDQQ magnets as well as positions (x,y) and a direction (u=Δx/Δz,v=Δy/Δz) at the downstream of the magnets. Figure 3.3 shows the reconstructed momentum distribution of the beam K^-.

3.2.2 Selection of K^-

Beam K^- particles were efficiently selected by aerogel Čerenkov counters (BAC1,2) at the trigger level. Figure 3.4 shows a time-of-flight distribution between BH1 and BH2 for KPI triggered events, where the horizontal axis is a time difference from the pion time-of-flight. A small amount of pions can still be seen in the spectrum. These contaminations

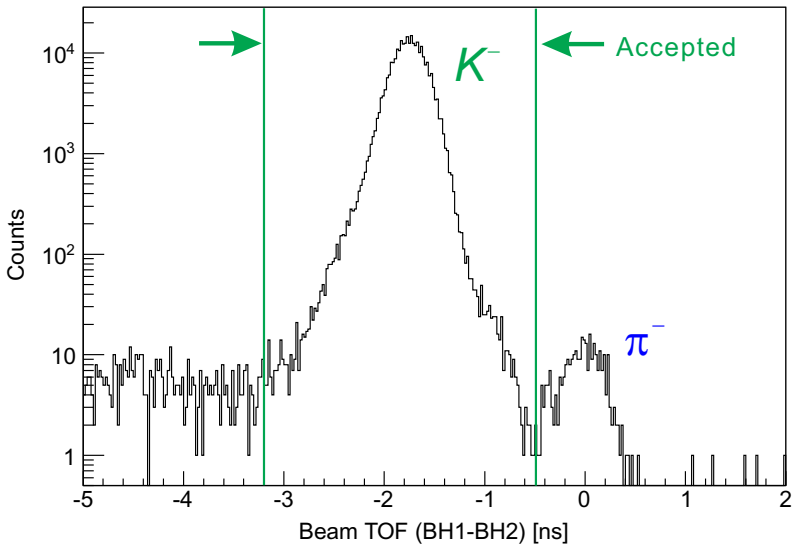

Figure 3.4: Time-of-flight distribution between BH1 and BH2 for KPI triggered events. The region of −3.2 ns < beam TOF (BH1–BH2) < −0.5 ns was selected as the time gate for the beam K^-.

were removed by selecting time-of-flight for kaons. The region of -3.2 ns $<$ beam TOF (BH1-BH2) < -0.5 ns was selected as the time gate for the beam K^- with a negligibly small loss of the beam K^- events. The time-of-flight (BH1–BH2) resolution was 155 ps in rms, and the K/π resolving power ($= \Delta t_{\pi\leftrightarrow K}/(\sigma_\pi + \sigma_K)$) was 5.4σ.

3.3 Analysis of scattered particle

3.3.1 Momentum reconstruction for scattered particle

The momentum vector of the scattered particle was reconstructed from the data of the drift chambers, SDC1,2 installed at the upstream of SKS magnet and SDC3,4 installed at the downstream of the magnet. A local straight track was drawn from measured positions in SDC1,2 for entering tracks into SKS and in SDC3,4 for outgoing tracks, by the least χ^2 fitting method. In the local tracking, tracks with minimum χ^2 values of more than 20 were rejected as fake tracks.

The Runge-Kutta method [33] was used for reconstruction of SKS trajectories using a magnetic field map. The magnetic field map was calculated by the TOSCA code [34] with the finite element method. The trajectory and the momentum of the scattered particle were obtained by the least χ^2 fitting method. The χ^2 value of SKS trajectory is defined as

$$\chi^2_{SKS} = \frac{1}{n-5}\sum_{i=1}^{n}\left[\frac{x_i^{\rm tracking} - x_i^{\rm data}}{\sigma_i}\right]^2,$$

where n is the number of layers having hits (the maximum number of layers is 22), $x_i^{\rm tracking}$ is the reconstructed hit position on the i-th layer on the SKS trajectory, and $x_i^{\rm data}$ and σ_i denote the measured hit position and the position resolution of the i-th layer, respectively. Typical position resolutions of a sense plane in these drift chambers are listed in Table 2.3.3. In the present analysis, events in which χ^2 in the SKS tracking was less than 20 were selected. Figure 3.5 shows a χ^2 distribution in the SKS tracking, and Fig. 3.6 shows the reconstructed momentum distribution for scattered pions selected by the time-of-flight method as described in the next section. Even after suppression of beam K^- decay events was applied using the SMF hit information (see Section 2.3.3), a small contamination from $K^- \to \mu^- + \bar{\nu_\mu}$ and a large contamination from $K^- \to \pi^- + \pi^0$ are expected to remain in this spectrum. Thanks to the wide momentum acceptance of SksMinus, Σ hyperon production events were also included in the data.

If more than one track was found in the local tracking, all possible combinations of those local tracks were tried in the SKS tracking. If reconstructed tracks do not pass through the hit segment of TOF, they were rejected as fake tracks in this analysis. Events in which more than one track remained were rejected. The yield loss by rejecting

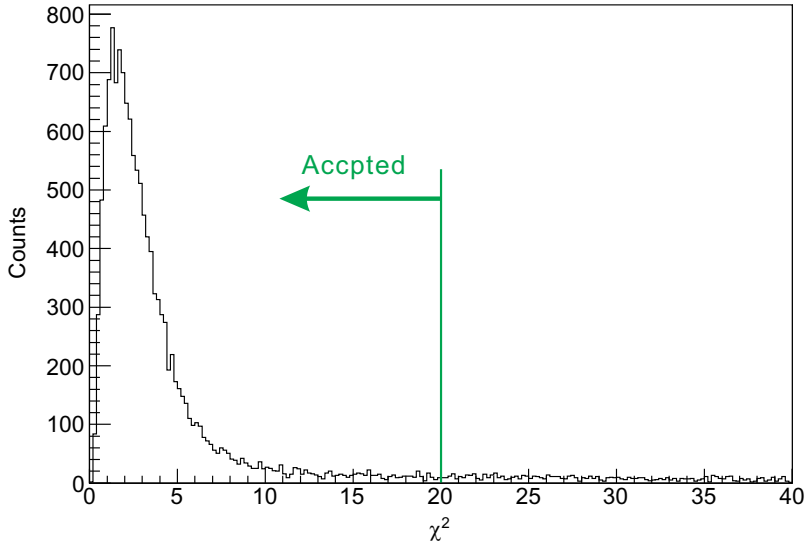

Figure 3.5: χ^2 distribution in the SKS tracking for scattered π^-.

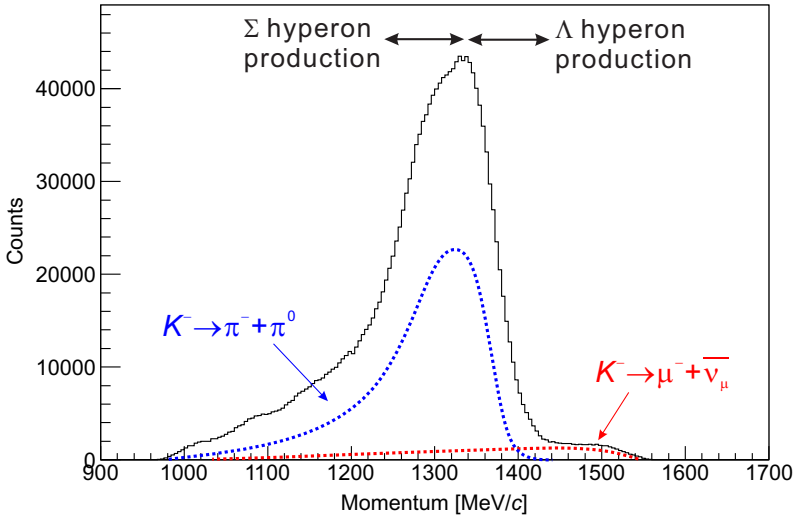

Figure 3.6: Momentum distribution reconstructed in the SKS tracking for scattered π^-. Contribution of beam K^- decay was estimated from data obtained with similar setup and no target material. See Section 3.9 for a description of the beam K^- decay analysis.

multi-track events was ∼3%. The track information reconstructed by the SKS tracking was used for an outgoing vector of π^- in calculation of a scattering angle $\theta_{K\pi}$.

3.3.2 Selection of π^-

In the KPI trigger, a large amount of background events were accepted due to a miss-identified kaon as a pion by SAC1. To reject these events, a time-of-flight (BH2–TOF)

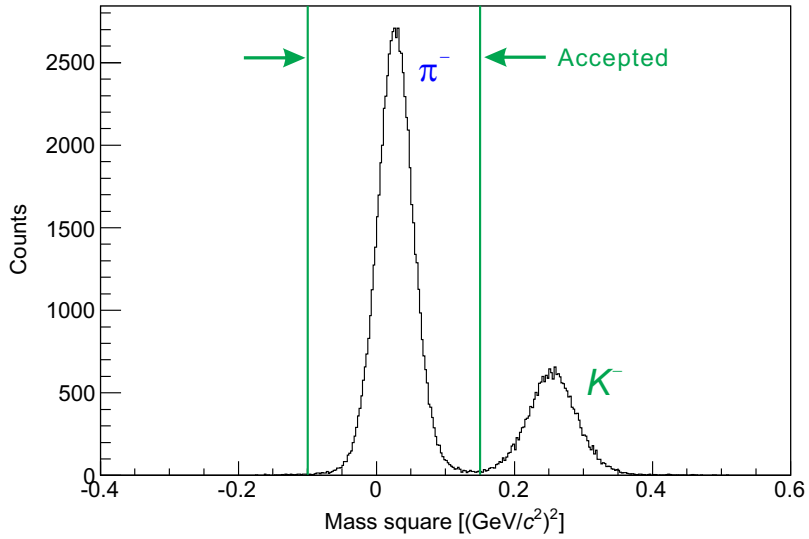

Figure 3.7: Mass spectrum for scattered particles for the KPI triggered events. The mass is plotted in the scale of mass square.

cut was applied in the off-line analysis. By using the time-of-flight information and a result of the SKS tracking, the mass of the scattered particle ($M_{\rm scat}$) can be calculated as

$$M_{\rm scat} = \frac{p}{\beta}\sqrt{1-\beta^2}, \quad \beta = \frac{L}{c\Delta t},$$

where p is the momentum of the scattered particle reconstructed by the SKS tracking, and β is a velocity of the scattered particle. β was calculated from a path length of a trajectory (L) between the target and TOF (typically of 5 m) obtained by the SKS tracking analysis and a time-of-flight (Δt) between BH2 and TOF correcting for a distance between BH2 and the target. Figure 3.7 shows a mass square spectrum for scattered particles in the unit of $(\mathrm{GeV}/c^2)^2$ for the KPI triggered events. Contamination from "beam K^- scattering" events is seen in the spectrum. The region of -0.10 $(\mathrm{GeV}/c^2)^2 < M^2_{\rm scat} < 0.15$ $(\mathrm{GeV}/c^2)^2$ was selected for the scattered π^-. The K/π resolving power ($= \Delta t_{\pi\leftrightarrow K}/(\sigma_\pi + \sigma_K)$) was 3.6σ where a dominant inaccuracy came from the time-of-flight (BH2–TOF) resolution of 135 ps in rms.

3.4 Reconstruction of scattering angle and reaction vertex

The scattering angle ($\theta_{K\pi}$) and the reaction vertex point were determined from vectors of an incident particle and an outgoing particle at the target region. The track obtained by the local tracking of BC3,4 was used as an incident particle vector, while the track

from the SKS tracking was used as an outgoing particle vector instead of the straight track from the local tracking of SDC1,2, because of an effect of the magnetic fringing field of the SKS magnet at the SDC1,2 position.

The scattering angle ($\theta_{K\pi}$) was defined as the angle between the vectors of the incident particle and the outgoing particle in the laboratory frame. The resolution of $\theta_{K\pi}$ was checked using beam-through data by letting beam pions having a momentum of 1.5 GeV/c pass through both the beam line spectrometer and SksMinus with a liquid helium target. The resolution was better than 0.5 deg. (FWHM).

The reaction vertex point was determined by taking a spatially closest point between the vectors of the incident particle and of the outgoing particle. Figure 3.8 (A) shows projections of the reaction vertex position onto the z-axis (z-vertex distribution) for the beam K^- scattering events, where the z axis is defined as the beam direction and z=0 is defined as the center of Hyperball-J. In this figure, a black line shows the vertex

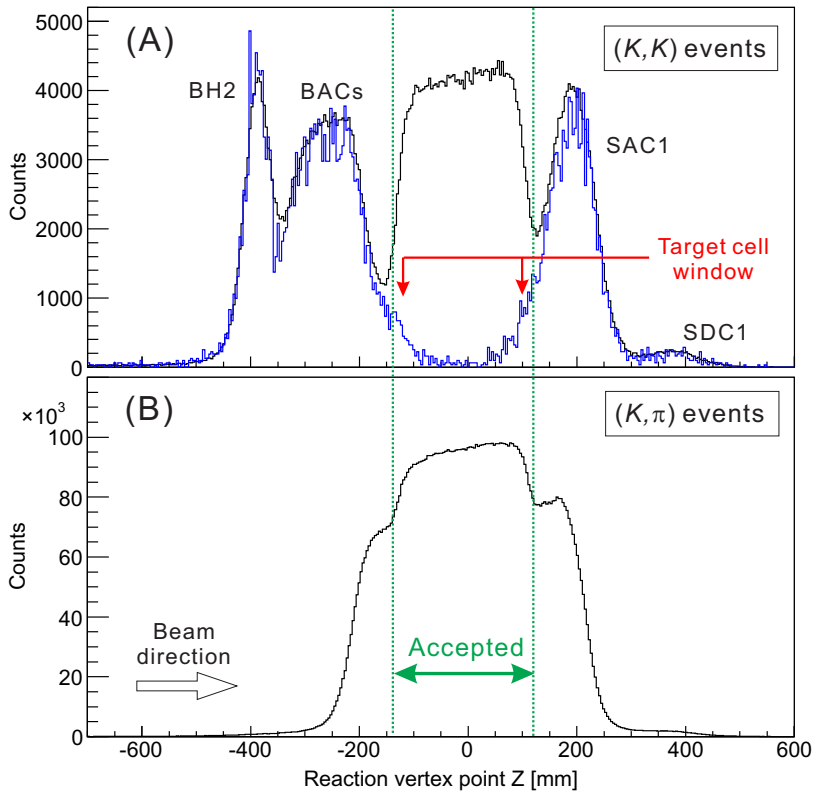

Figure 3.8: Z-axis projection of the reaction vertex position, where z axis is defined as the beam direction: (A) the distribution for the beam K^- scattering events, (B) the distribution for the KPI triggered events. In the spectrum (A), black line and blue line show the vertex distribution with the liquid helium target and with the empty target vessel, respectively.

point distribution with the liquid helium target, and the blue line with the empty target vessel. Background events in which the beam particle was scattered in the material of the detectors around the target (BH2, BACs, SAC1, SDC1) are shown in blue. On the other hand, an enhancement near the center was found with the liquid helium., which indeed indicates the presence of liquid helium in the target vessel. Figure 3.8 (B) shows a z-vertex distribution for the (K^-, π^-) events for the KPI triggered events. In this distribution, a large amount of beam K^- decay events that occurred between BACs and SAC1 ($\sim$45 cm in distance) overlapped with true (K^-, π^-) reaction events. Because of this background in the KPI triggered events, accepted gate for the z-vertex position was decided using the beam K^- scattered events. The z-vertex resolution depends on $\theta_{K\pi}$ and was 22 mm (σ) at $\theta_{K\pi}$= 5°, which was measured with a thin stainless steel target described in Section 3.5.

Figure 3.9 shows a contour plot of z-vertex points versus $\theta_{K\pi}$ for the beam K^- scattered events with liquid helium. Events in which $\theta_{K\pi}$ was less than 3.5° were rejected in the present analysis because of a worse z-vertex resolution and also of a large amount of contamination from beam $K^- \to \pi^- + \pi^0$ decay events which kinematically overlap with the hypernuclear production events (see Section 2.3.3). To reject a background events from material other than liquid helium, a z-vertex cut was applied in the present analysis. A region of -140 mm < z-vertex point < 120 mm was selected in the analysis.

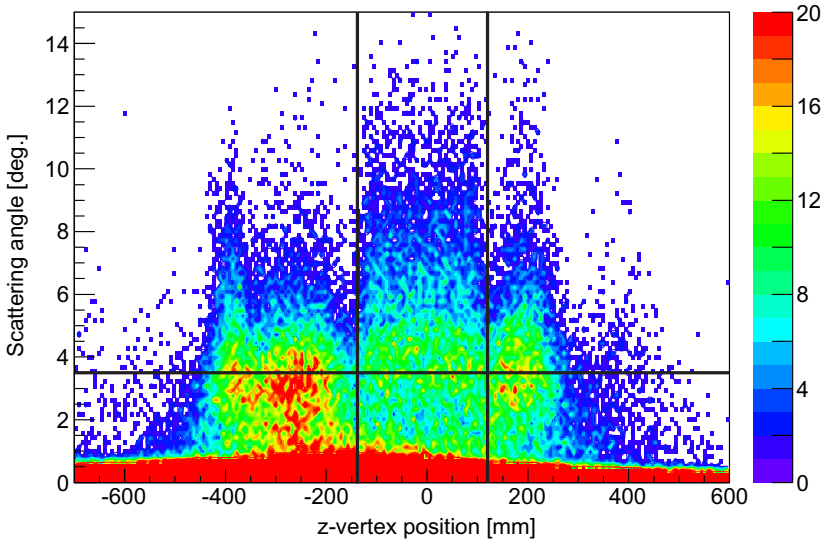

Figure 3.9: Contour plot of z-vertex points versus $\theta_{K\pi}$ for the beam K^- scattering events with liquid helium. Region of -140 mm < z-vertex point < 120 mm was selected as the reaction events on helium. Events in which $\theta_{K\pi}$ was less than 3.5° were rejected because of a worse z-vertex resolution and also a large amount of contamination from beam $K^- \to \pi^- + \pi^0$ decay events.

The yield loss due to this tight z-vertex cut was estimated to be ∼4% in total by a simulation using an angle dependence of the ^{4}He(1^+) production cross section based on a DWIA calculation [26].

3.5 Calculation of missing mass

The missing mass is calculated using measured momenta of the beam K^- meson and of the scattered π^- meson and the scattering angle ($\theta_{K\pi}$) as described in Section 3.1. In the present analysis, we applied corrections for measured momenta of the kaon (p_K) and the pion (p_π), namely, (1) the horizontal and vertical angle dependence for p_K, (2) the energy loss in the target for p_K and p_π.

Horizontal and vertical angle dependence for p_π

In the SKS magnet system, a measured p_π has a systematic shift which depends on the trajectory through the SKS magnet due to an ambiguity in the calculated magnetic field map. In the present analysis, the measured p_π was corrected with a 2nd-order polynomial function of horizontal angle ($u = dx/dz$) and vertical angle ($v = dy/dz$) of the scattered π^- vector at the target position. This correction was usually applied for the SKS analysis in the previous experiments [31, 39, 40, 41]. Figure 3.10 (A) shows contour plots of the calculated missing mass for the ^{4}He$(K^-, \pi^-)X$ kinematics versus the horizontal angle (u) of scattered π^-, and (B) shows that for the vertical angle (v). The missing mass is plotted in excitation energy ($E_{\rm ex}$). A major peak for the $^4_\Lambda$He(0^+ or 1^+) production is seen around $E_{\rm ex}$=0 in these plots. We determined optimum parameters of the 2nd-order polynomial functions for the correction by comparing measured $p_\pi^{\rm measured}$ and calculated $p_\pi^{\rm calcurated}$ with the ^{4}He$(K^-, \pi^-)^4_\Lambda$He kinematics. Figure 3.10 (C) and (D) show the plots after the u and v corrections, respectively.

Energy loss in the target for p_K and p_π

The momentum of the beam K^- at the reaction point was reduced from the p_K measured by the beam line spectrometer due to energy loss effects in the trigger counters (BH2, BAC1,2) and some materials of the target system (thin windows and liquid helium). The momentum of the scattered π^- just after the reaction should be larger than the p_π measured by SKS due to energy loss in some parts of the target system and SAC1. These energy loss effects were estimated by a simulation using the Geant4 code [32]. The energy losses were estimated to be 7.3 MeV in total for the beam K^- having a momentum of 1.5 GeV/c and 4.0 MeV for the scattered π^- with p_π=1.4 GeV/c, when the reaction point is at the center of the target. Difference in the momenta p_K (and also

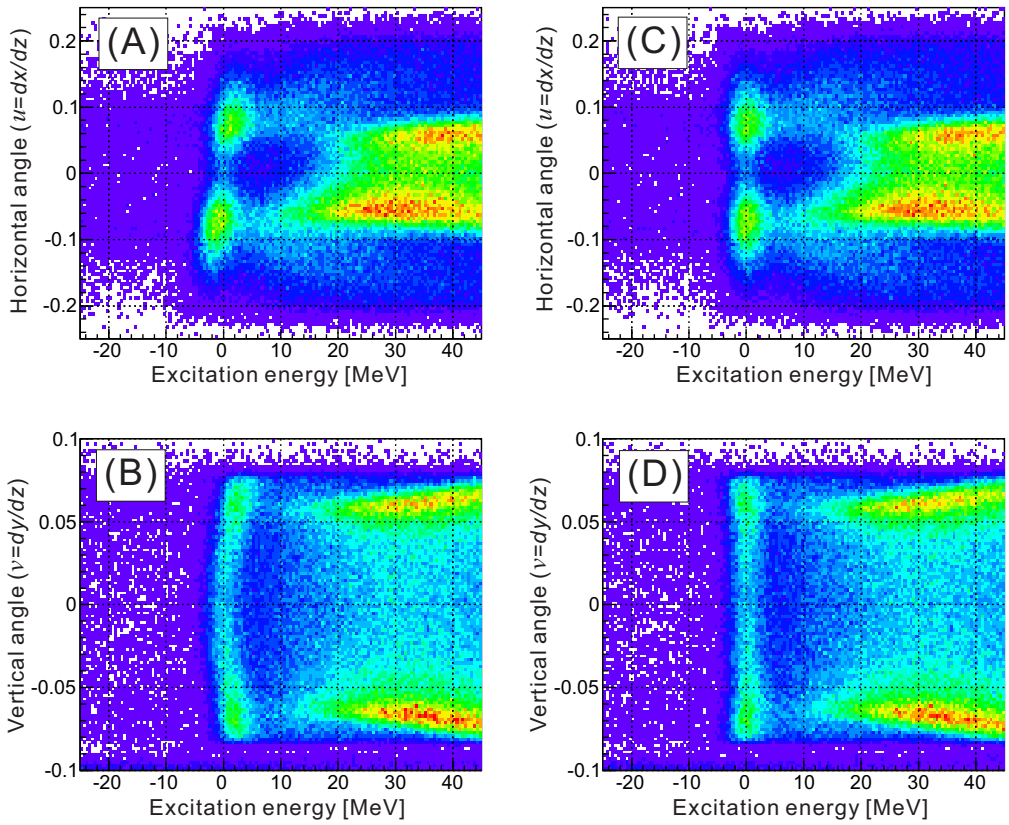

Figure 3.10: (A): Contour plots of calculated missing mass for the ^{4}He$(K^-,\pi^-)X$ kinematics versus the horizontal angle (u) of scattered π^-, (B): that for the vertical angle (v). (C) and (D): these plots after the u and v correction, respectively. A major peak for the $^4_{\Lambda}$He(0^+ or 1^+) production is seen around $E_{\rm ex}$=0.

p_π) was not considered because a change in the energy loss is less than 0.1 MeV against 0.1 GeV/c momentum change. The energy loss in the liquid helium with a total length of ∼230 mm was estimated to be ∼5 MeV, but the dependence of the calculated missing mass on the reaction point along the z-axis is estimated to be much smaller (∼0.2 MeV) than the energy resolution of our spectrometer system (∼5 MeV). Therefore, energy loss difference along z-vertex points was not taken into account in this analysis.

3.6 Mass spectrum of Σ^+ and $^{12}_{\Lambda}$C

For validating our missing mass analysis as well as our detector system, we took data with a polyethylene (CH_2) target with a thickness of t=2.9 g/cm^2 that is almost the same as the liquid helium target [2.8 g/cm^2]. With the corrected momentum of the beam kaon ($p_K^{\rm corrected}$), that of the scattered pion ($p_\pi^{\rm corrected}$) and the scattering angle ($\theta_{K\pi}$), the missing mass is calculated for the $p(K^-,\pi^-)\Sigma^+$ and ^{12}C$(K^-,\pi^-)^{12}_{\Lambda}$C kinematics.

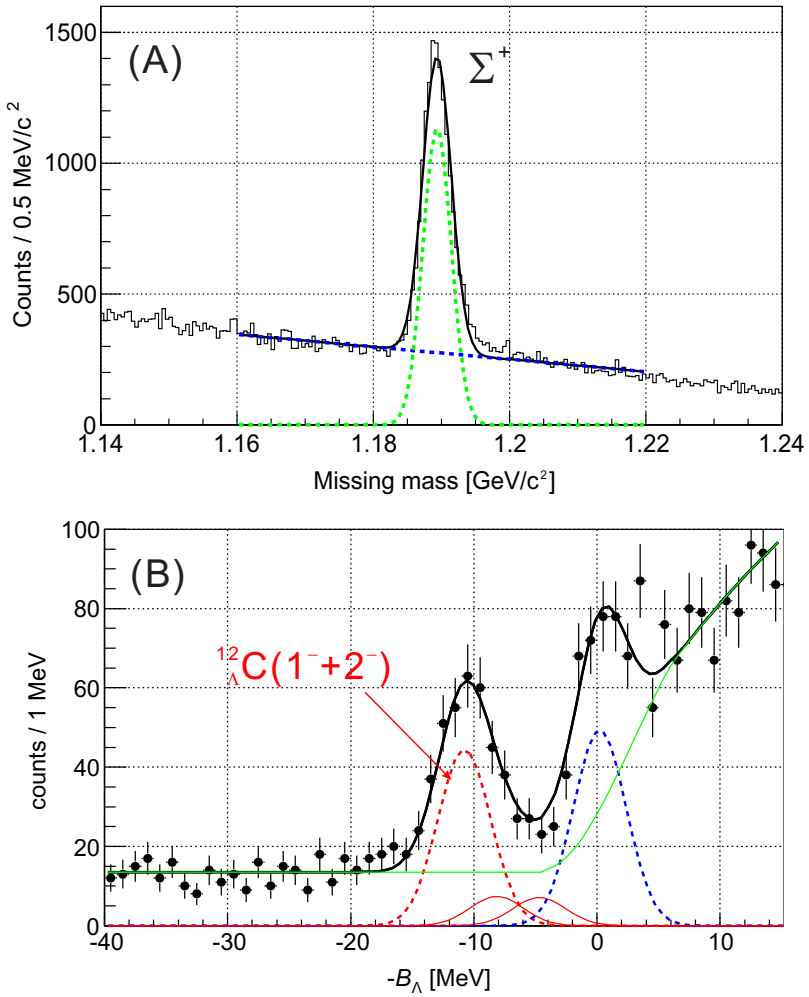

Figure 3.11: Missing mass spectra with a CH_2 target (t=2.9 g/cm^2): (A) shows the spectrum for $p(K^-, \pi^-)X$ kinematics. Peak structures in these spectra correspond to elementary Σ^+ production events. (B) shows the spectra for the ^{12}C$(K^-, \pi^-)^{12}_{\Lambda}$C reaction, in which data points are plotted against the Λ-binding energy $(-B_\Lambda)$. Scattering angles of 4–15° were selected to avoid contamination of beam K^- decay events. Energy positions and relative cross sections $(\sigma_{\rm coreexcited}/\sigma_{g.s.})$ of $^{12}_{\Lambda}$C core exited states are taken from the past experiment [50] in the fitting. K^- decay events were suppressed using SMF.

Figure 3.11 (A) shows a missing mass spectrum for the $p(K^-, \pi^-)X$ reaction. Σ^+ producing events were clearly observed on top of the beam K^- decay background and hyperon production with a $^{12}_{\Lambda}$C nucleus. An energy resolution of 4.9(1) MeV (FWHM) is achieved.

Figure 3.11 (B) shows a missing mass spectrum for the ^{12}C$(K^-, \pi^-)X$ kinematics in which data points are plotted against the Λ-binding energy (-B_Λ) scale. Decay events were suppressed by using SMF and by selecting $\theta_{K\pi}$ >4° in this spectrum. Two peak

structures can be seen. Each peak corresponds to the s- and p-Λ states of ${}^{12}_{\Lambda}$C, respectively. In the fitting, relative energy positions and cross sections ($\sigma_{\text{core excited}}/\sigma_{g.s.}$) of ${}^{12}_{\Lambda}$C core exited states are taken from the past experiment using the (π^+, K^+) reaction [50]. The background function is defined as $a\sqrt{E_{>threshold}} + b$. First, $\sqrt{E_{>threshold}}$ function for the energy distribution of the quasi-free Λ production is assumed where $E_{>threshold}$ denotes an excess energy from B_Λ=0. Secondly, constant b for the distribution of the beam K^- decay contamination is taken, of which shape was confirmed from data with the empty target to be almost flat in the shown mass range. The missing mass resolution, assumed as 5 MeV (FWHM), was convoluted into the background distribution as Gaussian. From the fit result, a missing mass resolution of 4.8(3) MeV (FWHM) is obtained combined with the beam line spectrometer.

The accuracy of absolute mass (energy) scale was estimated to be $\sim$1 MeV from the difference between the obtained peak position and the known mass of ${}^{12}_{\Lambda}$C [11]. From these results, we validated our analysis procedures for obtaining the missing mass.

3.7 Mass spectrum of ${}^{4}_{\Lambda}$He

Figure 3.12 shows the missing mass spectrum plotted as a function of the excitation energy, E_{ex}, where the missing mass was calculated for the ${}^{4}\text{He}(K^-, \pi^-){}^{4}_{\Lambda}\text{He}$ kinematics. Events with scattering angles ($\theta_{K\pi}$) larger than 3.5° are selected to reduce the background due to beam $K^- \to \pi^- + \pi^0$ decay events. The background spectrum associated with materials other than liquid helium as well as with K^- beam decay events was obtained with the empty target vessel as shown together in Fig. 3.12 (A); it is evident that the observed peak originates from the ${}^{4}\text{He}(K^-, \pi^-)$ reaction. In the spectrum with the empty target vessel, dominant events in the region of E_{ex} >10 MeV came from the beam $K^- \to \pi^- + \pi^0$ decay events. A small amount of constant background covering the entire region of the spectrum corresponds to the (K^-, K^-) events which remained even after the particle identification described in Section 3.3.2 and beam $K^- \to \mu^- + \bar{\nu_\mu}$ decay events resulted from the inefficiency of SMF. According to a theoretical calculation, the ${}^{4}_{\Lambda}\text{He}(0^+)$ ground state is predicted to be predominantly populated, while the ${}^{4}_{\Lambda}\text{He}(1^+)$ excited state is produced at a lower rate ($\sim$ 1/4 of ${}^{4}_{\Lambda}\text{He}(0^+)$) [26]. Therefore, the obtained peak is composed of ${}^{4}_{\Lambda}\text{He}(0^+)$ with a small contribution from ${}^{4}_{\Lambda}\text{He}(1^+)$, and the peak width of 5 MeV (FWHM) approximately corresponds to the missing mass resolution. Figure 3.12 (B) shows a fit result of the missing mass spectrum with two Gaussian functions and a background function where the threshold energy ($E_{>threshold}$) of 2.39 MeV (corresponds to $B_\Lambda = 0$) was taken from the emulsion experiment [9]. (See Section 3.6 for a description of background function.) The center position and the height of the second Gaussian

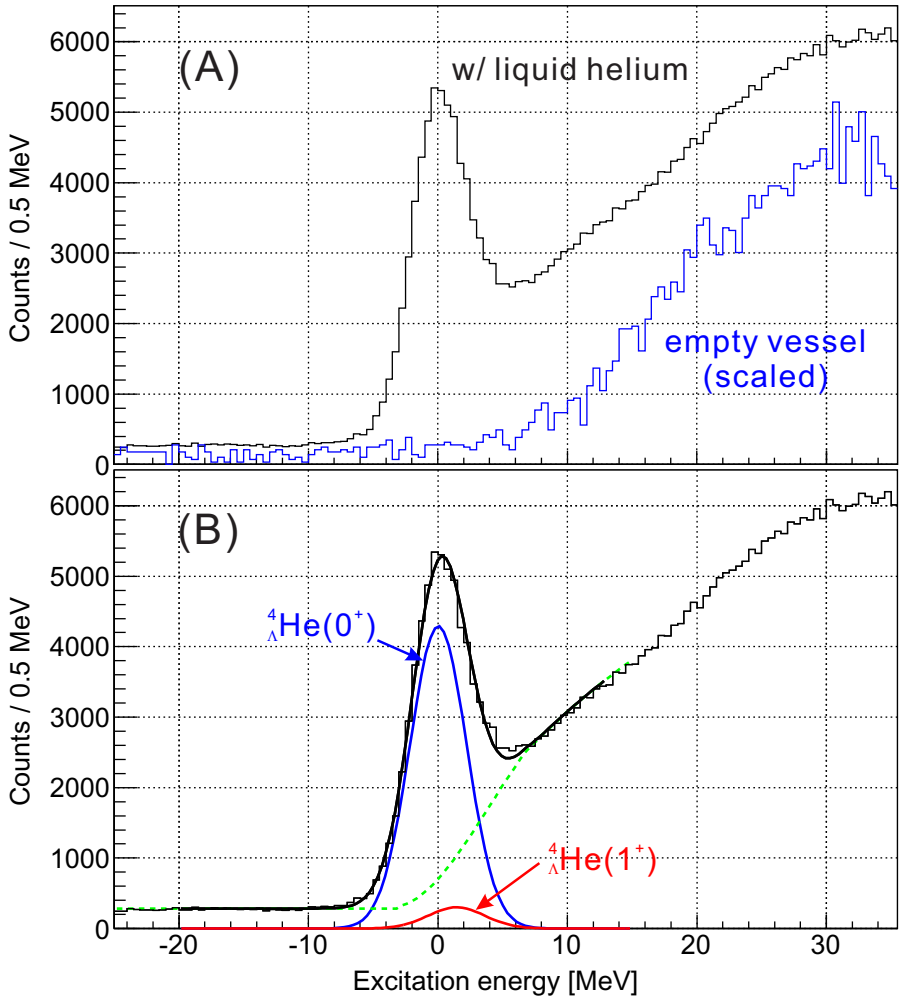

Figure 3.12: The missing mass spectrum for the ^{4}He$(K^-, \pi^-)^4_\Lambda$He kinematics plotted as a function of the excitation energy, $E_{\rm ex}$, where events with scattering angles ($\theta_{K\pi}$) larger than 3.5° are selected. In figure (A), black and blue lines show a spectrum with and without liquid helium, respectively. Figure (B) shows a result of the fitting using the result of the γ-ray analysis.

function was fixed according to the result of the present analysis (see Section 5.2). The obtained peak width [5.1(1) MeV (FWHM)] is consistent with the resolution in the test data of $^{12}_\Lambda$C production.

3.8 Information for the Doppler correction

A produced hypernucleus $^4_\Lambda$He has a recoil velocity (β) at the time of reaction, then slows down in the target medium. Figure 3.13 (A) shows a calculated initial velocity (β) of the produced $^4_\Lambda$He as a function of $\theta_{K\pi}$ for the (K^-, π^-) reaction with a beam momentum of

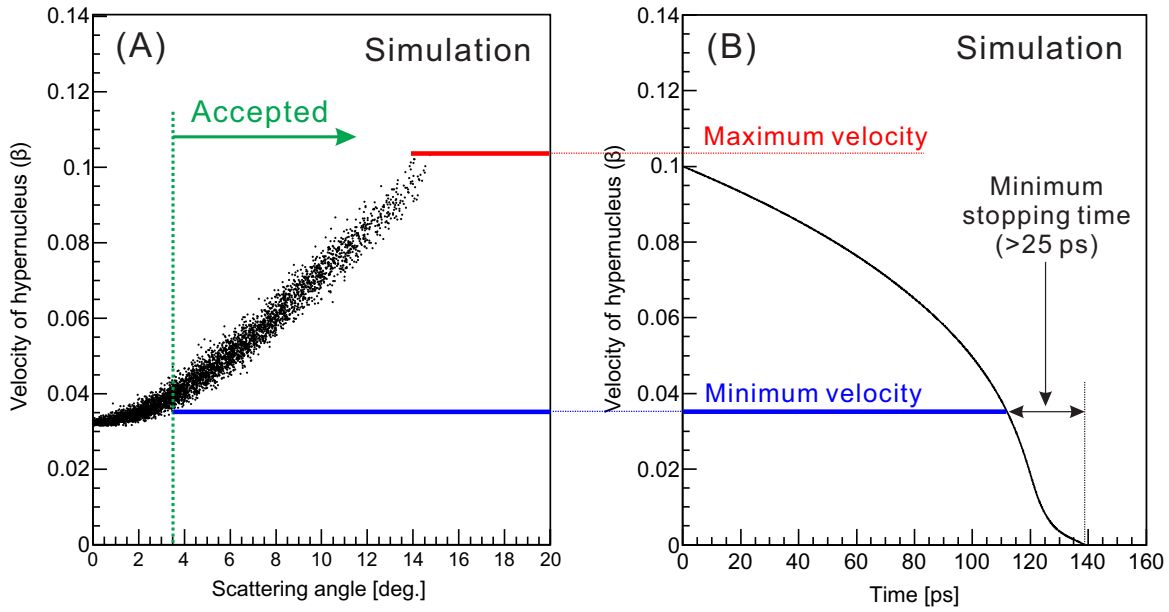

Figure 3.13: Calculated velocity and stopping time of the produced ${}^{4}_{\Lambda}$He, (A): initial velocity (β) of the produced ${}^{4}_{\Lambda}$He as a function of $\theta_{K\pi}$ for the (K^-, π^-) reaction with a beam momentum of 1.5 GeV/c, (B): changing rate of the velocity (recoil speed) of the ${}^{4}_{\Lambda}$He in the target medium.

1.5 GeV/c, and (B) shows a changing rate of the velocity of the ${}^{4}_{\Lambda}$He traversing the target medium estimated by a simulation using the SRIM code [51]. The minimum stopping time was estimated to be 25 ps. γ rays were emitted from ${}^{4}_{\Lambda}$He immediately after the production because of an estimated life time of the ${}^{4}_{\Lambda}$He(1^+) state is of $\sim$0.1 ps assuming weak coupling between the core nucleus and the Λ [52]. Then, the γ-ray energy measured by Ge detectors was shifted due to Doppler effect.

In the analysis of the Ge detectors, the Doppler correction is applied to obtain γ-ray energy spectra by using a following equation,

$$E_\gamma^{\rm corrected} = E_\gamma^{\rm measured} \cdot \frac{1}{\sqrt{1-\beta^2}}(1 - \beta\cos\theta_\gamma),$$

where $E_\gamma^{\rm corrected}$ and $E_\gamma^{\rm measured}$ are a corrected γ-ray energy and a measured energy by the Ge detector, respectively, β denotes velocity of the hypernucleus, θ_γ is an angle between the momentum of the hypernucleus and the γ-ray. The momentum and the velocity (β) of ${}^{4}_{\Lambda}$He just after the reaction are used for the Doppler-shift correction. Reduction of β in 0.1 ps after the reaction is estimated to be less than 0.05%. The γ-ray vector is defined as a vector from the reaction vertex point to the center position of the registered Ge crystal. The spatial distance between the γ emission point and the reaction vertex

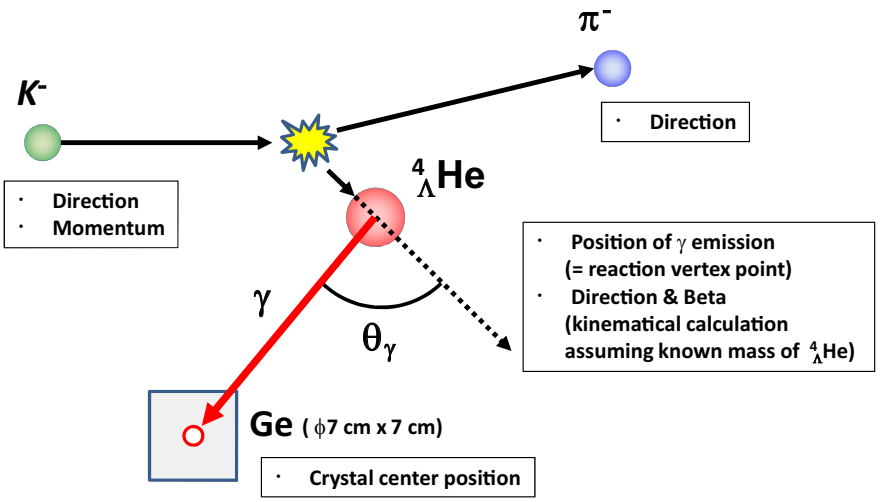

Figure 3.14: Illustration of the Doppler-shift correction.

is expected to be less than 10 μm with a life time of 0.1 ps, and thus is negligibly small comparing with the vertex resolution ($\sim$20 mm) and the size of Ge crystal (ϕ70 mm$\times$70 mm^L). Figure 3.14 illustrates the Doppler-shift correction method.

The information from the (K^-, π^-) analysis used for the Doppler-shift correction is summarized below:

- recoil momentum of hypernuclei,
- reaction vertex position as a point of γ-ray emission.

In the following section, calculation of the recoil momentum of the produced hypernuclei and estimation of the reaction vertex resolution are described.

Recoil momentum of hypernuclei

The recoil momentum of hypernuclei was calculated using reconstructed tracks from the (K^-, π^-) analysis by using kinematical conservation laws. For the calculation, inputs are listed as follow: (1) the vectors of the incident kaon and the scattered pion, (2) the measured momentum of the incident kaon (p_K), (3) the known mass of ${}^4_\Lambda$He(0^+) + 1 MeV(excitation energy). The measured momentum of the scattered pion (p_π) is not used in this calculation because of uncertainty in the calibration of the absolute momentum scale based on the calculated magnetic field map. The Λ binding energy for the ${}^4_\Lambda$He(0^+) of 2.39 MeV was taken from the past emulsion experiment [9]. The effect of a 1 MeV change in the ${}^4_\Lambda$He mass is estimated to be negligibly small. The accuracy of the velocity of the hypernucleus was estimated to be 1.2% (< 0.001 in β) from a simulation.

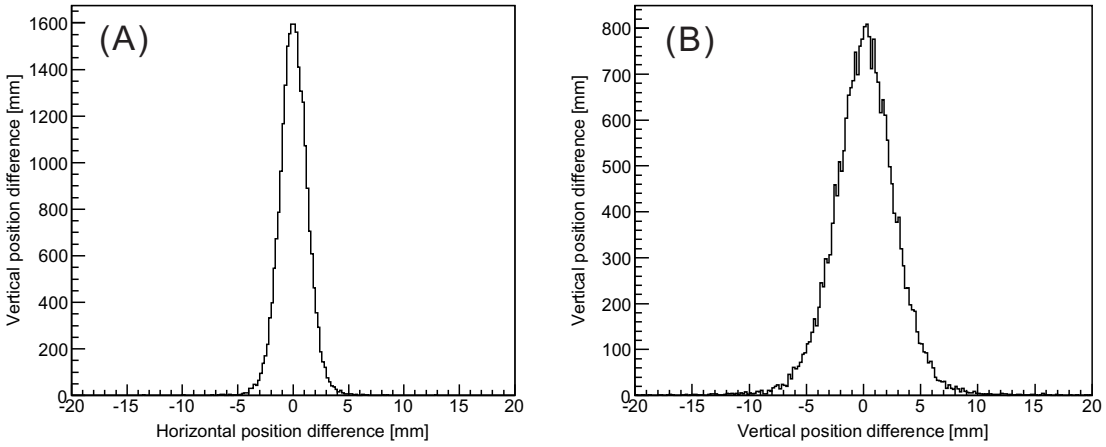

Figure 3.15: (A) distribution of a difference in the x-position of the incident vector and the outgoing vector at the target, (B) that in the y-position.

Reaction vertex resolution

In the analysis of Ge detectors, we estimated a γ-ray peak width after the Doppler-shift correction (see Section 5.3). The reaction vertex resolution was used as an input in this estimation.

x- and y-vertex position

The x- and y-vertex position resolutions were checked by using data with a liquid helium target, in which the beam particles pass through both the beam line spectrometer and SksMinus. In these events, x and y positions of the incident vector and of the outgoing vector at the target should be identically the same. Figure 3.15 (A) shows a distribution of a difference in the x-position of incident vector and the outgoing vector at the target, reconstructed from the analysis of the beam line spectrometer and SksMinus, respectively. Similarly Figure 3.15 (B) shows a distribution for the y-position. The resolutions of x- and y-vertex positions were 1.2 mm and 2.6 mm (σ), respectively.

z-vertex position

The z-vertex resolution was checked with a thin stainless steel (SUS) target (t=3 mm) data. Figure 3.16 shows z-vertex distributions at $\theta_{K\pi}$=4°–6°, 6°–8°, and 8°–10° for the beam particle scattered off the SUS target. The z-vertex resolution was obtained by a fit of this spectrum and is shown in Fig. 3.17 as a function of $\theta_{K\pi}$. The resolution of the z-vertex position was 22 mm (σ) at $\theta_{K\pi} = 5°$. The effect of the thickness of the SUS target (t=3 mm) is estimated to be less than 0.1 mm (σ) for the obtained resolution,

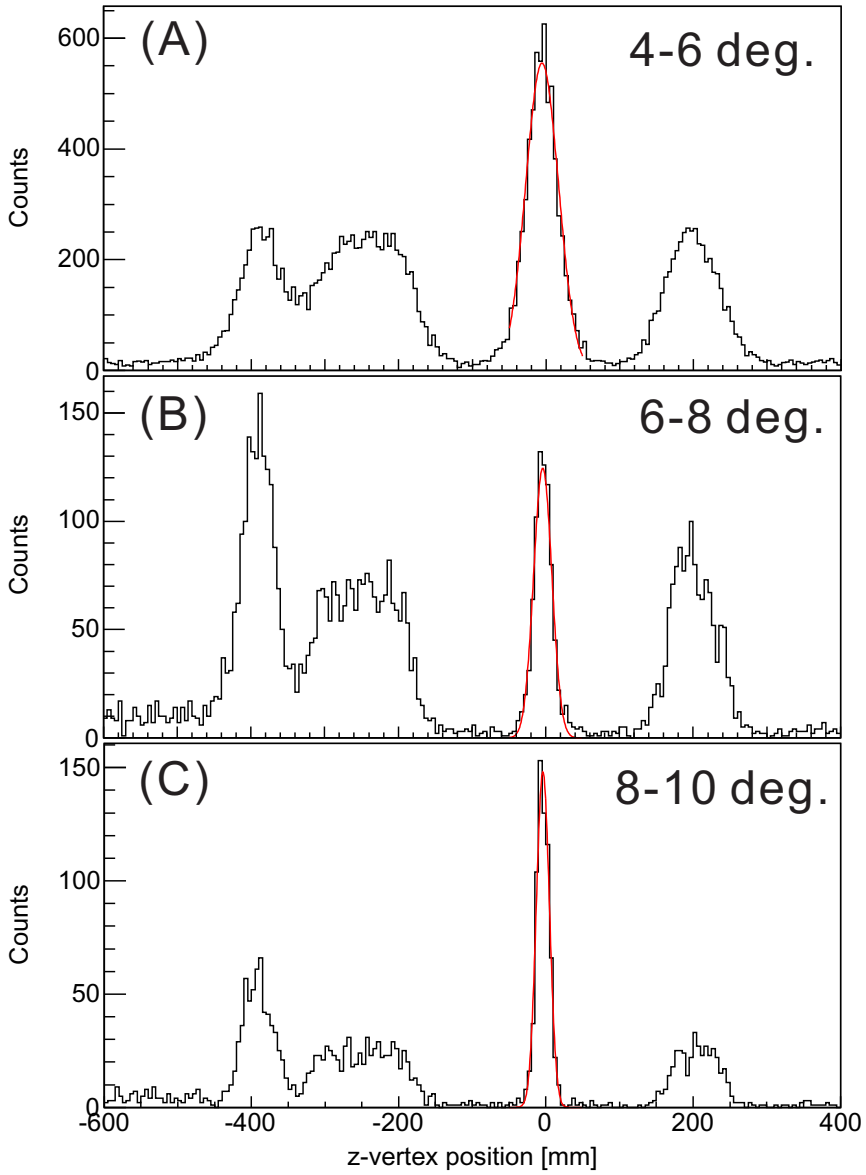

Figure 3.16: Z-vertex distributions with the SUS target for the beam particle scattering events. (A), (B) and (C) are for the scattering angles ($\theta_{K\pi}$) of 4°–6°, 6°–8°, and 8°–10°, respectively.

and thus is ignored in the estimation.

With the liquid helium target, of which length in z-axis is longer (∼230 mm) than that of the SUS target, the z-vertex resolution becomes worse due to a multiple scattering effect. This effect was estimated by a simulation using the GEANT4 code [32]. The simulated z-vertex resolutions are shown together in Fig. 3.17; black line and red line shows the simulated values with the thin SUS target and with the long helium target, respectively. From these results, the difference in z-vertex resolution between the SUS

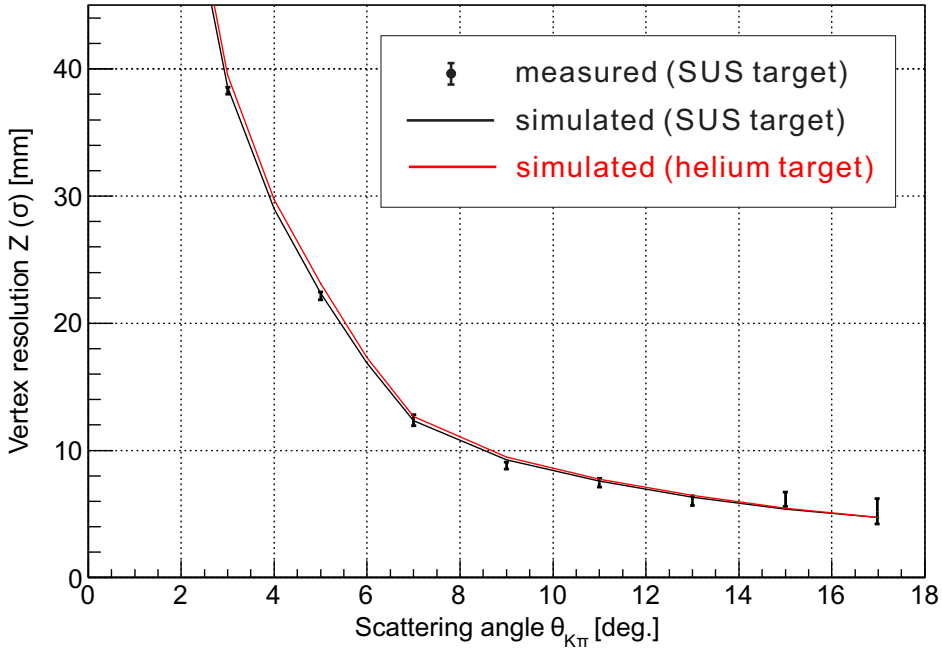

Figure 3.17: z-vertex resolution as a function of $\theta_{K\pi}$ obtained by a fitting of data with thin SUS target (t=3 mm). Black and red line are simulated vertex resolutions with the thin SUS target and the long liquid helium target, respectively.

target and the liquid helium target is estimated to be ∼1 mm at $\theta_{K\pi}$=5°. The estimated resolutions for the liquid helium target was used for the peak shape simulation. The accuracy of the simulated resolution is expected to be less than 2 mm, which is obtained from the difference between the measured and estimated resolutions.

3.9 Performance of decay suppression counter

The efficiencies of SP0 and SMF for beam-decay events were checked with the KPI trigger for the empty target, where only K^- decay events make the KPI trigger. $K^- \to \pi^- + \pi^0$ and $K^- \to \mu^- + \overline{\nu_\mu}$ events are selected by missing mass spectrum, gating corresponding mass regions for π^0 and $\overline{\nu_\mu}$. Figure 3.18 shows a missing mass square distribution reconstructed for $K^- \to \pi^- X$ kinematics, assuming $m_{\mu^-} \simeq m_{\pi^-}$.

$K^- \to \pi^- + \pi^0$ rejection using SP0

By selecting number of hit layers in SP0 with setting threshold for the number, $K^- \to \pi^- + \pi^0$ events can be suppressed. The suppression with SP0, however, was not applied in the present analysis for ${}^{4}_{\Lambda}$He production because of a large branching ratio of π^0 emission decay channel leading ∼6% yield loss [53]. Figure 3.19 shows number of hit layers for

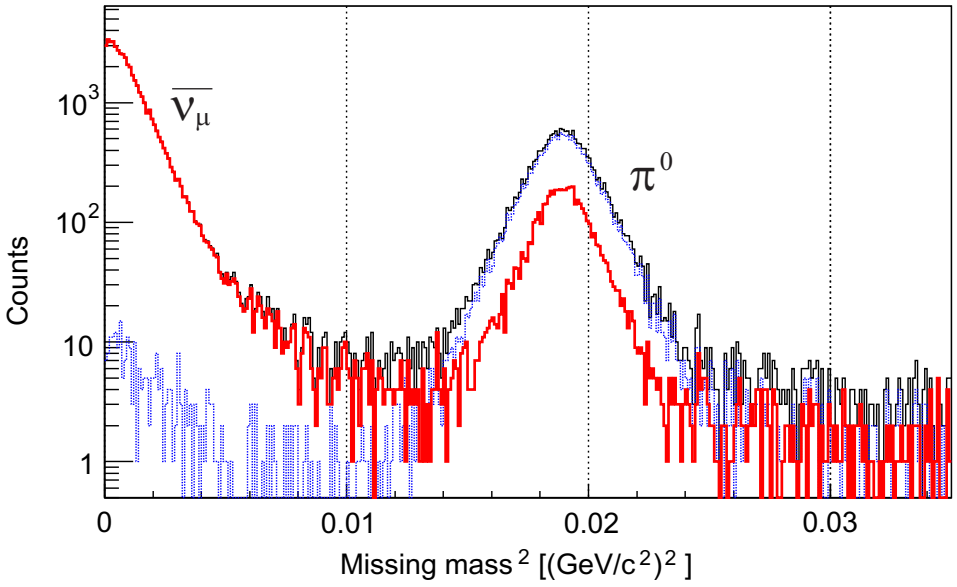

Figure 3.18: Missing mass square (M^2) distributions for the KPI trigger with empty target, reconstructed by missing mass analysis for empty$(K^-, \pi^-)X$ kinematics (solid black line). Enhancements around $M^2 = 0$ and $= 0.02$ correspond to particles from K^- decay, $\overline{\nu_\mu}$ and π^0, respectively. Decay events can be suppressed by SP0 multiplicity cut (thick red line) and SMF cut (dotted blue line).

events of the decay channel. The numbers for events of Σ^+ production via the (K^-, π^-) reaction was also shown, from where miss-identification ratio for hypernuclear production due to detecting π^0 from Λ decay can be checked, considering analogy between Λ and Σ^+ in out going particles from their decay. These show different distributions; decay events fire 1–8 layers while 0–2 for Σ^+ production events. Setting hit layer threshold as 3, more than 69% of the decay events were tagged for over all SksMinus acceptance as shown in Fig.3.18 and 3.19, while miss-identification ratio of Σ^+ production is obtained to be $\sim$11%. Focusing on scattering angles of 2°–4° in where the decay events kinematically overlap with hypernuclear production events as shown in Fig.3.20, the suppression efficiency is 54%. Miss-identification ratio for ${}^{12}_{\Lambda}$C production events is estimated to be $\sim$2% by Monte Carlo simulation considering decay branching ratio [46] and minor difference with Σ^+ decay [53]. Suppression performance of SP0 is summarized in Table 3.9.1.

$K^- \to \mu^- + \overline{\nu_\mu}$ rejection using SMF

By requiring SMF hit, more than 99.5% of $K^- \to \mu^- + \overline{\nu_\mu}$ events were suppressed as shown in Fig. 3.18. Miss-identification of hypernuclear production events can be caused by scattered π^- which is not stopped in the iron block and also by neutrons and γs generated from the absorption of π^-. To check this effect, the over-kill probability for

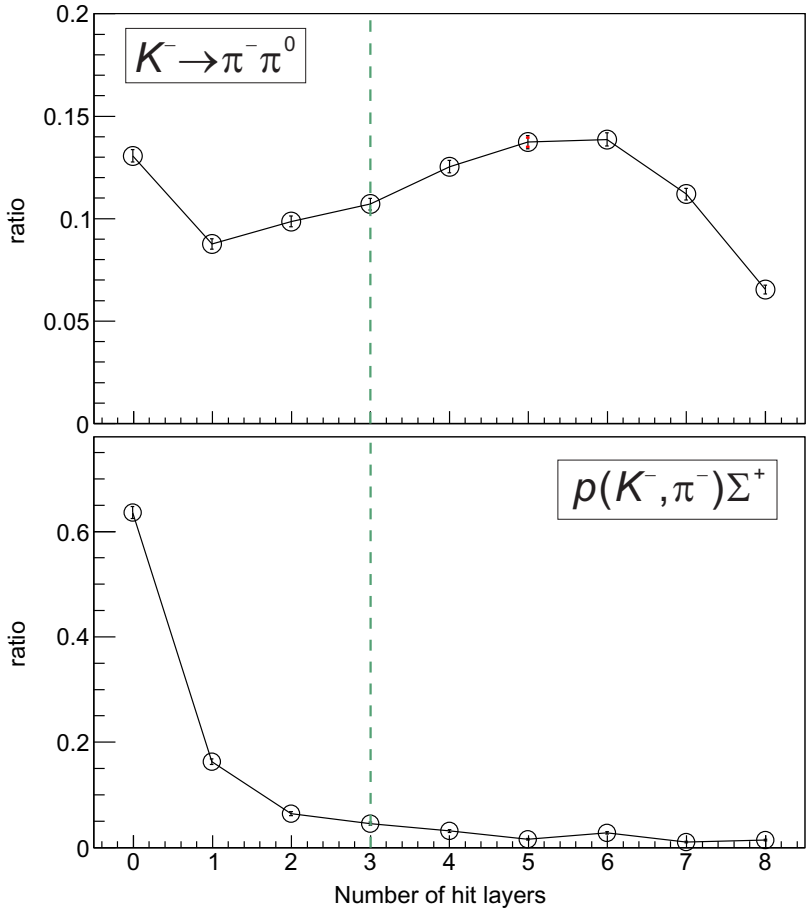

Figure 3.19: Number of hit layers of SP0 for $K^- \to \pi^- + \pi^0$ decay events (upper) and Σ^+ production events (lower). The layer multiplicity threshold is set to be >3 as shown in dashed green line.

Table 3.9.1: Suppression efficiency of SP0 and SMF

	Efficiency
SP0 efficiency (layer multiplicity ≥ 3)	
$K^- \to \pi^- + \pi^0$ events (θ:1–12°)	69(1)%
$K^- \to \pi^- + \pi^0$ events (θ:2–4°)	54(1)%
Σ^+ production events	11(1)%
SMF efficiency	
$K^- \to \mu^- + \overline{\nu_\mu}$ events (θ:1–14°)	99.5(1)%
$K^- \to \mu^- + \overline{\nu_\mu}$ events (θ:5–7°)	99.5(1)%
Σ^+ production events	13(1)%

Σ^+ production was measured to be ∼13%. The probability for hypernuclear production is estimated to be ∼10% [53]. Suppression performance of SMF is also summarized in Table 3.9.1. By adding the SMF (veto) signal to the trigger, the trigger rate was reduced

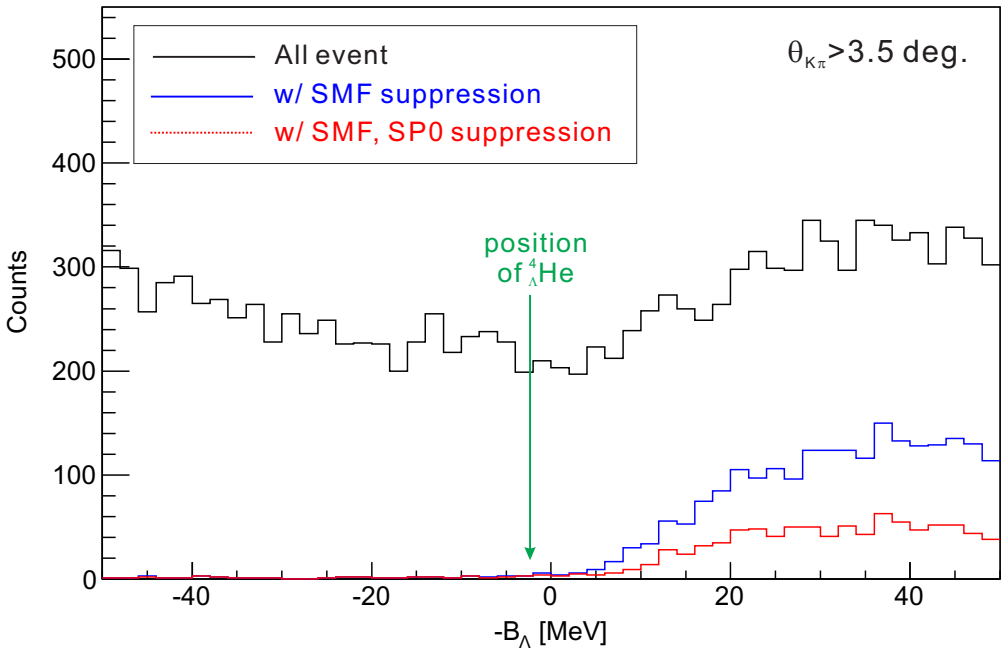

Figure 3.20: Binding energy spectra with empty target reconstructed for ^{4}He$(K^-, \pi^-)^4_\Lambda$He kinematics. Decay events (black line) which overlap to region of the hypernuclear production (green lines) can be suppressed using SMF as shown in blue line. Dotted red lines show spectra in which both SMF and SP0 are used for the suppression.

to $\sim$43% leading 37% increase of the efficiency of the data-acquisition system.

Effect of the beam decay suppression on the missing mass spectrum

Figure 3.20 shows missing mass distribution for K^- decay events obtained with empty target, reconstructed for ^{4}He$(K^-, \pi^-)^4_\Lambda$He kinematics. The distribution with suppression using SP0 and SMF are also shown. More than 95% of background events in hypernuclear mass region can be suppressed by using SMF, leading to better S/N ratio in the γ-ray energy spectrum as well as in the hypernuclear mass spectrum. The contamination from the π^0 emission decay channel was small in the hypernuclear bound region when events in which the scattering angle ($\theta_{K\pi}$) of $<3.5^\circ$ are selected.

Chapter 4

Analysis II - γ rays

The analysis of Hyperball-J (the Ge detectors and the PWO counters) to obtain the γ-ray energy spectrum is described in this chapter. Following this analysis, hypernuclear γ-ray energy spectra before/after the Doppler-shift correction were obtained combining with the analysis of the (K^-, π^-) reaction described in the previous chapter.

4.1 Outline

The analysis procedure of Hyperball-J is illustrated in Fig. 3.1 and also summarized below:

- event selection by using timing information of the Ge detectors and the PWO counters,
- energy calibration of the Ge detectors,
- Doppler-shift correction for γ-ray energy,
- simulation of a peak shape in the Doppler-shift corrected spectrum.

4.2 Event selection

The timing signal from the Ge detectors was not used for the KPI trigger. The accepted coincidence time window between the Ge signal and the KPI trigger (= BH2 timing) was very wide (2.5 μs) in the trigger level. This window corresponds to the gate width for the peak-sensitive ADC modules for the readout of the Ge detectors, and is much wider than the time resolution of the Ge detector ($\sim$15 ns at E_γ= 1 MeV). Therefore, an event selection using a tight time window was applied to improve a signal to noise ratio in the γ-ray energy spectrum.

Furthermore, background events from incomplete charge correction of the Ge detectors and from Compton scattering were rejected in the off-line analysis described in this section.

4.2.1 Coincidence events with the (K^-, π^-) reaction

To select γ rays from the produced hypernuclei in the off-line analysis, we took a coincidence between the Ge detector and the KPI trigger, using timing information of the Ge detectors which was processed through the Timing-Filter Amplifier (TFA) and the Constant-Fraction Discriminator (CFD) and then was digitized by the multi-hit TDC modules. CFD modules were used because of a large dynamic range of Ge signals which results in pulse height (energy) dependent timing. Even though the timing signal was processed through the CFD modules, the recorded timing distribution has a correlation with the ADC value. Figure 4.1 shows a typical correlation between the timing distribution (Ge detector$-KPI$ trigger) and the measured γ-ray energy (E_γ). A tight timing window can be applied for an energy region of $E_\gamma > 600$ keV, while a wider window is necessary for the lower energy region. In the present analysis, however, we concentrated on the energy region of ~ 1 MeV for the γ ray from ${}^{4}_{\Lambda}$He. Figure 4.2 shows a typical

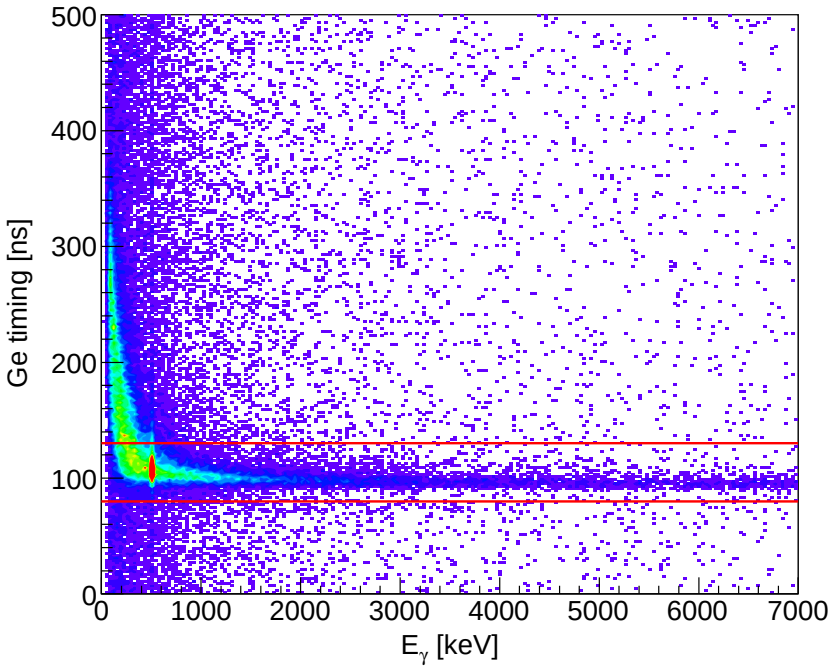

Figure 4.1: Typical correlation between the timing distribution (Ge detector$-KPI$ trigger) and the measured γ-ray energy (E_γ).

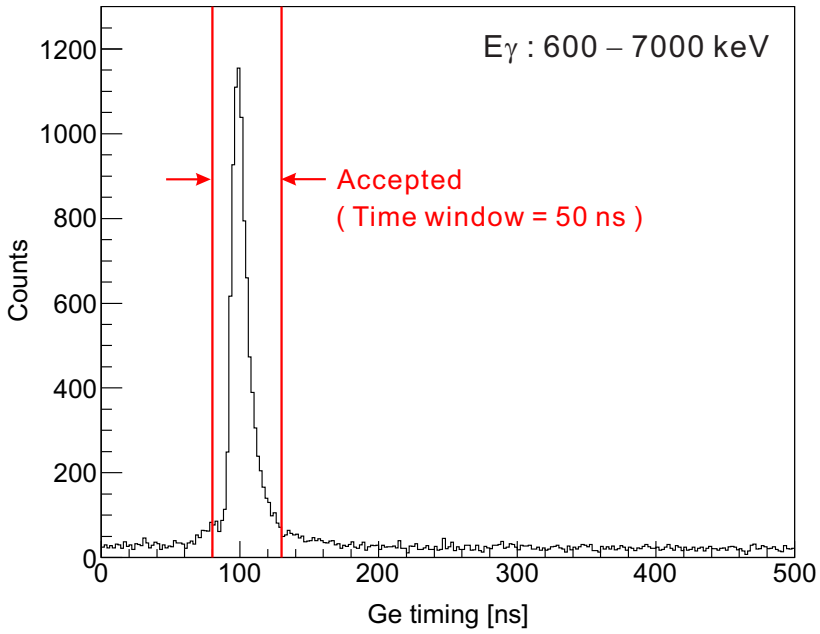

Figure 4.2: Typical timing distribution for an energy region of $E_\gamma > 600$ keV.

timing distribution for an energy region of 600 keV $< E_\gamma <$ 7000 keV. A typical time resolution of the Ge detector was 13 ns (FWHM) for the measured energy region of 600–7000 keV. Also the width of the timing window for this event selection was set typically 50 ns, which was optimized for each Ge detector.

4.2.2 Background events

Preamplifier reset and pulse pileup

In the pulse shaping process by the main amplifier (UHA 973U), some of the pulses suffer from two factors: (1) a base line shift in the output signal of UHA 973U caused by the reset of the preamplifier, (2) a signal pileup which occurs when more than two pulses arrive within the integration time of UHA 973U.

When a pulse rides on a distorted base line following a reset, the measured pulse height and thus the energy will be shifted in peak-sensitive ADC modules. Figure 4.3 shows a typical correlation between the ADC value and the timing of the reset. In the figure, the Reset Time (RT) was defined as "KPI trigger - reset signal from the preamplifier". The reset timing pulse was output from the preamplifier and then was digitized by the multi-hit TDC. The effect of the base line shift is seen in the region of RT $\simeq$ 40 μs. Furthermore, the reset makes a fake peak at a particular energy ($\sim$300 keV) for a typical detector as shown in Fig. 4.3. The recorded energy of the fake peak is

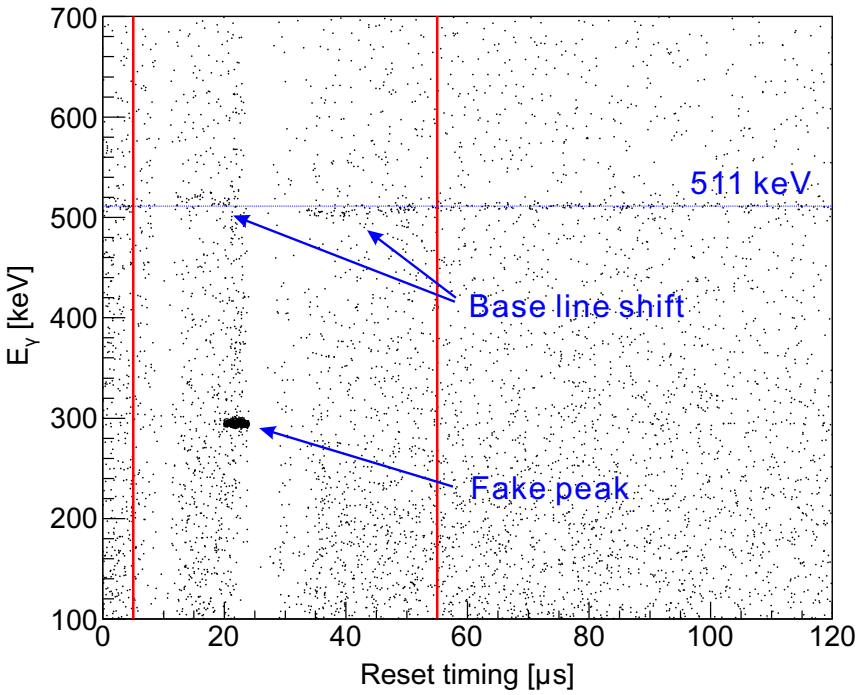

Figure 4.3: Typical correlation between the ADC value and the Reset Time (RT= KPI trigger - reset signal).

less than 600 keV. Therefore, the fake peak will not affect in the energy region of $E_\gamma >$ 600 keV, even when the event selection with the reset timing associated with the fake peak was not applied. To reject pulses affected by the reset, hit information of a Ge detector was removed in the off-line analysis, when the recorded reset timing is in the gate of 5 μs $<$ RT $<$ 55 μs. The time window is illustrated in Fig. 4.3.

The pulse height for the piled-up events become larger because of summing of more than one pulse within the integration time of the UHA 973U module, which is set to be 3 μs in the present experiment. Therefore, those events in which there is more than one hit in a Ge detector in the $\pm$3 μs time gate were removed in the off-line analysis.

Background suppression with PWO counters

Backgrounds in the γ-ray spectrum originate from such as Compton scattering, electro magnetic shower due to high energy γ rays from π^0 decay, and passing of a high energy charged particle. These events can be suppressed by taking an anti-coincidence between the Ge detector and surrounding PWO counters (see Section 2.4 for the description of the detector configuration). Figure 4.4 shows a typical time distribution of the PWO counters, where the time difference between the PWO counter and the KPI trigger (=

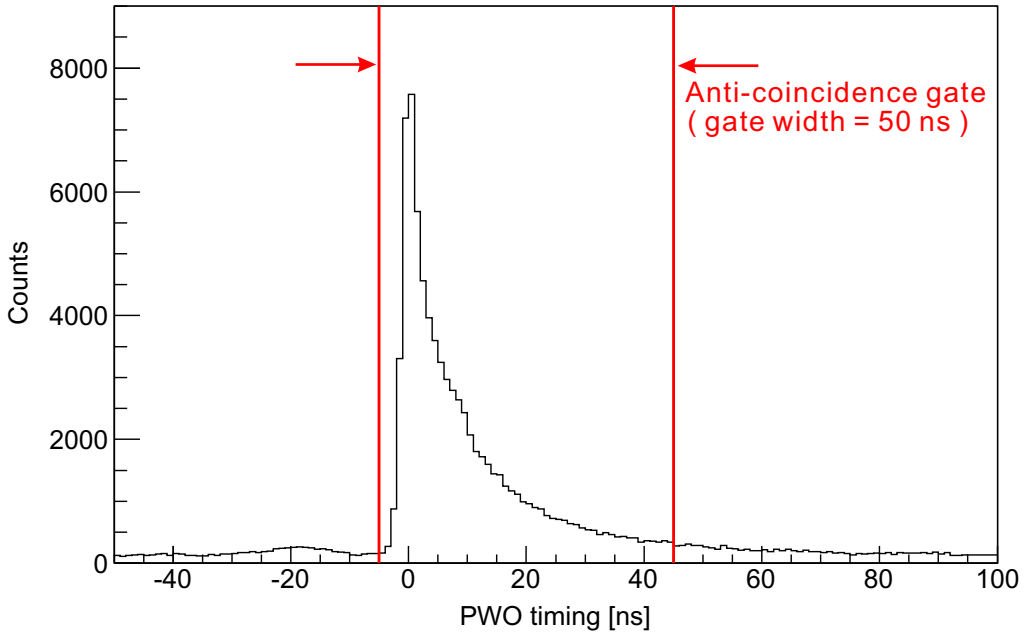

Figure 4.4: Typical time distribution of the PWO counters. The time difference between the PWO counter and the KPI trigger (= BH2 timing) is used.

BH2 timing) is used instead of the corresponding Ge detector timing which has worse time resolution than BH2. The time resolution of the PWO counters was 8 ns (FWHM). The anti-coincidence gate width was set to be 50 ns, which was studied in the test experiment with a known γ ray from ^{10}B [54]. The anti-coincidence gate was illustrated in the Fig. 4.4. The rate of accidental killing of good events was estimated to be 1% in the present analysis, which is smaller than that with conventional BGO counters, due to the short decay constant of the PWO crystal.

Figure 4.5 shows the γ-ray energy spectra for the KPI triggered events before/after the background suppression with the anti-coincidence of the PWO counters. In the spectrum, the event selection based on the timing information of the Ge detectors (the TFA timing cut, the preamplifier reset and the pulse pileup rejection) was made. As shown in this figure, the background events were suppressed while the γ-ray peaks from normal nuclei were not. The suppression efficiency depends on the γ-ray energy. Background events were suppressed by a factor of $\sim$3 at the energy region of $E_\gamma = 1$ MeV.

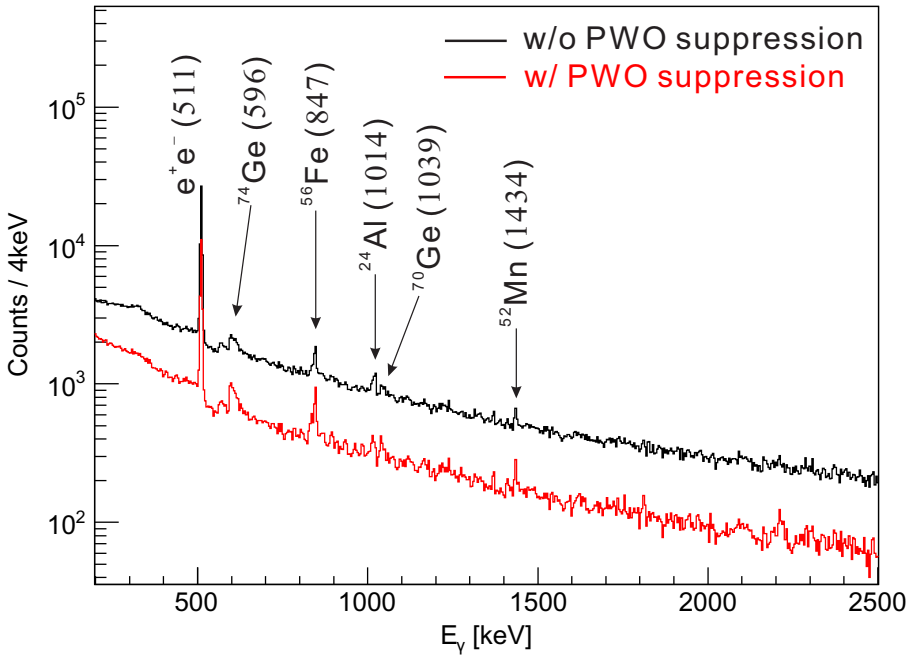

Figure 4.5: γ-ray energy spectra for the KPI triggered events before/after the background suppression with the anti-coincidence of the PWO counters. In the spectrum, event selection with the timing information of the Ge detectors (the TFA timing cut, the preamplifier reset and the pulse pileup rejection) was done.

4.3 Energy calibration of Ge detectors

The energy calibration for the Ge detector can be separated in two steps; the first is to obtain an energy calibration curve in the off-beam-spill period, and the second is correction of a peak shift between the on-beam-spill and the off-beam-spill periods. These two analyses for the energy calibration are described in this section.

4.3.1 Calibration curve

The energy range of the Ge detectors was set to be 0.15–7 MeV. The low energy end (0.15 MeV) corresponds to the threshold of CFD. The high energy end (7 MeV) was decided because the highest γ-ray energy from $^{19}_{\Lambda}$F is expected to be $\sim$6 MeV. (We also took data for a γ-ray spectroscopy of $^{19}_{\Lambda}$F with the same setup, and the result will be reported elsewhere.) In the present analysis, we concentrated on the energy region of $\sim$1 MeV for γ rays from $^{4}_{\Lambda}$He. Therefore, the energy calibration was performed for the narrow energy region of 0.5–2.6 MeV. We applied a two-step calibration by using the off-beam data. First, a gain drift is corrected by applying a rough energy calibration with γ rays from the Th-series source during the beam time on daily basis. Second, an

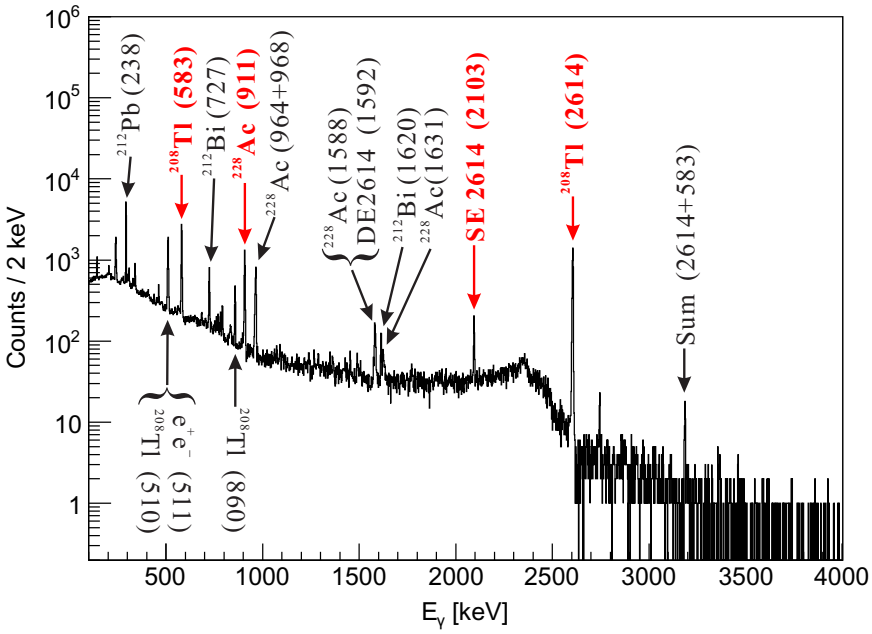

Figure 4.6: γ-ray energy spectrum with the Th-series source. The data was taken with the Ge self-trigger in the off-beam-spill. The data taking time was $\sim$1 hour.

Table 4.3.1: Selected γ rays from the Th-series source for the gain shift correction. SE denotes a Single-Escape peak.

Parent nucleus	γ-ray energy [keV]
^{208}Tl	583.2
^{228}Ac	911.2
^{208}Tl (SE 2614 keV)	2103.5
^{208}Tl	2614.5

energy calibration curve is obtained with γ rays from ^{152}Eu just after the beam time.

We took calibration data with the Ge self-trigger (see Section 2.7) in the off-beam-spill period, where γ rays from the Th-series source installed adjacent to each Ge detector were observed. Figure 4.6 shows a γ-ray energy spectrum obtained with the Ge self-trigger in the off-beam-spill, for $\sim$1 hour which equals the run cycle of the KPI triggered data. γ-ray peaks are seen between 0.5 and 2.6 MeV in this spectrum. We selected four γ-ray peaks as "clean peaks" and used them for correcting the gain shift. The selected γ rays from the Th-series source are listed in Table 4.3.1. The other peaks were not used because of overlap with other γ-ray peaks or insufficient statistics after one day data taking. Figure 4.7 shows drift of the peak position of 2.6 MeV (^{208}Tl) γ ray for a typical Ge detector through out the data taking period where x-axis is a run number of the KPI triggered data. The drift of the peak position was $\pm$0.8 ADC channel, corresponding

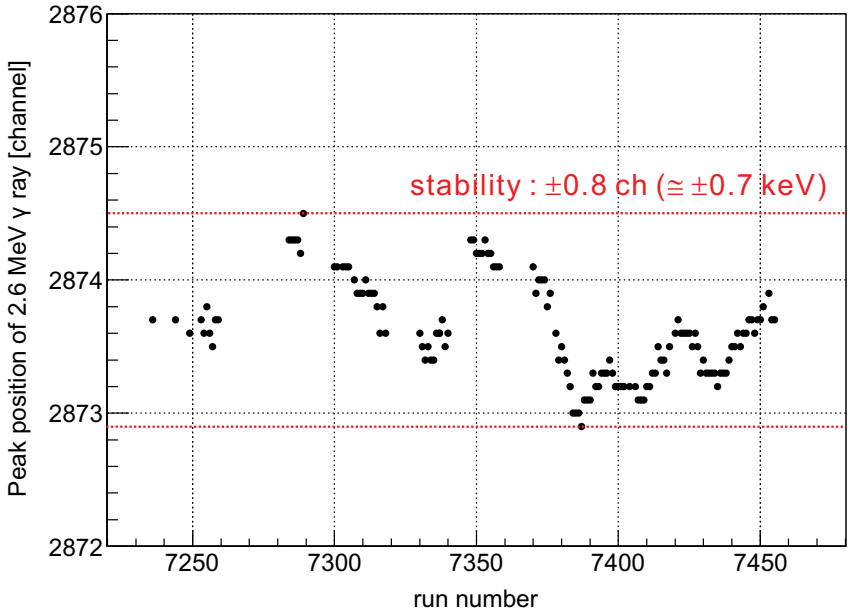

Figure 4.7: Peak position drift of the 2.6 MeV (^{208}Tl) γ ray for a typical Ge detector through out the data taking period (10 days in total), where x-axis is a run number of the KPI triggered data.

to $\pm$ $\sim$0.7 keV. To correct this gain shift, a rough calibration curve was determined by fitting these calibration energies with a 2nd-order polynomial function.

A more accurate calibration curve was obtained with the data taken just after the beam time, where γ rays from ^{152}Eu source were added. 4th-order polynomial correction function was obtained by fitting the "roughly energy calibrated" peak positions of γ rays from ^{152}Eu and Th-series source. γ-ray peaks used in the fitting are listed in Table 4.3.2. Figure 4.8 shows residuals of the fitting. Accuracy of the energy calibration for the whole data set is discussed in Section 4.5.1.

4.3.2 Peak shift

In beam-on conditions, γ-ray peak positions shifted to lower energy by 1 keV or less compared to the beam-off conditions. A higher single counting rate of the Ge detector caused the base line to shift in the main amplifier (UHA 973U). A similar shifting of peaks was also observed in the previous experiments with Ge detector arrays, Hyperball and Hyperball-2 [55, 56, 57]. To correct for the peak shift, measured γ-ray energies were shifted by a constant value so as to bring the annihilation peak to 511 keV. We did not include a gain shift in this correction. No gain shift was observed from the measured peak position of the 2614-keV γ-ray peak in all summed up spectrum of the on-beam-spill,

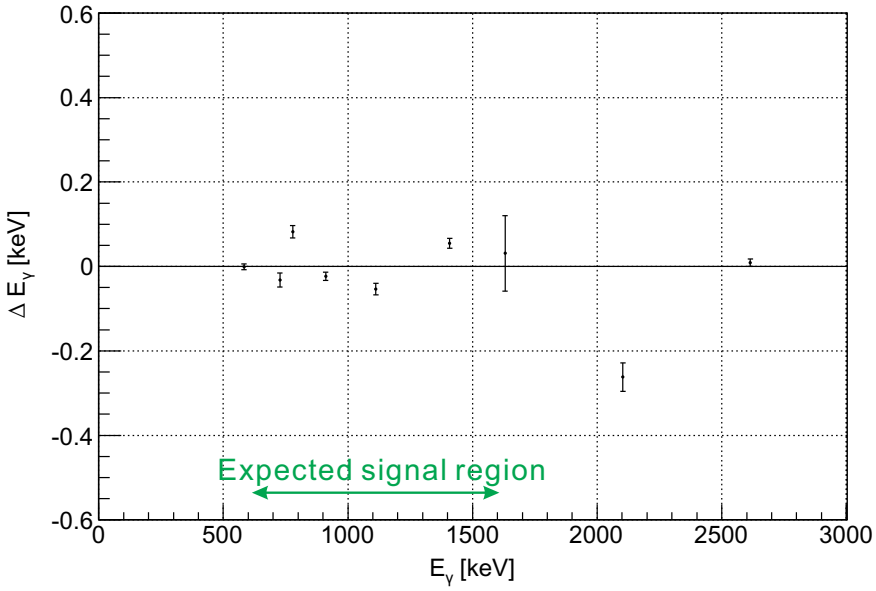

Figure 4.8: Residuals of the fitting to obtain the energy calibration curve for typical Ge detector with ^{152}Eu and Th-series sources.

Table 4.3.2: γ-ray peaks used in the fitting for accurate energy calibration. SE denotes a Single-Escape peak.

Parent nucleus	γ-ray energy [keV]
^{208}Tl	583.19
^{212}Bi	727.33
^{152}Eu	778.90
^{228}Ac	911.20
^{152}Eu	1112.07
^{152}Eu	1408.00
^{228}Ac	1630.63
^{208}Tl (SE 2614 keV)	2103.51
^{208}Tl	2614.51

which peak can be appears by an accidental coincidence with the KPI trigger.

4.4 Doppler-shift correction

The $M1$ γ-ray transition from ${}^{4}_{\Lambda}$He is expected to be Doppler broadened because the life time of ${}^{4}_{\Lambda}$He(1^+), estimated to be of $\sim$0.1 ps assuming the excitation energy of 1 MeV, is much shorter than the stopping time of the recoiling ${}^{4}_{\Lambda}$He ($>$ 25 ps). See Section 3.7 for the detailed description of the Doppler broadening.

Measured γ-ray energies were corrected for the Doppler shift event by event by using

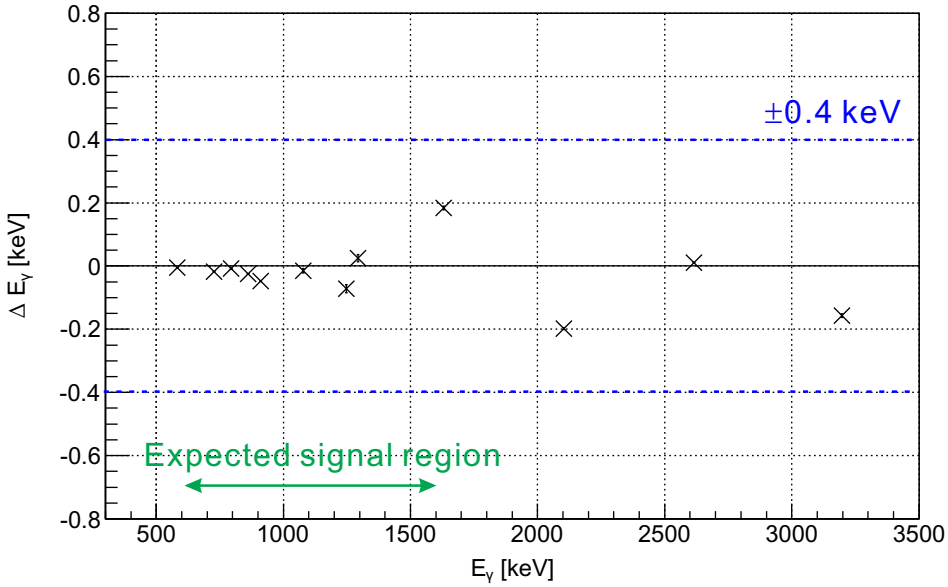

Figure 4.9: Residuals of the measured γ-ray energy position from known energies. The residuals were obtained by using data accumulated in the over all the off-beam-spill period and summed up for all of the Ge detectors.

the following equation,

$$E_\gamma^{\rm corrected} = E_\gamma^{\rm measured} \cdot \frac{1}{\sqrt{1-\beta^2}}(1-\beta\cos\theta_\gamma),$$

where β denotes the recoil speed of ${}^{4}_{\Lambda}$He obtained from the analysis of the (K^-, π^-) reaction. θ_γ is the angle between the γ-ray vector and the momentum of ${}^{4}_{\Lambda}$He, where γ-ray vector originates from the reaction vertex point and ends at a center position of the Ge crystal with a hit. The effect of the Doppler-shift correction is described in the next section, and its accuracy is described in Section 5.3.

4.5 Performance of Hyperball-J

4.5.1 Accuracy of the energy calibration

The accuracy of the energy calibration over the entire data-taking period was checked by using data accumulated in the off-beam-spill period, and summed up for all the beam time. Figure 4.9 shows the residuals between measured and their known γ-ray energies. In this figure, only prominent peaks are shown; the others have insufficient statistics or overlap with neighboring peaks. A overall accuracy of the energy calibration in the range of 0.6–2.6 MeV was estimated to be less than 0.4 keV from these residuals.

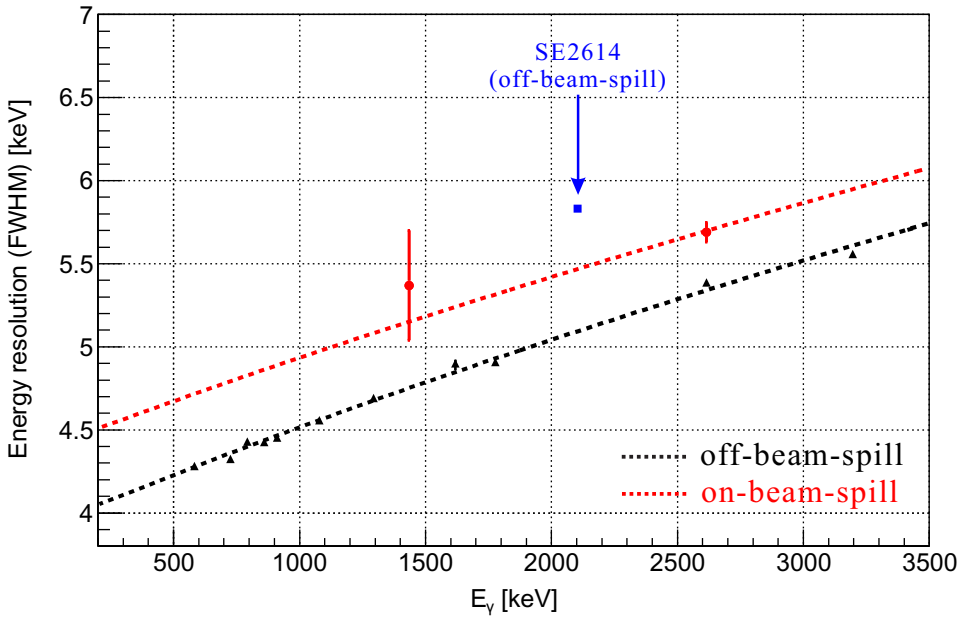

Figure 4.10: Energy resolution in FWHM as a function of the γ-ray energy. Black triangle shows measured energy resolutions from the off-beam-spill data, and red point shows the in-beam resolution. The resolution functions ($\sqrt{A \cdot E_\gamma + B^2}$) for the off-beam-spill (dotted black line) and for the on-beam-spill (dotted red line) are also shown.

4.5.2 Energy resolution

The energy resolution of Hyperball-J was measured by summing up all of the off-beam-spill data (Ge self-triggered data) for all the Ge detectors. Figure 4.10 shows the energy resolution in FWHM as a function of the γ-ray energy. The peak width of Single-Escape (SE) peak of 2614-keV γ ray at 2103 keV is broadened by in-flight annihilation of a positron with an electron. The energy resolution is expected to be a root-squared function of the energy as

$$\delta E = \sqrt{A \cdot E_\gamma + B^2},$$

where parameters A and B are obtained by fitting the measured energy resolution excluding the 2103-keV peak. The obtained function is also shown in Fig. 4.10 with A = 5.03(4) $\times 10^{-3}$ keV and B = 3.92(1) keV. The in-beam resolution was checked with the 1434-keV (^{52}Mn) and the 2614-keV (^{208}Tl) peaks produced by the beam. They are seen in the KPI-triggered data without applying an event selection by taking coincidence between the Ge detectors and the KPI trigger. Under the in-beam condition, B = 4.40(8) keV was obtained by fitting these peaks with a fixed value of A from the off-beam-spill.

4.5.3 Expected peak shape with Doppler-shift correction

The γ-ray peak shape broadened by the Doppler effect and also its shape after the Doppler-shift correction were simulated. Conditions for the simulation are listed below,

- response function of the Ge detector for a stopped γ-emission peak was assumed to be Gaussian with the expected peak width described in Section 4.5.2,
- measured positions of the detector and the target were used,
- γ-ray source point was generated over the target volume taking the beam x- and y-profile into account,
- momentum of the hypernucleus was calculated with the ^{4}He$(K^-, \pi^-)^4_\Lambda$He kinematics assuming the mass of $^4_\Lambda$He to be $M(^3\mathrm{He})+M(\Lambda)-B_\Lambda(=2.39$ MeV$)+$ $E_{\mathrm{ex}}(=1$ MeV$)$,
- measured performance of the magnetic spectrometers, such as the reaction vertex resolution and the momentum resolution for a recoiling hypernucleus, were considered.

Figure 4.11 shows simulated peak shapes for the 1-MeV γ rays. The peak widths of the simulated peak shapes are 5, 90 and 14 keV (FWHM) for the stopped γ-emission peak, the Doppler-broadened peak and the Doppler-shift corrected peak, respectively. The simulated peak before the Doppler-shift correction has an asymmetric shape because the numbers of Ge detectors located at the upstream side and at the downstream side in Hyperball-J with respect to the target center are different. The peak width after the Doppler-shift correction is wider than the stopped γ-emission peak shape due to inaccuracy of the measured momentum of the hypernucleus, the reaction vertex position, and the γ-ray hit position (assumed to be the center of the Ge crystal).

4.5.4 Photo-peak efficiency

The absolute photo-peak efficiency of Hyperball-J was estimated by using a simulation based on the Geant4 code [32]. In the simulation, we incorporated the measured detector positions, all materials around the Ge crystals, and γ-ray absorption in the target medium. The efficiencies of the data acquisition system and the analysis were not taken into account.

Figure 4.12 shows the simulated total absolute photo-peak efficiency of Hyperball-J as a function of γ-ray energy. In this figure, a black line shows the efficiency with a point source placed at the center of Hyperball-J and without the target material, and a red

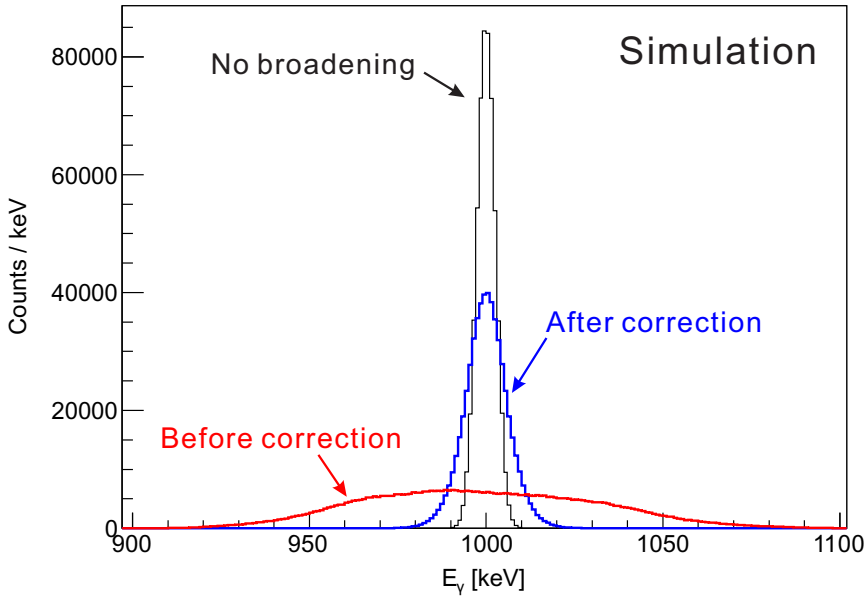

Figure 4.11: Simulated peak shapes for the 1-MeV γ rays. Black line is the peak shape with no Doppler effect. Red and blue lines are the Doppler broadened and the Doppler-shift corrected peak shapes, respectively.

line shows the efficiency when γ ray is uniformly generated in the liquid helium target. The efficiency shown in the red line was smaller than that of the point source shown in the black line. This is because there is an effect of absorption in the target material and an effective solid angle for source position distributing over the target volume is smaller. The dependence of the simulated efficiency on energy was derived from the measured relative efficiency of γ rays from a ^{152}Eu source. The measured relative efficiency was scaled and plotted in Fig. 4.12. Absolute efficiency was not obtained from data with a ^{152}Eu source because of uncertainty in the live time of the data acquisition. To check the absolute efficiency, additional data were taken with a ^{60}Co source and a 2" NaI counter as a γ tagging counter. Absolute value of the simulated efficiency at the energy of 1.17 MeV was compared to the measured efficiency with a ^{60}Co source where angular correlation between the two γ rays from ^{60}Co was taken into account in the simulation. From this comparison, a scaling factor ($\epsilon_{\rm measured}/\epsilon_{\rm simulated}$) of 0.76 was obtained to be applied to the simulated efficiency curve. A less than one scaling factor would be due to idealized geometry and size of Ge crystal in the simulation. In addition, actual mechanical structure of Ge detectors are much simplified in the simulation.

Real efficiency of Hyperball-J is expected to be further reduced by two effects: (1) an in-beam live time of the Ge detectors which was measured to be typically 96% from the analysis of the Ge×LSO triggered data (described in Section 2.7), (2) over-kill due

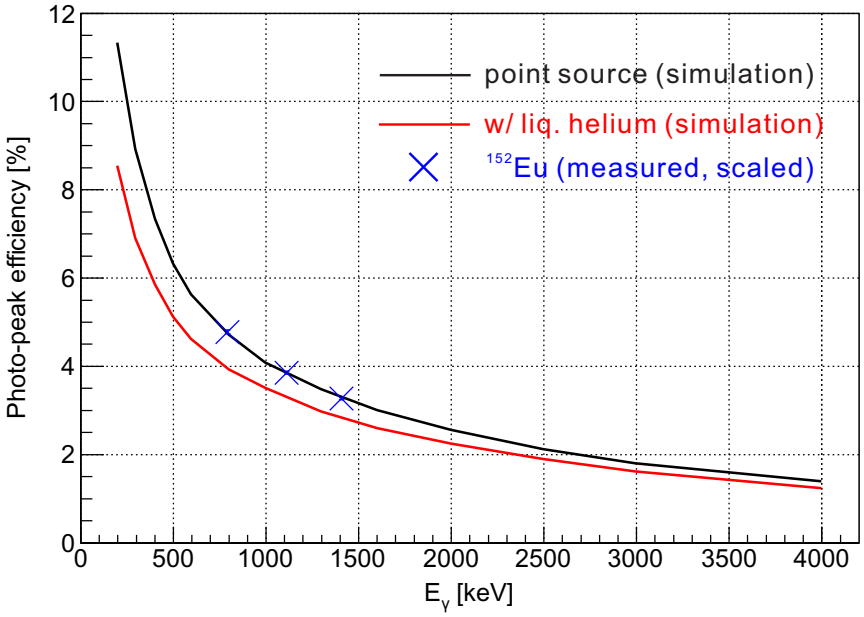

Figure 4.12: Simulated total photo-peak efficiency of Hyperball-J as a function of γ-ray energy. Black line is the efficiency with a point source placed at the center of Hyperball-J, and red line is that with the liquid helium target system and with randomly distributed γ-ray source points. Blue points are measured relative efficiency for γ rays from a ^{152}Eu source.

to the accidental suppression by the PWO counters which was estimated to be of 1%. In total, the actual efficiency of Hyperball-J was estimated to be 95% of the efficiency curve in Fig. 4.12.

Chapter 5

Results

By combining the analysis of the (K^-, π^-) reaction and the Ge detectors, we can identify γ rays from the hypernucleus, ${}^{4}_{\Lambda}$He. The analysis result - the missing mass-gated γ-ray energy spectrum and the observed peak for ${}^{4}_{\Lambda}$He - is described in this chapter.

5.1 Mass selection

Figure 5.1 shows the missing mass spectrum for ${}^{4}_{\Lambda}$He as a function of the excitation energy, $E_{\rm ex}$. The background spectrum associated with materials other than liquid helium as

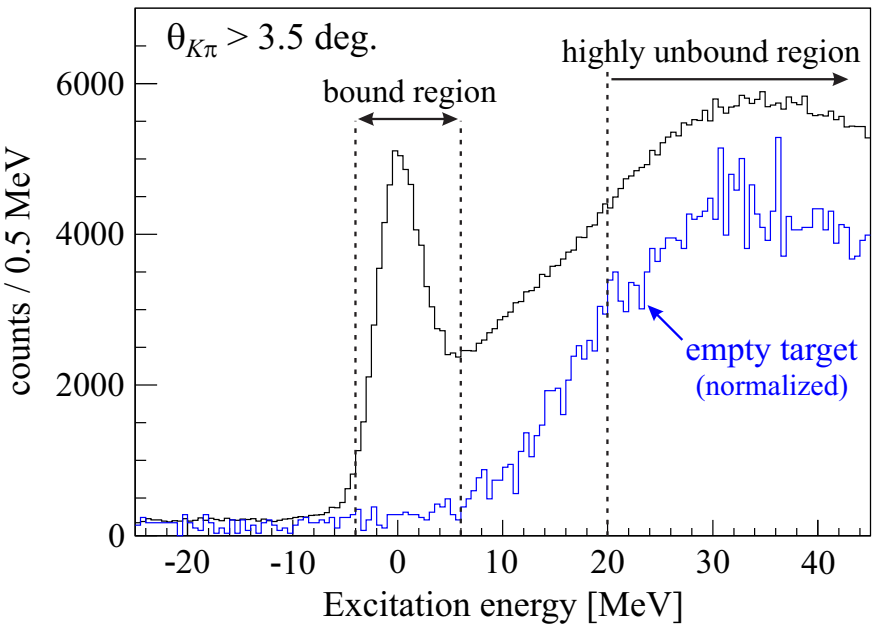

Figure 5.1: The missing mass spectrum for the ^{4}He$(K^-, \pi^-){}^{4}_{\Lambda}$He kinematics plotted as a function of the excitation energy, $E_{\rm ex}$, where events with scattering angles ($\theta_{K\pi}$) larger than 3.5° are selected. Black and blue lines show a spectrum with and without liquid helium, respectively.

well as with K^- beam decay events was obtained from the data with the empty target vessel as shown together in Fig. 5.1. The energy region for a bound ${}^{4}_{\Lambda}$He is $E_{\rm ex} = 0$ – 2.39 MeV, where the Λ binding energy (B_Λ) of 2.39 MeV is taken from emulsion data (see Section 1.5). Therefore, considering the mass resolution of $\sim$5 MeV (FWHM), the region of $-4 < E_{\rm ex} < +6$ MeV was chosen for event selection of the ${}^{4}_{\Lambda}$He bound state that is allowed for γ decay. Events in a highly unbound region were also used to check a background shape in the γ-ray spectrum. The highly unbound region is selected as $E_{\rm ex} > 20$ MeV.

5.2 γ-ray spectra

Figure 5.2 shows mass-gated γ-ray energy spectra. Figure 5.2(a) and (b) are the spectra without and with the Doppler-shift correction, respectively, when the highly unbound region ($E_{\rm ex} > +20$ MeV) of ${}^{4}_{\Lambda}$He is selected. Figure 5.2(c) and (d) are the spectrum without and with the Doppler-shift correction, respectively, for the ${}^{4}_{\Lambda}$He bound region (-4 MeV $< E_{\rm ex} < +6$ MeV).

highly unbound region

In the spectrum (a), we found peaks of γ ray emitted from e^+e^- annihilation (511 keV) and normal nuclei such as ^{76}Ge(564 keV), ^{74}Ge(596 keV), ^{56}Fe(847 keV). These peaks from the normal nuclei are observed because of beam-induced reactions [such as the (n, n') reaction] as well as of an accidental coincidence between the KPI trigger and the γ ray. No γ rays from unknown sources, possibly from hypernuclei, was observed in this spectrum. With the mass gate for the highly unbound region, no γ ray from ${}^{4}_{\Lambda}$He is expected because ${}^{4}_{\Lambda}$He with this excitation energy will emit particles before γ decay. In the spectrum (b), the Doppler-shift correction was applied to (a), and no significant peak structure was found in the energy region of 600 keV $< E_\gamma <$ 2500 keV. The peak of the γ rays from normal nuclei found in (a) was broadened by a unnecessary correction of the Doppler shift. This fact indicates that no peak from any nuclei other than ${}^{4}_{\Lambda}$He appears in the γ-ray energy spectrum after the Doppler-shift correction when the bound mass region is selected.

${}^{4}_{\Lambda}$He bound region

In the spectrum (c), the missing mass gate is applied for the bound region of ${}^{4}_{\Lambda}$He. Observed γ-ray peaks were of e^+e^- annihilation (511 keV) and of normal nuclei with small counts because of the beam-induced reactions and the accidental coincidence. These γ-

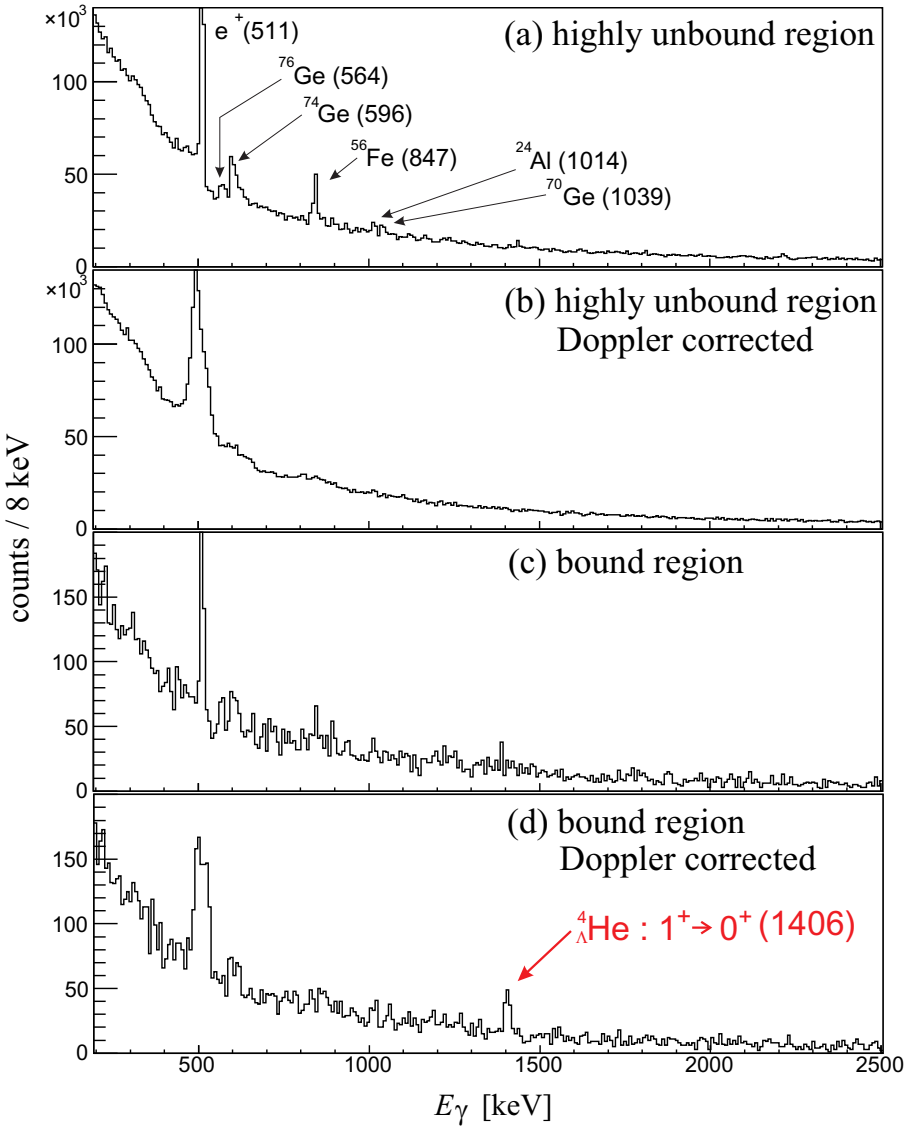

Figure 5.2: γ-ray energy spectra measured by Hyperball-J in coincidence with the ^{4}He(K^-, π^-) reaction. Missing mass selections are applied to the highly unbound region ($E_{\rm ex} > +20$ MeV) for (a) and (b) and to the $^4_\Lambda$He bound region ($-4 < E_{\rm ex} < +6$ MeV) for (c) and (d). An event-by-event Doppler correction is applied for (b) and (d). A single peak observed in (d) is attributed to the $M1(1^+ \to 0^+)$ transition.

ray sources are the same as in the spectrum (a). Only after the event-by-event Doppler-shift correction (the spectrum (d)), the 1406-keV peak is clearly visible.

We tried a peak search in the spectra of the bound region using a peak significance defined as

$$\text{Peak significance} = \frac{\text{peak count}}{1\sigma \text{ error of peak count}},$$

where the peak count was obtained by fitting with a Gaussian function plus a constant

background. The width of the Gaussian function was fixed to the measured resolution (see Section 4.5.2) in the fitting for the spectrum before the Doppler-shift correction. For the spectrum after the Doppler-shift correction, the peak shape was approximated as a Gaussian function having the simulated peak width (see Section 4.5.3). The fitting was attempted at every 2-keV steps of γ-ray energy where the peak position was fixed to a given energy. Figure 5.3 shows results of the peak search in the γ-ray energy spectrum before/after the Doppler-shift correction with the energy range of 600–2500 keV. In the spectrum before the Doppler-shift correction, only one peak at 847 keV was found with a peak significance of more than 3σ, which is the γ-ray from a normal nucleus, ^{56}Fe. In the spectrum after the Doppler-shift correction, the peak at 1406 keV was found with a peak significance of $\sim 7\sigma$. No such peak structure was found with the missing mass gate for the highly unbound region. No other statistically significant peak was obtained in both spectra before/after the Doppler-shift correction.

Therefore, we confirmed that only one γ-ray peak at 1406-keV came from ${}^{4}_{\Lambda}$He.

5.3 1406-keV γ ray

Level assignment

The peak at 1406 keV is assigned to the spin-flip $M1$ transition between the spin-doublet states, ${}^{4}_{\Lambda}\mathrm{He}(1^+ \to 0^+)$. The reasons for this assignment are listed below;

- it is known that ${}^{4}_{\Lambda}\mathrm{He}(1^+)$ is the only bound excited state of ${}^{4}_{\Lambda}$He, and no state other than ${}^{4}_{\Lambda}\mathrm{He}(1^+)$ which emits γ rays is expected to be populated in the selected excitation energy region,

- the peak appears only after the Doppler-shift correction,

- the peak shape is consistent with the peak shape calculated by assuming Doppler-shift effect for the ${}^{4}_{\Lambda}\mathrm{He}(1^+)$ state.

The spin assignments of the ground state $[{}^{4}_{\Lambda}\mathrm{He}(0^+)]$ and the 1st excited state $[{}^{4}_{\Lambda}\mathrm{He}(1^+)]$ were established from the past experiments (see Section 1.3). The ratio of the observed yield of ${}^{4}_{\Lambda}\mathrm{He}(0^+)$ and ${}^{4}_{\Lambda}\mathrm{He}(1^+)$ states in the missing mass spectrum, where the yield of 1^+ state was based on the obtained yield of 1406-keV γ ray (see Section 5.5), is consistent with this spin assignment. A much smaller cross section is expected for the ${}^{4}_{\Lambda}\mathrm{He}(1^+)$ state with the spin-flip Λ production than that for the ${}^{4}_{\Lambda}\mathrm{He}(0^+)$ state with the spin-non-flip Λ production. The comparison of the yields will be described in Section 5.5.

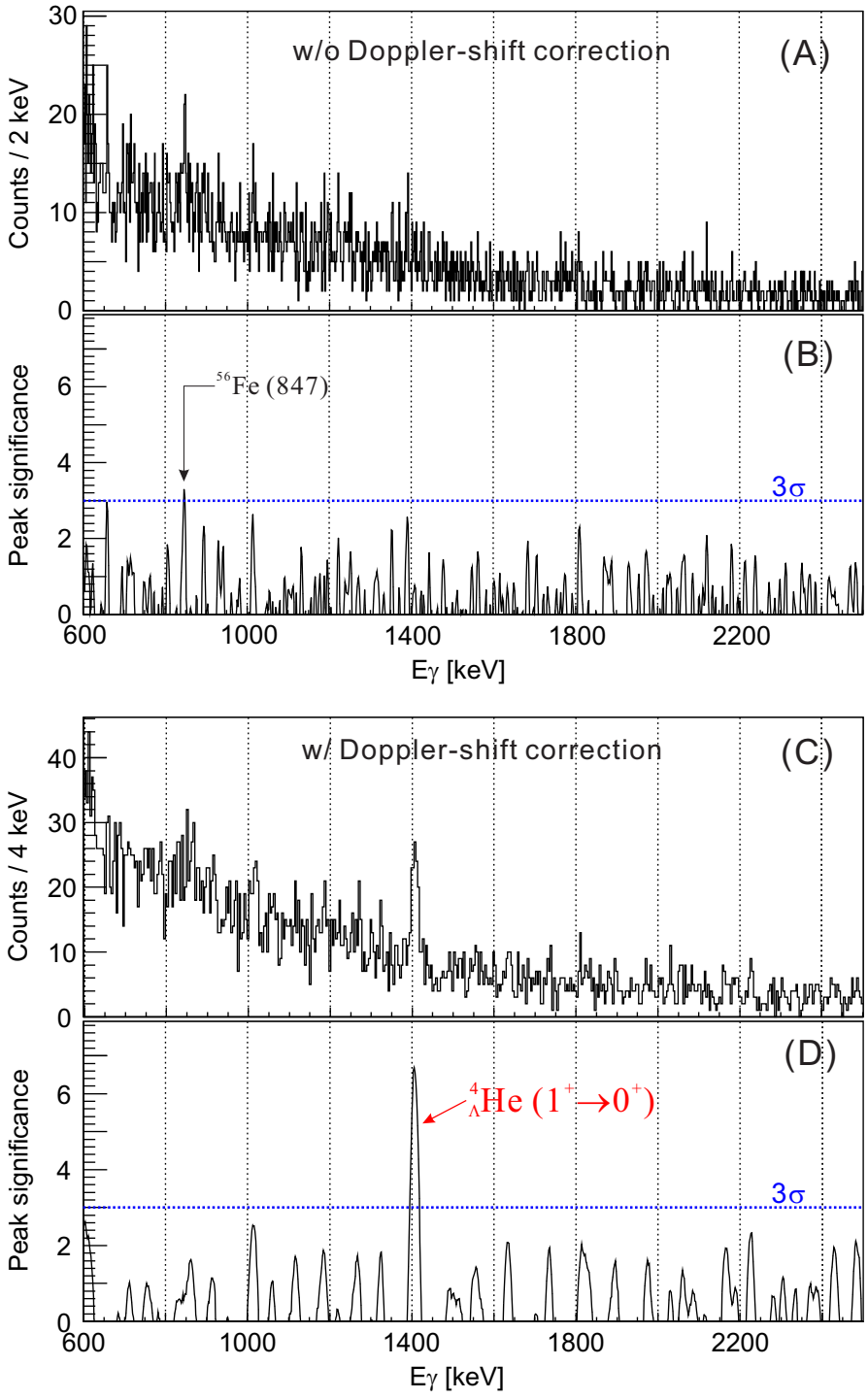

Figure 5.3: A result of the peak search in the γ-ray energy spectrum before/after the Doppler-shift correction: (A) a γ-ray energy spectrum before the Doppler-shift correction selecting a missing mass gate for the $^{4}_{\Lambda}$He bound region, (B) an obtained peak significance as a function of the γ-ray energy, (C) and (D) are those after the Doppler-shift correction.

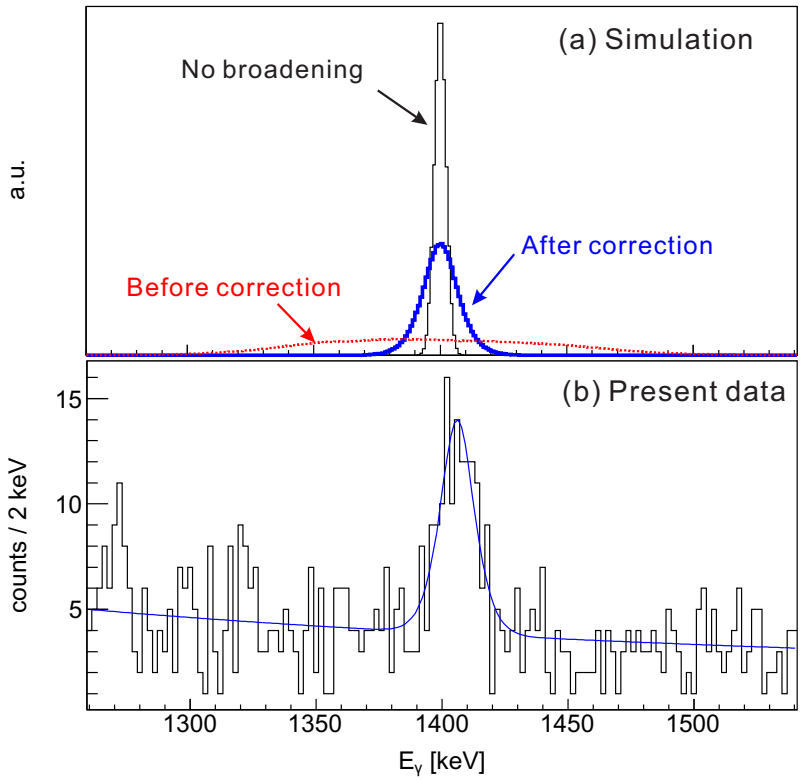

Figure 5.4: (a) Simulated shapes of a 1.4 MeV γ-ray peak. The black line corresponds to a γ ray emitted at rest, the dotted red line to a γ ray emitted from the recoiling ${}^{4}_{\Lambda}$He. The blue line is the result of the Doppler-shift correction applied to the dotted one. (b) shows the fit of the simulated peak shape to the present data.

γ-ray energy

The Doppler-shift-corrected γ-ray energy spectrum with the missing mass gate on the bound region was fitted by using the simulated peak shape assuming the peak energy to be 1.4 MeV (see Section 4.5.3 about the peak shape simulation). Figure 5.4(a) shows simulated γ-ray peak shapes. The thin black line is for a γ ray emitted at rest, the dotted red line for a γ ray emitted immediately after the reaction where ${}^{4}_{\Lambda}$He has a maximum recoil velocity before slowing down in the target material, and the thick blue line for a γ ray with the Doppler-shift correction applied to the dotted red line. The width of the simulated peak shape after the Doppler-shift correction (blue line) is 17 keV (FWHM). The peak fitting result of the Doppler-shift-corrected spectrum is presented in Fig. 5.4(b). In this fitting, the assumed background function was $f_{B.G.}(E_\gamma) = a/\sqrt{E_\gamma - b}$ where a and b are parameters for the fitting. The obtained reduced-χ^2 of the fitting shown in Fig. 5.4(b) was 1.2. We, therefore, concluded that the observed peak shape agrees with a simulated one. This is one of the reasons for assigning the observed γ-ray peak to the

${}^{4}_{\Lambda}\mathrm{He}(1^+ \to 0^+)$ transition.

As a result of the fitting, the γ-ray energy and the yield of the $M1[{}^{4}_{\Lambda}\mathrm{He}(1^+ \to 0^+)]$ transition were determined to be

$$E_\gamma = 1406 \pm 2(\mathrm{stat.}) \pm 2(\mathrm{syst.})\ \mathrm{keV},$$
$$\mathrm{counts} = 94 \pm 13(\mathrm{stat.}),$$

where a dominant source of the systematic error in the measured energy comes from a position inaccuracy of the reaction vertex and of the Ge detectors in correcting the Doppler shift. The systematic error for E_γ will be discussed in the next subsection. The peak significance was

$$\text{Peak significance} = \frac{N_s^{2\sigma}}{\sqrt{N_s^{2\sigma} + N_b^{2\sigma}}} = 7.4\sigma,$$

where $N_s^{2\sigma}$ and $N_b^{2\sigma}$ denote integrated counts over the energy range of $\pm 2\sigma$ of the simulated peak width with the fitting function and that of the background function, respectively.

Systematic error in the measured energy

The sources of the systematic error in the measured energy are listed below:

- accuracy of the energy calibration,
- background function in the fitting,
- simulated Doppler-corrected peak shape,
- inaccuracy in the spatial configuration of the Ge detectors which affects the Doppler-shift correction.

The effects of those sources are described in this section, followed by a summary of a total systematic error at the end.

precision of the energy calibration

We applied energy calibration of the Ge detectors taking into account a gain drift due to the Ge crystal temperature change (see Section 4.3.1). The range of the measured γ-ray energy for the 1406-keV peak before the Doppler-shift correction is 1300–1500 keV as shown in Fig. 5.4(a) (dotted red line). The accuracy of the energy calibration for this energy region is better than ± 0.4 keV as shown in Fig. 4.9.

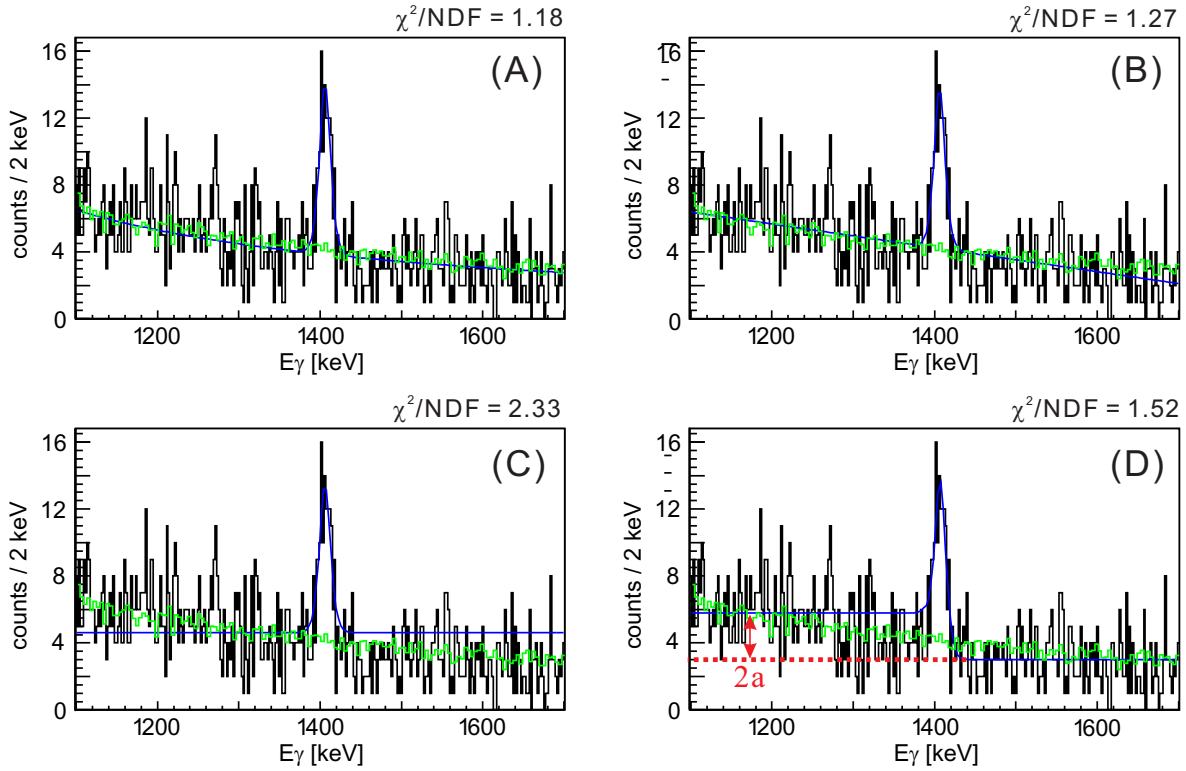

Figure 5.5: Results of the fitting: (A) with the assumed background function, $f_{B.G.}(E_\gamma) = a/\sqrt{E_\gamma - b}$, (B) with a liner background function, (C) with a constant background, (D) with a step background function. The spectrum with the mass gate on the highly unbound region is also plotted in green lines.

background function

We also tried to fit the spectrum after the Doppler-shift correction with various background functions other than the square root function, $f_{B.G.}(E_\gamma) = a/\sqrt{E_\gamma - b}$, such as a constant, a liner function, and a step function ($f_{B.G.}(E_\gamma) = a \cdot \mathrm{erfc}([E_\gamma - E_{center}]/\sqrt{2}\sigma) + b$). In those background functions, a and b are fitting parameters. In the step function, E_{center} and σ are the peak position and the peak width, respectively. The results of the fitting with those background functions are shown in Fig. 5.5 (A–D) and summarized in Table 5.3.1. In the figure, a spectrum with the mass gate on the highly unbound region is also shown in green.

The lowest reduced-χ^2 value of 1.18 was obtained with the square root background function, (A) $f_{B.G.}(E_\gamma) = a/\sqrt{E_\gamma - b}$. This function also agrees with the background shape in the Doppler-corrected spectrum with the mass gate on the highly unbound region. From these two reasons, this background function was used.

With the liner background function (B), a reduced-χ^2 is slightly larger (1.27) than

Table 5.3.1: Results of the fitting with different background functions. a and b denote parameters for the fitting. E_{center} and σ are the peak position and the peak width, respectively.

Background function	Reduced-χ^2	peak position [keV]
(A) $f_{B.G.}(E_\gamma) = a/\sqrt{E_\gamma - b}$ $[a = 2.9(2) \times 10^3, b = 6.5(4) \times 10^2]$	1.18	1406.0(1.2)
(B) $f_{B.G.}(E_\gamma) = aE_\gamma + b$ $[a = -7.1(5) \times 10^{-3}, b = 14.2(7)]$	1.27	1406.1(1.3)
(C) $f_{B.G.}(E_\gamma) = a$(constant) $[a = 4.6(1)]$	2.33	1405.9(1.3)
(D) $f_{B.G.}(E_\gamma) = a \cdot \mathrm{erfc}([E_\gamma - E_{center}]/\sqrt{2}\sigma) + b$ $[a = 1.4(1), b = 3.0(1)]$	1.52	1407.0(1.3)

the square root background function, while it becomes larger (2.33) with the constant background (C). We did not use the constant background because of the larger reduced-χ^2. The liner function (B) can be used to fit the spectrum for the highly unbound region only in the narrow γ-ray energy region.

When the step function [(D) $f_{B.G.}(E_\gamma) = a \cdot \mathrm{erfc}([E_\gamma - E_{center}]/\sqrt{2}\sigma) + b$] was used, the fitting parameter a, which denotes the step height, was 1.4(1). Such a step is expected in the presence of multi Compton scatterings. We simulated an energy deposit distribution in the Ge crystal for the 1.4 MeV γ ray using the Geant4 code [32]. The simulated value of the parameter a is $\sim$0.2, and it is quite different from the fit result. Therefore, we did not use function (D) to fit the background. If the parameter a is fixed to the simulated value, the fitting result is almost the same as the result with the constant function (C).

From these analyses, we concluded that the square root (A) and the line (B) background functions are applicable to the present data, and the systematic error in the peak position among these background functions is estimated to be 0.1 keV. We decided to use the square root function (A) in the analysis for the peak position and the yield because of the lowest reduced-χ^2 value.

simulated peak shape with the Doppler-shift correction

We estimated inaccuracy of the simulated peak shape arising from other factors than the detector geometry, namely, the errors in the estimations of the energy resolution of the Ge detector, in the reaction vertex resolution, and in reconstructing the recoil velocity of ${}^{4}_{\Lambda}$He.

The energy resolution of the Ge detectors after summing up all the data for 1.4-MeV γ ray is 5.13(0.07) keV (FWHM) without Doppler broadening (see Section 4.5.2).

The 1.4% error in this resolution corresponds only to a less than 0.2% change in the simulated peak width after the Doppler-shift correction. This change in the peak width has a negligible effect on its position.

The reaction vertex resolution is 22(2) mm at $\theta_{K\pi}$= 5° (see Section 3.7). The associated error leads to a change of 1.8% in the simulated peak width after the Doppler-shift correction, which again does not have an impact on the peak position.

Accuracy of the recoil velocity of ${}^{4}_{\Lambda}$He depends on three factors: the error in the angular resolution in $\theta_{K\pi}$, and the momentum resolution for the beam K^-. The effect from the error in the angular resolution in $\theta_{K\pi}$ and the momentum resolution for the beam K^- was estimated by the peak shape simulation. The change in the simulated peak width is less than 4%, and the effect of this change on the peak position is also found to be negligibly small.

inaccuracy in the spatial configuration of the detectors

An effect of inaccuracy in the spatial configuration of the Ge detectors respect to the magnetic spectrometer system (= the vertex position) was estimated by the peak shape simulation described in Section 4.5.3. The center position of the simulated peak is shifted by ±1.3 keV with a 5 mm change between the reaction vertex position and the detector position, which is equivalent to the position alignment accuracy of the detector setup. This geometrical uncertainty contributes the most to the systematic error.

over all systematic error in the measured energy

We obtained a total systematic error for the measured γ-ray energy from the systematic errors described above which are listed in Table 5.3.2.

Table 5.3.2: Systematic errors on measured energy position.

Error source	systematic error
precision of the energy calibration	±0.4 keV
background function in the fitting	±0.1 keV
simulated peak shape with the Doppler-shift correction	negligible
inaccuracy in the spatial information of the detectors	±1.3 keV

The systematic error in the measured energy is ±1.8 keV by linearly summing up all of the errors above.

5.4 Excitation energy of ${}^{4}_{\Lambda}\mathrm{He}(1^{+})$

In the present work, a γ-ray energy of the ${}^{4}_{\Lambda}\mathrm{He}(1^{+} \rightarrow 0^{+})$ transition was measured as 1406.0 keV. The transition energy is larger than the measured by an amount of recoil energy of ${}^{4}_{\Lambda}$He. This recoil energy is calculated as $E_{recoil} \cong E^{2}_{measured}/2M_{HYP} = 0.2$ keV where M_{HYP} is the mass of ${}^{4}_{\Lambda}$He. The excitation energy of ${}^{4}_{\Lambda}\mathrm{He}(1^{+})$ was determined as 1406 $\pm$ 2(stat.) $\pm$ 2(syst.) keV, where a small nuclear recoil correction of 0.2 keV does not change the value.

5.5 Ratio of the yield of ${}^{4}_{\Lambda}\mathrm{He}(0^{+})$ and ${}^{4}_{\Lambda}\mathrm{He}(1^{+})$

The ratio of the yield of ${}^{4}_{\Lambda}\mathrm{He}(0^{+})$ and ${}^{4}_{\Lambda}\mathrm{He}(1^{+})$ can be obtained by fitting the missing mass spectrum with additional information for the 1^{+} state (height and peak position relative to 0^{+} state) from the γ-ray analysis.

The γ-ray energy and yield of γ-ray from the 1^{+} state was 1.406$\pm$0.04 MeV and 94$\pm$13 counts, respectively. From this γ-ray yield, we estimated the yield of ${}^{4}_{\Lambda}\mathrm{He}(1^{+})$ in the missing mass spectrum to be $0.33(5) \times 10^{4}$ counts by using the known efficiency of Hyperball-J, 3.1% at 1.4 MeV (see Section 4.5.4). It should be noted that a efficiency loss of 8% due to high energy γs from π^{0} generated by the ${}^{4}_{\Lambda}\mathrm{He} \rightarrow {}^{4}\mathrm{He} + \pi^{0}$ weak decay (BR=52% [45]), which cause electro magnetic shower and lead to an additional energy deposit in Ge detectors and an over suppression with PWO counters, was taken into account for yield estimation.

The yield of ${}^{4}_{\Lambda}\mathrm{He}(0^{+})$ was obtained by fitting the missing mass spectrum with the two Gaussian functions, corresponding to the ${}^{4}_{\Lambda}\mathrm{He}(0^{+})$ [first Gaussian] and ${}^{4}_{\Lambda}\mathrm{He}(1^{+})$ state [second Gaussian]. The fitting parameters are (1) the peak position, (2) the height, and (3) the width of the first Gaussian. The second Gaussian has no free parameters; the height and the relative peak position with respect to the first Gaussian was fixed as 0.33×10^{4} counts and 1.406 MeV, respectively, according to the γ-ray analysis, and the width was common with the first Gaussian. A description of the background function was shown in Section 3.6. Figure 5.6 shows the fit result in the missing mass spectrum for the ${}^{4}\mathrm{He}(K^{-}, \pi^{-}){}^{4}_{\Lambda}\mathrm{He}$ kinematics with the two Gaussian functions. The yield of ${}^{4}_{\Lambda}\mathrm{He}(0^{+})$ and the width were obtained as $4.72(7) \times 10^{4}$ counts and 5.1(1) MeV (FWHM) respectively. The obtained yields in the missing mass spectrum are listed in Table 5.5.1.

The ratio of the yields, $\mathrm{N}[{}^{4}_{\Lambda}\mathrm{He}(1^{+})]/\mathrm{N}[{}^{4}_{\Lambda}\mathrm{He}(0^{+})]$, was found to be 0.07(1) with the scattering angle ($\theta_{K\pi}$) of more than 3.5°. This ratio is one of the reasons for the assignment of the observed γ-ray peak to the $M1$ transition of ${}^{4}_{\Lambda}\mathrm{He}(1^{+} \rightarrow 0^{+})$; a much smaller production cross section is expected for the spin-flip Λ production of the ${}^{4}_{\Lambda}\mathrm{He}(1^{+})$ state

Table 5.5.1: Yield of ${}^{4}_{\Lambda}\mathrm{He}(0^+)$ and ${}^{4}_{\Lambda}\mathrm{He}(1^+)$, obtained by a fitting of the missing mass spectrum with two Gaussian functions. The expected yields based on a DWIA calculation [26]. Only the statistical errors are presented in the obtained values.

	Present data	Calc. [26]
$\mathrm{N}[{}^{4}_{\Lambda}\mathrm{He}(0^+)]$	$4.72 \pm 0.07 \times 10^4$	3.40×10^4
$\mathrm{N}[{}^{4}_{\Lambda}\mathrm{He}(1^+)]$	$0.33 \pm 0.05 \times 10^4$	0.81×10^4
$\mathrm{N}[{}^{4}_{\Lambda}\mathrm{He}(1^+)]/\mathrm{N}[{}^{4}_{\Lambda}\mathrm{He}(0^+)]$	0.07 ± 0.01	0.24

than the spin-non-flip state of ${}^{4}_{\Lambda}\mathrm{He}(0^+)$. As shown in Table 5.5.1, the obtained yields are consistent within a factor of 3 with the expected value based on a DWIA calculation [26], where efficiencies of the detectors, the data-acquisition system, and the analysis of the (K^-, π^-) reaction were roughly taken in account (the total efficiency is 0.4). The obtained ratio of the yields of ${}^{4}_{\Lambda}\mathrm{He}(1^+)/{}^{4}_{\Lambda}\mathrm{He}(0^+)$ is also has a deviation from that of the DWIA calculation. It would be caused by the ambiguity in the quoted elementary spin-flip and spin-non-flip Λ production cross sections which were based on the bubble chamber experiment (see Ref. [58], for example).

Further description of the analysis for the yield and absolute cross sections of ${}^{4}_{\Lambda}\mathrm{He}(0^+)$ and ${}^{4}_{\Lambda}\mathrm{He}(1^+)$ will be reported elsewhere.

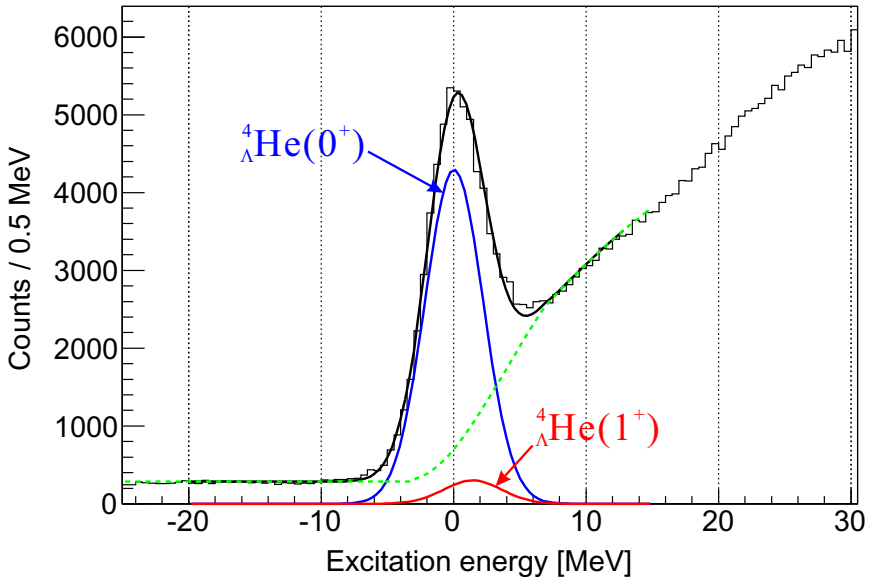

Figure 5.6: Fit result in the missing mass spectrum with two Gaussian function. The relative position respect to the first Gaussian and the height of the second Gaussian are taken from the analysis of the 1406-keV peak.

Chapter 6

Discussion

In the present work, the γ-ray transition of ${}^{4}_{\Lambda}\mathrm{He}(1^{+} \rightarrow 0^{+})$ was unambiguously identified, and the excitation energy of the ${}^{4}_{\Lambda}\mathrm{He}(1^{+})$ state was precisely determined to be $1.406 \pm 0.002 \pm 0.002$ MeV. In this chapter, we will compare the present data with the past γ-ray measurement. We will also discuss theoretical calculations for the charge symmetry breaking effect in the mirror hypernuclei, ${}^{4}_{\Lambda}\mathrm{H}$ and ${}^{4}_{\Lambda}\mathrm{He}$.

6.1 Comparison with the past γ-ray measurement

The comparison between the present and the past experiment for $E_{\mathrm{ex}}({}^{4}_{\Lambda}\mathrm{He}(1^{+}))$ is discussed in this section.

There is only one experiment [14] in the past which reported the γ-ray energy from ${}^{4}_{\Lambda}\mathrm{He}$ (see Appendix A on this experiment) before the present result. It reported the excitation energy of ${}^{4}_{\Lambda}\mathrm{He}(1^{+})$ to be 1.15 ± 0.04 MeV. This energy deviates far from the present value of $1.406 \pm 0.002 \pm 0.002$ MeV beyond errors in these results. Figure 6.1 shows the γ-ray energy spectra of the present and the old experiment: (A) shows the spectrum reported in the previous experiment with stopped K^{-} on ${}^{6}\mathrm{Li}$ and ${}^{7}\mathrm{Li}$ targets by tagging a π^{0} from the ${}^{4}_{\Lambda}\mathrm{He} \rightarrow {}^{4}\mathrm{He} + \pi^{0}$ with a π^{0} kinetic energy selection, (B) is the same as (A), but with a ${}^{6}\mathrm{Li}$ target and a different gate for the kinetic energy, (C) and (D) show the spectra obtained in the present work before/after the Doppler-shift correction.

They claimed that they observed a γ-ray peak from ${}^{4}_{\Lambda}\mathrm{He}$ at the energy of 1.15 ± 0.04 MeV as shown in Fig. 6.1 (A) and (B). However, no such peak structure was found in the spectra of the present work as shown in Fig. 6.1 (C) and (D). Therefore, we concluded that the observed peak in the past experiment, if it really exists, did not belong to ${}^{4}_{\Lambda}\mathrm{He}$. In addition, the statistical significance of less than 3σ for the 1.15-MeV peak is not enough. On the other hand, the γ-ray peak at 1406 keV clearly observed in the present work as shown in Fig. 6.1 (D) is absent in the spectrum (A) and (B).

The present experiment achieved a higher sensitivity because, (1) the hypernucleus

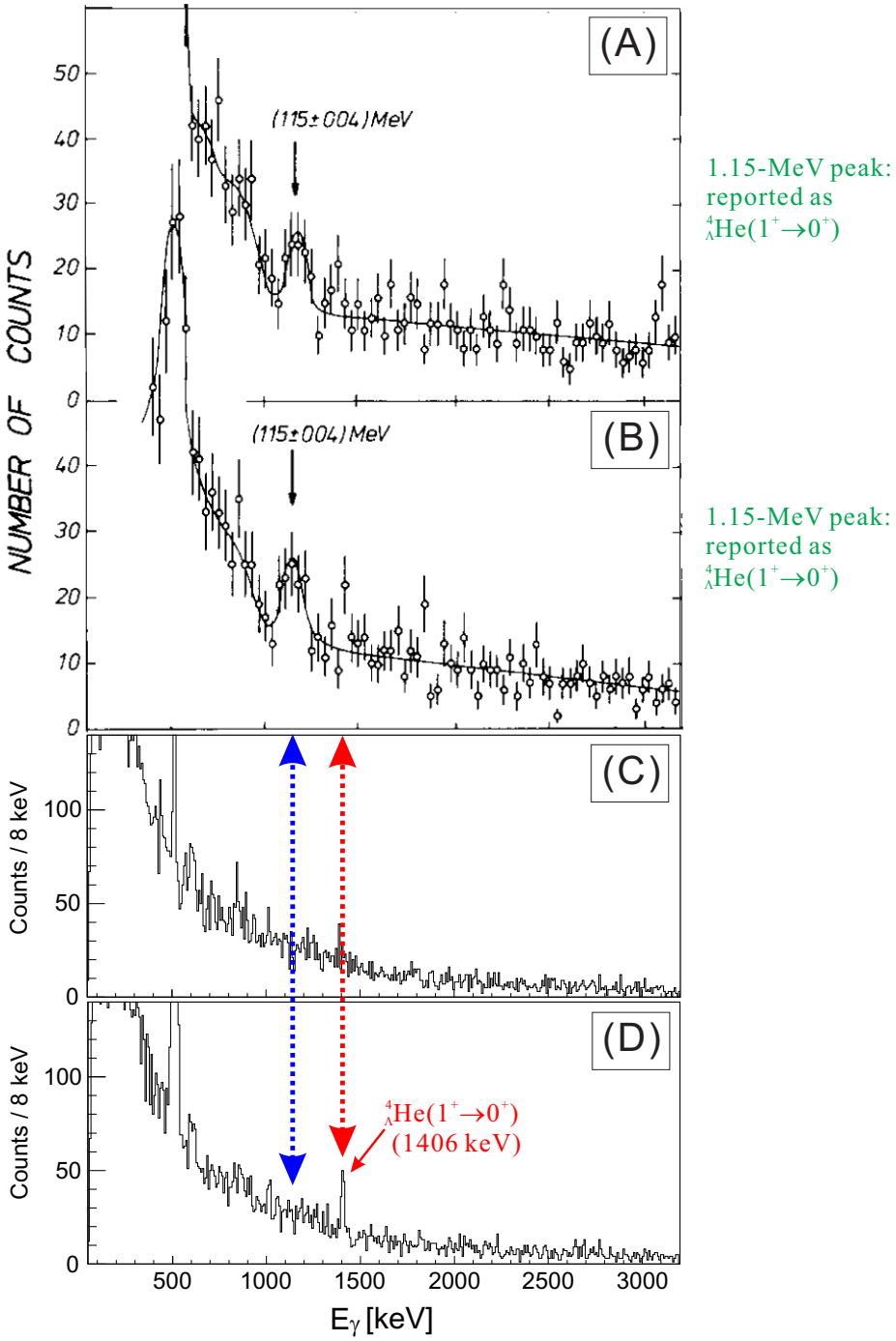

Figure 6.1: γ-ray energy spectra of the present data and the old experiment [14]. (A) the spectrum reported in the previous experiment with stopped K^- on a ^{6}Li and ^{7}Li target tagging a π^0 having a kinetic energy of 45–85 MeV. (B) same as (A), but with a ^{6}Li tagging a π^0 having a kinetic energy of 200–400 MeV. M. Bedjidian *et al.* reported the γ-ray peak from $^4_\Lambda$He at the energy of 1.15 $\pm$ 0.04 MeV [14]. (C) and (d) the spectra before/after the Doppler-shift correction obtained in the present work.

was cleanly tagged by using a direct ${}^{4}_{\Lambda}$He production via the in-flight (K^-, π^-) reaction, (2) we used the Ge detectors with a much better energy resolution (0.5% at 1 MeV (FWHM)) than that of the NaI detectors (12% at 0.98 MeV (FWHM)), (3) we applied the event-by-event Doppler-shift correction combined with the in-flight (K^-, π^-) reaction analysis, which reduces the effect of the Doppler broadening and also supports the γ-ray assignment with the obtained peak shape, and (4) the 1406-keV peak has a statistical peak significance of 7.4σ. The comparison between the present and the past experiment is summarized in Table 1.7.1 and Table 1.7.2.

Updated γ-ray data

Prior to the present work, there were three reports assigning γ rays to ${}^{4}_{\Lambda}$H and one for ${}^{4}_{\Lambda}$He (see the Section 1.6). The averaged excitation energy of ${}^{4}_{\Lambda}$H(1^+) is 1.09 $\pm$0.02 MeV. The result of the present work, $E_{\rm ex}[{}^{4}_{\Lambda}{\rm He}(1^+)]$= 1.406 MeV, supersedes the previously reported energy of $E_{\rm ex}[{}^{4}_{\Lambda}{\rm He}(1^+)]$= 1.15 MeV [14]. The measured γ-ray energies are summarized in Table 6.1.1. Then a difference between these energies, $\Delta E_{\rm ex}$=$E_{\rm ex}[{}^{4}_{\Lambda}{\rm He}(1^+)]-E_{\rm ex}[{}^{4}_{\Lambda}{\rm H}(1^+)]$, is +0.32 $\pm$0.02 MeV.

It is to be noted that two previous experiments using a stopped K^- on ^{6}Li and ^{7}Li targets and NaI detectors had reported hints of unassigned γ-ray peaks at 1.42 $\pm$ 0.02 MeV [25] and 1.45 $\pm$ 0.05 MeV [13], respectively. Taking into account the present result, it is probable that these γ lines are ascribed to the ${}^{4}_{\Lambda}$He$(1^+ \to 0^+)$ transition. Also for ${}^{4}_{\Lambda}$H$(1^+ \to 0^+)$ transition, two previous experiments reported hints of unassigned γ-ray peaks at 1.08 $\pm$ 0.01 MeV [25] and 1.108 $\pm$ 0.010 MeV [59], respectively. These reported γ-ray energy values are consistent with the average value of $E_{\rm ex}({}^{4}_{\Lambda}{\rm H}(1^+))$, respectively. We considered that these unassigned γ-ray peaks support the use of the average value of the three experiments [13, 14, 15] for $E_{\rm ex}({}^{4}_{\Lambda}{\rm H}(1^+))$. A detailed description for these experiments is shown in Appendix A.

Table 6.1.1: Measured γ-ray energies for ${}^{4}_{\Lambda}$H/${}^{4}_{\Lambda}$He. Unit is in MeV.

	${}^{4}_{\Lambda}{\rm H}(1^+ \to 0^+)$	${}^{4}_{\Lambda}{\rm He}(1^+ \to 0^+)$
M. Bedjidian *et al.* (1976) [13]	1.09 $\pm$0.03	-
M. Bedjidian *et al.* (1979) [14]	1.04 $\pm$0.04	(1.15 $\pm$0.04)
A. Kawachi (1997) [15]	1.114 $\pm$0.030	-
Present experiment	-	1.406 $\pm$0.004
Average energy	1.09 $\pm$0.02	1.406 $\pm$0.004

6.2 Level scheme of ${}^{4}_{\Lambda}$H/${}^{4}_{\Lambda}$He

Based on the present result, we updated the level scheme of ${}^{4}_{\Lambda}$He. Figure 6.2 shows the updated level schemes of the mirror hypernuclei, ${}^{4}_{\Lambda}$H and ${}^{4}_{\Lambda}$He, where only the assigned γ-ray data are used to obtain the excitation energies.

By combining the emulsion data of $B_\Lambda({}^{4}_{\Lambda}\mathrm{He}(0^+))$=2.39 ±0.03 MeV, the present result gives $B_\Lambda({}^{4}_{\Lambda}\mathrm{He}(1^+))$= 0.98 ± 0.03 MeV, where the error in $B_\Lambda({}^{4}_{\Lambda}\mathrm{He}(1^+))$ of 0.03 MeV is

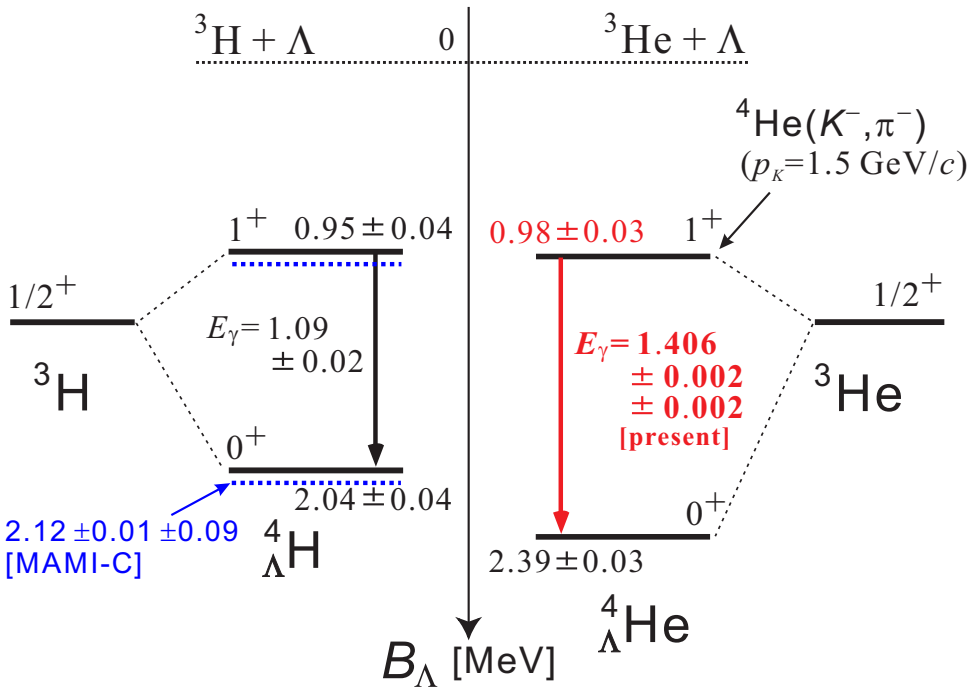

Figure 6.2: Updated level schemes of the mirror hypernuclei, ${}^{4}_{\Lambda}$H and ${}^{4}_{\Lambda}$He. Λ binding energies (B_Λ) of ${}^{4}_{\Lambda}$H(0^+) and ${}^{4}_{\Lambda}$He(0^+) are taken from the past emulsion experiments [9]. $B_\Lambda({}^{4}_{\Lambda}\mathrm{He}(1^+))$ and $B_\Lambda({}^{4}_{\Lambda}\mathrm{H}(1^+))$ are obtained using the present and past γ-ray data [13, 14, 15], respectively. Recently, $B_\Lambda({}^{4}_{\Lambda}\mathrm{H}(0^+))$ = 2.12 ± 0.01 (stat.) ± 0.09 (syst.) MeV was obtained with an independent technique [16].

Table 6.1.2: Measured Λ binding energies (B_Λ) of ${}^{4}_{\Lambda}$H/${}^{4}_{\Lambda}$He. Unit is in MeV.

	Ground state (0^+)	1st-excited state (1^+)
${}^{4}_{\Lambda}$He	2.39 ±0.03	0.98 ±0.03
with emulsion data		
${}^{4}_{\Lambda}$H	2.04 ±0.04	0.95 ±0.04
$\Delta B_\Lambda[{}^{4}_{\Lambda}\mathrm{He}-{}^{4}_{\Lambda}\mathrm{H}]$	+0.35 ±0.05	+0.03 ±0.05
with MAMI-C data		
${}^{4}_{\Lambda}$H	2.12 ±0.10	1.03 ±0.10
$\Delta B_\Lambda[{}^{4}_{\Lambda}\mathrm{He}-{}^{4}_{\Lambda}\mathrm{H}]$	+0.27 ±0.11	−0.05 ±0.11

carried over from the error in $B_\Lambda({}^{4}_{\Lambda}\mathrm{He}(0^+))$ measured by the emulsion experiments. The measured B_Λ values of 0^+ and 1^+ states for the mirror hypernuclei, ${}^{4}_{\Lambda}$H and ${}^{4}_{\Lambda}$He, are summarized in Table 6.1.2.

6.3 CSB effect in ${}^{4}_{\Lambda}$H/${}^{4}_{\Lambda}$He

The present result provides a solid experimental evidence for existence of a large CSB effect in ΛN interaction. Our new findings are summarized below:

Existence of the CSB effect

The excitation energy of ${}^{4}_{\Lambda}\mathrm{He}(1^+)$ (1.406 $\pm$0.004 MeV) obtained in the present work is largely different from ${}^{4}_{\Lambda}\mathrm{H}(1^+)$ (1.09 $\pm$0.02 MeV); the difference amounts to ΔE_{ex}=+0.32 $\pm$ 0.02 MeV (see Section 6.2), which is larger than +0.06 $\pm$0.05 MeV reported in the past experiment [14]. Therefore, the existence of the CSB effect in ΛN interaction has been definitely confirmed via γ-ray data alone.

Strong spin-dependence of the CSB effect

The differences in B_Λ values between ${}^{4}_{\Lambda}$H and ${}^{4}_{\Lambda}$He are summarized in Table 6.1.2. By comparing $B_\Lambda({}^{4}_{\Lambda}\mathrm{He}(1^+)) = 0.98 \pm 0.03$ MeV and $B_\Lambda({}^{4}_{\Lambda}\mathrm{H}(1^+)) = 0.95 \pm 0.04$ MeV, obtained from the emulsion data of $B_\Lambda(0^+)$ as well as the γ-ray data, the difference in $B_\Lambda(1^+)$ is $\Delta B_\Lambda(1^+) = B_\Lambda({}^{4}_{\Lambda}\mathrm{He}(1^+)) - B_\Lambda({}^{4}_{\Lambda}\mathrm{H}(1^+)) = +0.03 \pm 0.05$ MeV, while the difference in $B_\Lambda(0^+)$ is $\Delta B_\Lambda(0^+) = +0.35 \pm 0.05$ MeV. If the result of MAMI-C is used for $B_\Lambda({}^{4}_{\Lambda}\mathrm{H}(0^+))$, these differences will become as $\Delta B_\Lambda(1^+) = -0.05 \pm 0.11$ MeV and $\Delta B_\Lambda(0^+) = +0.27 \pm 0.11$ MeV. These values are the same within the errors between the emulsion and the MAMI-C data.

Thus, the CSB effect is found to be strongly spin dependent, being vanishingly small in the 1^+ state and significantly large in the 0^+ state. This demonstrates that the underlying ΛN CSB interaction has spin dependence. Even if the reported $B_\Lambda(0^+)$ value in ${}^{4}_{\Lambda}$H or ${}^{4}_{\Lambda}$He has a systematic shift, it is clear that the 0^+ state receives a different energy shift from the CSB effect than the 1^+ state, by taking account of the 320 keV difference in $E_{\mathrm{ex}}(1^+)$ obtained from γ-ray data, indicating the strong spin dependence of the CSB effect.

6.4 Theoretical calculations for the CSB effect

The present findings, the confirmation of the CSB effect in ΛN interaction and its spin dependence, would give novel constraints to baryon-baryon interaction models such as

widely accepted Nijimegen-soft-core models [60, 61, 62].

The Nijimegen group constructed interaction models called "model-D" and "model-F" based on one boson exchange picture [60], which are described in terms of pseudoscaler-, vector-, and scaler-meson exchanges. The free parameters, such as coupling constants and F/D ratios, were obtained from wealthy and precise NN scattering data and also limited YN scattering data. These interaction models succeeded in reproducing B_Λ values in hypernuclei, while the use of "hard-core" potentials with the infinite height near the core region was thought to be unrealistic. Then they constructed interaction models with "soft-core" pictures. The first version of the soft-core model (NSC89) [61] failed to explain the spin-spin part of ΛN interaction which appears in hypernuclear spin-doublet energy spacing. The Nijimegen group, then, proposed an improved version of the soft-core model (NSC97 $a \sim f$) with various parameter set [62], in which the spin-spin part of ΛN interaction changes continuously from a to f, but all of them give a good fit to the two-body scattering data. It means that constraints for the interaction model from the existing scattering data is insufficient, and therefore, feedback from hypernuclear data is required.

In this section, firstly, we describe of three-body $\Lambda N - \Sigma N$ mixing force, which we conjecture is possibly an origin of the spin dependent CSB effect. Then, the comparisons between the updated experimental data and theoretical calculations considering $\Lambda N - \Sigma N$ mixing force are discussed in this section, which may gives feedback to interaction models.

Three-body $\Lambda N - \Sigma N$ mixing force

We found a large spin dependence of CSB effect in the mirror hypernuclei, ${}^{4}_{\Lambda}\mathrm{H}/{}^{4}_{\Lambda}\mathrm{He}$; there is a large effect in the 0^+ state but a small effect in the 1^+ state. We conjecture that Σ mixing in Λ hypernuclei is mainly responsible for the CSB effect because theoretical calculations [8, 63] show that the $\Lambda\Sigma$ mixing effect via ΛNN three-body force as shown in Fig. 6.3 (top right) gives rise to a one order of magnitude smaller energy shift in the 1^+ state than the 0^+ state.

Y. Akaishi claimed that ΛNN three-body force plays an important role to reproduce B_Λ values of s-shell hypernuclei [8]. Figure 6.3 shows the calculated level scheme of ${}^{4}_{\Lambda}\mathrm{He}$ where effects of the ΛNN three-body force are presented. He explained that two-body ΛN-ΣN coupling interaction contributes as

$$\begin{aligned} &(3/2)V^{T}_{\Lambda\Sigma N} - (1/2)V^{S}_{\Lambda\Sigma N} \quad (\text{for } {}^{4}_{\Lambda}\mathrm{H}/{}^{4}_{\Lambda}\mathrm{He}(0^+) \text{ state}) \\ &(1/2)V^{T}_{\Lambda\Sigma N} + (1/2)V^{S}_{\Lambda\Sigma N} \quad (\text{for } {}^{4}_{\Lambda}\mathrm{H}/{}^{4}_{\Lambda}\mathrm{He}(1^+) \text{ state}) \end{aligned}$$

where $V^{T}_{\Lambda\Sigma N}$ and $V^{S}_{\Lambda\Sigma N}$ denote ΛN-ΣN coupling potentials in the spin-triplet and singlet

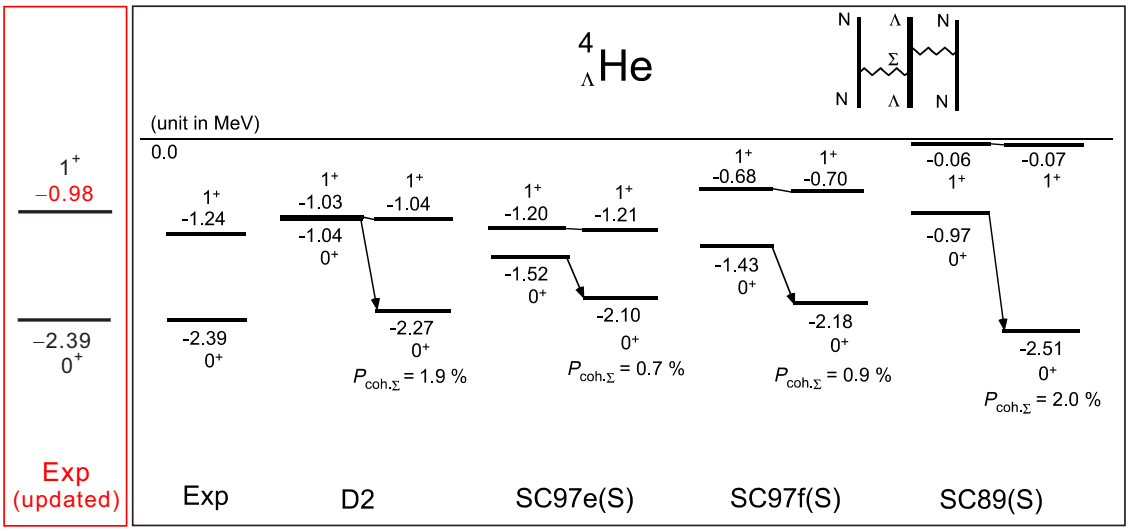

Figure 6.3: Calculated level scheme of $^{4}_{\Lambda}$He reported by Y. Akaishi [8] shown together with the present experimental result (left). The level shifts shown in the arrow are due to dominant effects of the ΛNN three-body force through the ΛN-ΣN mixing as shown in the top right.

state of the hyperon-nucleon system. Because the ΛN-ΣN coupling interaction is much stronger in the spin-triplet channel according to the Nijimegen interaction models, it is claimed that the contribution of the ΛNN three-body force appears about one order, $9 = [(3/2)/(1/2)]^2$, of magnitude larger in the 0^+ state than the 1^+ state. They reported that the $(1^+, 0^+)$ energy spacing comes from the contribution of ΛNN three-body force as well as ΛN spin-spin interaction in the Nimegen soft-core potential. A similar contribution of ΛNN three-body force was also seen with their simple potential ("D2 potential") which has only the central parts instead of the tensor part for both ΛN and ΣN channels. These results indicate importance of ΛN-ΣN mixing force for understanding the s-shell hypernuclear system.

The effect of ΛNN three-body force on the CSB effect in A=4 hypernuclear system was discussed by E. Hiyama [63], A. Nogga [21], and A. Gal [64] as described in the followings.

Few-body calculation with the ΛNN three-body force

E. Hiyama studied the effect of the ΛNN three-body force by performing an exact four-body calculation [63]. It was reported that an effect of the $NN\Lambda$ three-body force causes a larger energy shift in the 0^+ state than the 1^+ state, which is the same trend as the Akaishi's report [8]. The calculation showed that the Coulomb effect including Σ makes a small CSB effect (-0.05 MeV). Other possible origins of the CSB effect were not taken

Table 6.4.1: Comparison between the four-body calculation by A. Nogga [21] (calc. I: with the NSC97*e* interaction model, calc II: with the NSC89 model) and the experimental data. ΔB_Λ denotes the difference in B_Λ, $\Delta B_\Lambda = B_\Lambda({}^4_\Lambda\mathrm{He}) - B_\Lambda({}^4_\Lambda\mathrm{H})$. Unit is in MeV.

	exp. data (old)	(updated)	calc.I NSC97*e*	calc.II NSC89
Λ binging energy				
$B_\Lambda({}^4_\Lambda\mathrm{H}(0^+))$	2.04 ±0.04		1.47	1.80
$B_\Lambda({}^4_\Lambda\mathrm{H}(1^+))$	0.95 ±0.04		0.73	
$B_\Lambda({}^4_\Lambda\mathrm{He}(0^+))$	2.39 ±0.03		1.54	2.14
$B_\Lambda({}^4_\Lambda\mathrm{He}(1^+))$	1.24 ±0.05	0.98 ±0.03	0.72	
excitation energy				
$E_{\mathrm{ex}}({}^4_\Lambda\mathrm{H}(1^+))$	1.09 ±0.02		0.74	
$E_{\mathrm{ex}}({}^4_\Lambda\mathrm{He}(1^+))$	1.15 ±0.04	1.406 ±0.004	0.82	2.06
ΔB_Λ				
$\Delta B_\Lambda(0^+)$	+0.35 ±0.05		0.07	0.34
(with MAMI data)	+0.27 ±0.11			
$\Delta B_\Lambda(1^+)$	+0.29 ±0.05	+0.03 ±0.05	−0.01	
(with MAMI data)	+0.21 ±0.11	−0.05 ±0.11		

into account in this calculation.

In contrast to the previous calculation, A. Nogga reported results of a four-body $YNNN$ coupled-channel calculation using NSC97*e*, where the CSB in the YN interactions as well as the mass difference of Σ was taken into account [21] (see Section 1.4 for a description of the calculation). Comparison with the updated experimental data is summarized in Table 6.4.1. The experimental result of a small difference in the $B_\Lambda(1^+)$, $\Delta B_\Lambda(1^+) = +0.03 \pm 0.05$ MeV, was reproduced by the calculation with the NSC97*e* interaction model, remaining large disagreement in $\Delta B_\Lambda(0^+)$. The calculation with the NSC89 interaction model accounted for a sizable CSB difference in $B_\Lambda(0^+)$ [$\Delta B_\Lambda(0^+) =$ 0.34 MeV], but the difference in $E_{\mathrm{ex}}({}^4_\Lambda\mathrm{He}(1^+))$ from the experimental data is large (0.65 MeV). The calculations based on the Nijimagen interaction models have yet explained the measured CSB effects.

Shell-model calculation with a central $\Lambda N - \Sigma N$ mixing force

Recently, A. Gal estimated the CSB effect [64] using the central-force ΛN-ΣN interaction ("D2 potential" in the Akaishi's paper [8], namely "$\Lambda\Sigma_{e \text{ or } f}$"), in contrast to the widely-used tensor-force dominated ΛN-ΣN interaction in NSC97*e* or *f*. It is noted that D.J. Millener also used "D2 potential" for calculations of *p*-shell hypernuclear structures (see Ref. [7], for example) which shows good agreement with γ-ray data. The comparison between the calculation and the experimental data is summarized in Table 6.4.2. Two

Table 6.4.2: Comparison between the shell model calculation by A. Gal [64] and the experimental data. Each contribution on B_Λ difference was defined as $\Delta B_\Lambda = B_\Lambda(^4_\Lambda\mathrm{He}) - B_\Lambda(^4_\Lambda\mathrm{H})$. Unit is in keV.

model	$\Delta T_{YN}(0^+)$	$\Delta V_C(0^+)$	$\Delta V_{YN}(0^+)$	$\Delta B_\Lambda(0^+)$	$\Delta B_\Lambda(1^+)$
NSC97e	47	−16	44	75	−10
NSC97f				100	−10
$\Lambda\Sigma_e$	39	−45	232	226	30
$\Lambda\Sigma_f$	49	−46	263	266	39
exp. data (emulsion)				350 ±50	30 ±50
exp. data (MAMI)				270 ±110	−50 ±110

contributions, an asymmetric kinetic energy contribution due to a ΣN intermediate-state mass difference (ΔT_{YN}) and a contribution from Coulomb energy modification induced by hyperons (ΔV_C), both being <50 keV, cancel out and do not seem to be a source of the observed CSB effect (∼300 keV). CSB one-pion-exchange contribution with a $\Lambda\Lambda\pi$ coupling [20], which arises from Λ-Σ^0 mixing, was taken into account in his calculation. This contribution on the energy (ΔV_{YN}) with the "$\Lambda\Sigma_{e \text{ or } f}$" potential was found to be sizable (>200 keV) for reproducing the existing data, while the NSC97 model gives a small ΔV_{YN}. It was mentioned that the origin of such a large contribution is a $\Lambda\Sigma$ central part in the selected potential, while the $^3S_1$-$^3D_1$ tensor part is dominant in the NSC97 model.

His ΔB_Λ values show a good agreement with the experimental data. This fact implies that the tensor-dominated strong $\Lambda\Sigma$ coupling in the widely accepted NSC97 model has to be reconsidered. In addition, this result suggests that the Λ-Σ mixing force can be a source of the CSB effect observed in the A=4 hypernuclear systems.

ab initio calculation with the interaction from chiral effective field theory

In contrast to the calculations based on Nijimegen one boson exchange models described above, D. Gazda and A. Gal studied the CSB effect using the Bonn-Jülich leading-order (LO) chiral effective field theory hyperon-nucleon potential (reported in 2006) [65] via a four-body *ab initio* calculation [66]. The LO Bonn-Jülich interaction model was based on one pseudoscaler-meson exchanges and four-baryon contact terms, in which free parameters were determined from NN and YN scattering data as in the case of the Nijimegen interaction models. A charge symmetry breaking $\Lambda - \Sigma^0$ mixing vertex was additionally taken into account in the calculation. The results of their calculation and the experimental data are summarized in Table 6.4.3. Obtained values are close to the experimental data, while there is a large dependence of the cutoff momentum parameter in the interaction model. They claimed that the origin of this large CSB splitting in

Table 6.4.3: Comparison between the experimental data and the *ab initio* calculation by D. Gazda [66], which is made with a cutoff parameter range of 600–650 MeV. Unit is in MeV.

	exp. data	calc. [66]
Λ binging energy of ${}^{4}_{\Lambda}$He		
$B_\Lambda({}^{4}_{\Lambda}\mathrm{He}(0^+))$	2.39 $\pm$0.03	2.444 – 2.365
$B_\Lambda({}^{4}_{\Lambda}\mathrm{He}(1^+))$	0.98 $\pm$0.03	0.683 – 1.166
excitation energy of ${}^{4}_{\Lambda}$H/${}^{4}_{\Lambda}$He		
$E_{\mathrm{ex}}({}^{4}_{\Lambda}\mathrm{H}(1^+))$	1.09 $\pm$0.02	0.95 – 1.09
$E_{\mathrm{ex}}({}^{4}_{\Lambda}\mathrm{He}(1^+))$	1.406 $\pm$0.04	1.28 – 1.56
$\Delta B_\Lambda = B_\Lambda({}^{4}_{\Lambda}\mathrm{He}) - B_\Lambda({}^{4}_{\Lambda}\mathrm{H})$		
$\Delta B_\Lambda(0^+)$	+0.35 $\pm$0.05	+0.14 – +0.24
(with MAMI data)	+0.27 $\pm$0.11	
$\Delta B_\Lambda(1^+)$	+0.03 $\pm$0.05	-0.23 – -0.19
(with MAMI data)	-0.05 $\pm$0.11	

the excitation energy (ΔE_{ex}) is a dominant spin-singlet ΛN-ΣN coupling contact term in the Bonn-Jülich interaction model combined with the CSB $\Lambda - \Sigma^0$ mixing term. It is not the case in widely-accepted NSC97 potential having a dominant ${}^3S_1$-${}^3D_1$ tensor component. The same argument was given in Ref. [64], while there exists a difference in the contribution of the CSB effect on $\Delta B_\Lambda(1^+)$; -200 keV in this calculation and +40 keV in the previous calculation [64]. It is noted that the few-body calculation reported by E. Hiyama also shows repulsive contribution from the three-body ΛNN interaction in the 1^+ state [63].

However, the calculated differences in B_Λ, $\Delta B_\Lambda(0^+) = B_\Lambda({}^{4}_{\Lambda}\mathrm{He}(0^+)) - B_\Lambda({}^{4}_{\Lambda}\mathrm{H}(0^+))$ =+0.14–+0.24 MeV and $\Delta B_\Lambda(1^+) = -0.23$–$-0.19$ MeV, do not agree with the experimental data, while B_Λ values of ${}^{4}_{\Lambda}$He are reproduced and the dependence of the cutoff parameter on $\Delta B_\Lambda(1^+)$ seems to be small. This calculation gives a $B_\Lambda({}^{4}_{\Lambda}\mathrm{H}(0^+))$ value shifted by +0.2 MeV from the emulsion data, but this shift is larger than the reported experimental error. It is conjectured that a systematic energy shift of 0.2 MeV exists in the measured $B_\Lambda(0^+)$ based on the emulsion data.

6.5 Present status of the study of CSB in A=4 hypernuclear system

The confirmation of the CSB effect in the A=4 hypernuclear system found in the present work indicates the existence of the CSB effect in ΛN interaction. Theoretical studies suggest importance of ΛN-ΣN mixing contribution for understanding the CSB effect. The strong spin-dependence of the CSB effect found in the present work may support this

suggestion. However, the widely accepted interaction model, NSC97, failed to reproduce the experimental data for A=4 mirror hypernuclei. Resent studies claimed that NSC97 interaction model has to be reconsidered in terms of ΛN-ΣN interaction; the central part seems to be important for CSB effect while the tensor part is dominant in NSC97 interaction model.

Experimentally, the excitation energies of the ${}^{4}_{\Lambda}\mathrm{He}(1^+)$ was accurately determined by the present work. On the other hand, although the excitation energy of ${}^{4}_{\Lambda}\mathrm{H}(1^+)$ is rather well determined by the past experiments using NaI detectors, re-examination of this energy using Ge detectors with a much better energy resolution is desirable for experimental completeness for study of the CSB effect in A=4 hypernuclei. We are, therefore, now proposing a new γ-ray spectroscopic experiment at J-PARC to measure the excitation energy of ${}^{4}_{\Lambda}\mathrm{H}(1^+)$ [67]. If the experiment is carried out, the excitation energies of ${}^{4}_{\Lambda}\mathrm{H}(1^+)/{}^{4}_{\Lambda}\mathrm{He}(1^+)$ would be completely re-examined with modern techniques.

For $B_\Lambda(0^+)$ values, it is thought that the measured $B_\Lambda(0^+)$ values based on the emulsion data have a systematic shift. Recently, an experiment at MAMI re-examined the $B_\Lambda(\mathrm{H}(0^+))$ value via precise decay π^- spectroscopy and reported a consistent $B_\Lambda(0^+)$ value with the emulsion data [16]. In this experiment, there is a chance to reduce the reported systematic error of ± 0.09 MeV. The reduction of the systematic error may help to improve experimental data for study of the CSB effect. On the other hand, it is difficult to re-examine the $B_\Lambda(\mathrm{He}(0^+))$ value with precision of better than 0.1 MeV with a technique other than emulsion. A discovery of a new method for measuring $B_\Lambda(\mathrm{He}(0^+))$ value is necessary to complete experimental data for the CSB effect in ΛN interaction.

It is noted that the large deviations in the calculated CSB effect among the interaction models, such as Nijimegen model and Bonn-Jülich model, would be caused by the lack of YN scattering data. The existing data of YN scattering were obtained via bubble chamber experiments in 1960s (see references in [68]). More precise YN scattering data with modern techniques may help for study of the CSB effect and understanding of baryon-baryon interaction. Actually, a Σp scattering experiment will be performed at J-PARC with a newly developed scintillating fiber tracking device [69].

We hope that our new result (and also precise measurements in future) may promote further theoretical and experimental studies not only for the origin of the CSB effect but also for the properties of Λ-Σ mixing in hypernuclei.

Chapter 7

Summary

We performed a γ-ray spectroscopic experiment of ${}^{4}_{\Lambda}$He (J-PARC E13) at the J-PARC K1.8 beam line to examine the existence of the Charge Symmetry Breaking (CSB) effect in the mirror hypernuclei, ${}^{4}_{\Lambda}$H and ${}^{4}_{\Lambda}$He [23, 24]. The CSB effects were previously reported by the past experiments; there are (1) difference between the Λ binding energies (B_Λ) of ${}^{4}_{\Lambda}$H(0^+) and ${}^{4}_{\Lambda}$He(0^+) and (2) difference between the excitation energies of ${}^{4}_{\Lambda}$H(1^+) and ${}^{4}_{\Lambda}$He(1^+). The reported excitation energy of ${}^{4}_{\Lambda}$He(1^+) was 1.15 $\pm$0.04 MeV [14]. These differences indicate a large CSB effect in ΛN interaction if the data are confirmed. However, experimental re-examinations by independent and modern techniques with higher sensitivity have been awaited for the confirmation. A break-through has been brought by our γ-ray spectroscopic experiment of ${}^{4}_{\Lambda}$He; we has measured the transition energy between the Λ-spin doublet states ($1^+, 0^+$) using germanium (Ge) detectors with a much better energy resolution of 5 keV (FWHM) for 1 MeV γ ray.

The hypernucleus ${}^{4}_{\Lambda}$He was produced via the (K^-, π^-) reaction with a beam momentum of $p_K = 1.52$ GeV/c. The hypernuclear production was tagged by measuring the missing mass of the ^{4}He$(K^-, \pi^-)X$ reaction, where the beam K^- and the scattered π^- were particle identified and momentum analyzed by the beam line spectrometer and the superconducting dipole magnet (SKS) with a modified detector configuration for γ-ray spectroscopy (SksMinus), respectively. The signal-to-noise ratio in the missing mass as well as the γ-ray energy spectrum was drastically improved by employing a beam K^- decay suppression counter (SMF). In addition, γ rays from the produced hypernucleus were detected by a large solid-angle Ge detector array (Hyperball-J), in coincidence with the (K^-, π^-) reaction. The event-by-event Doppler-shift correction was necessary because the lifetime of the ${}^{4}_{\Lambda}$He(1^+) state is expected to be much shorter than the stopping time of the recoiling hypernucleus, and thus the measured γ-ray peak was subject to Doppler broadening.

From the analysis of the present data, we clearly identified a γ-ray transition from ${}^{4}_{\Lambda}$He after the Doppler-shift correction and determined the energy spacing between the

spin-doublet states $(1^+, 0^+)$ to be 1406 $\pm$ 2 (stat.) $\pm$ 2 (syst.) keV. The result of the present data superseded the claim of the previous experiment (1.15 MeV) and established the level scheme of ${}^{4}_{\Lambda}$He. The Λ binding energy of the excited state was obtained to be $B_\Lambda({}^{4}_{\Lambda}\mathrm{He}(1^+)) = 0.98 \pm 0.03$ MeV by combining with the emulsion data of $B_\Lambda(0^+)$.

The difference between the excitation energy of ${}^{4}_{\Lambda}\mathrm{He}(1^+)$ [1.406 $\pm$ 0.004 MeV, the present data] and that of ${}^{4}_{\Lambda}\mathrm{H}(1^+)$ [1.09 $\pm$0.02 MeV, the average of the past three experiments [13, 14, 15]] is definitively non zero. Therefore, the existence of CSB in ΛN interaction has been confirmed via γ-ray data alone. By comparing differences in B_Λ's of the 0^+ and 1^+ states between ${}^{4}_{\Lambda}$H and ${}^{4}_{\Lambda}$He, namely $\Delta B_\Lambda(0^+) = B_\Lambda({}^{4}_{\Lambda}\mathrm{He}(0^+)) - B_\Lambda({}^{4}_{\Lambda}\mathrm{H}(0^+))$ $= +0.35 \pm 0.05$ MeV and $\Delta B_\Lambda(1^+) = +0.03 \pm 0.05$, we have discovered a large spin dependence in the CSB effect; the CSB effect is pronounced in the 0^+ state while vanishingly small in the 1^+ state. This fact suggests that Σ mixing in Λ hypernuclei is responsible for the CSB effect since the 0^+ state in ${}^{4}_{\Lambda}\mathrm{H}/{}^{4}_{\Lambda}\mathrm{He}$ is expected to receive one order of magnitude larger energy shift due to Λ-Σ mixing than the 1^+ state [8].

The result presented in this thesis has confirmed a sizable CSB effect in ΛN interaction and its strong spin dependence. Further theoretical studies of ΛN-ΣN interaction will explain the observed CSB effect, giving a relevant contribution to our understanding of baryon-baryon interactions.

Appendix A

Past γ-ray spectroscopic experiments of ${}^{4}_{\Lambda}$H/${}^{4}_{\Lambda}$He

A detailed description of the past γ-ray measurements which claimed assigned γ-lines belonging to ${}^{4}_{\Lambda}$H/${}^{4}_{\Lambda}$He is shown in this Appendix. Unassigned γ lines reported in other experiments for the hyperfragments, which are considered to be from ${}^{4}_{\Lambda}$He and ${}^{4}_{\Lambda}$H, are discussed at the end.

A.1 Summary of γ-ray measurement for ${}^{4}_{\Lambda}$H/${}^{4}_{\Lambda}$He

Adding the present result of excitation energy of ${}^{4}_{\Lambda}$He(1^+), 1.406 MeV, the list of γ-ray data was updated as shown in Table A.1.1 and Fig. A.1. In addition, the unassigned γ lines, which were suggested to be attributed to ${}^{4}_{\Lambda}$H and ${}^{4}_{\Lambda}$He based on the present result (see A.3), are also listed in the figure and the table. The averaged energies are summarized in Table A.1.2.

Prior to the present work, there were three reports assigning γ rays to ${}^{4}_{\Lambda}$H and one for ${}^{4}_{\Lambda}$He (see A.2). The result of the present work, $E_{\rm ex}[{}^{4}_{\Lambda}{\rm He}(1^+)]$= 1.406 MeV, supersedes the previously reported energy of $E_{\rm ex}[{}^{4}_{\Lambda}{\rm He}(1^+)]$= 1.15 MeV. The averaged excitation energy is 1.09 $\pm$0.02 MeV and 1.406 $\pm$0.004 MeV for ${}^{4}_{\Lambda}$H(1^+) and ${}^{4}_{\Lambda}$He(1^+), respectively, where the result of the past experiment for ${}^{4}_{\Lambda}$He [14] is not included. Then a difference between these energies, $\Delta E_{\rm ex}$=$E_{\rm ex}[{}^{4}_{\Lambda}{\rm He}(1^+)]$−$E_{\rm ex}[{}^{4}_{\Lambda}{\rm H}(1^+)]$, is +0.32 $\pm$0.02 MeV.

If the results for the unassigned γ rays are considered, the average excitation energy is 1.093 $\pm$0.004 MeV and 1.407 $\pm$0.004 MeV for ${}^{4}_{\Lambda}$H(1^+) and ${}^{4}_{\Lambda}$He(1^+), respectively. Then the difference between the two energies becomes +0.314 $\pm$0.006 MeV. The average energies with and without including the unassigned γ rays agree within the errors.

In addition, we are now proposing a new γ-ray spectroscopic experiment at J-PARC to measure the excitation energy of ${}^{4}_{\Lambda}$H(1^+) [67].

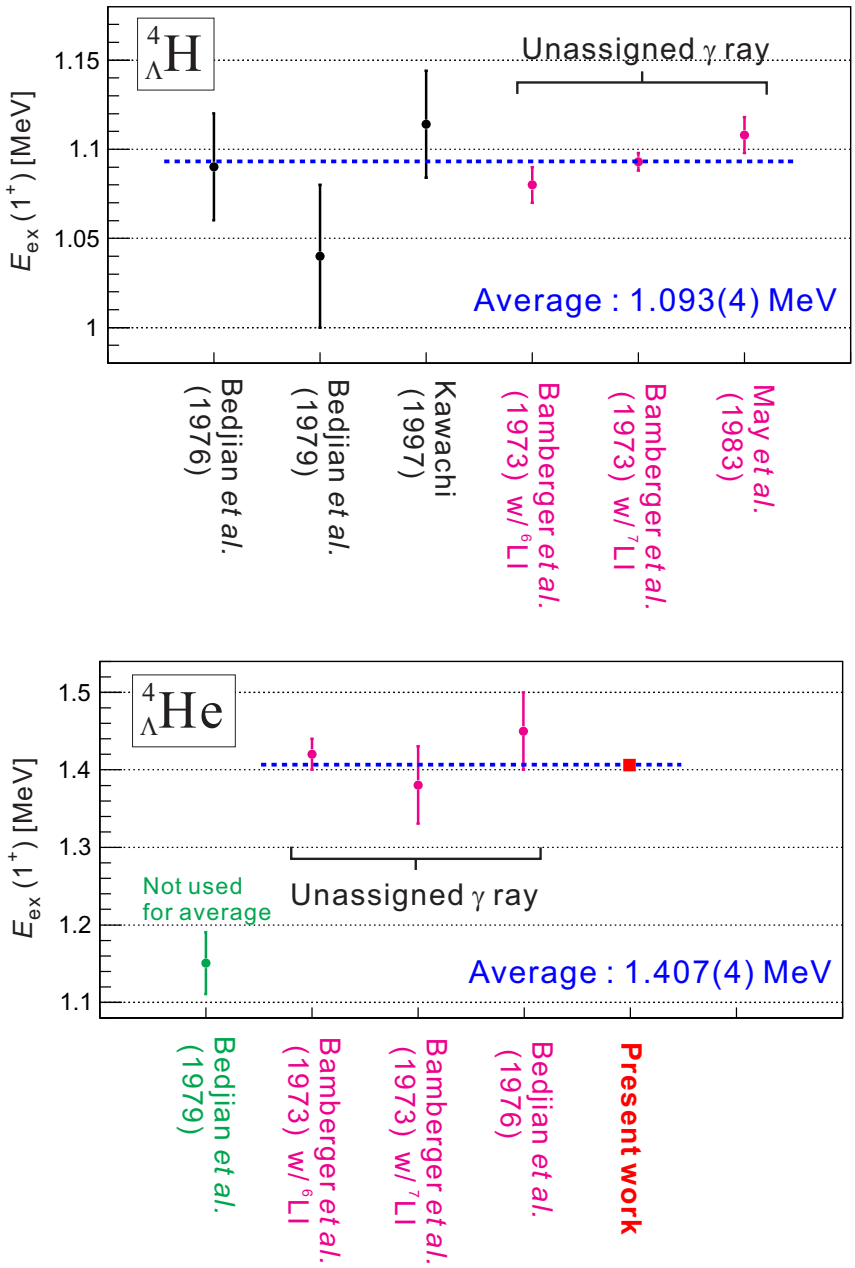

Figure A.1: Measured γ-ray energies from ${}^{4}_{\Lambda}H/{}^{4}_{\Lambda}He$. The assigned γ rays (black circle) and the result of the present result (red box) are plotted. In addition, the unassigned γ lines (magenta circle) are also used for averaging energies. The result of the past measurement for ${}^{4}_{\Lambda}He$ [14] is not included for averaging.

A.2 On the assigned γ-lines

The ${}^{4}_{\Lambda}H$ γ ray was measured three times, and the weighted average of excitation energies (E_{ex}) of ${}^{4}_{\Lambda}H(1^{+})$ was 1.09 ± 0.02 MeV. These three measurements reported E_{ex} as 1.09

Table A.1.1: Measured γ-ray energy list for ${}^{4}_{\Lambda}$H/${}^{4}_{\Lambda}$He. Unit is in MeV.

	${}^{4}_{\Lambda}\mathrm{H}(1^+ \to 0^+)$	${}^{4}_{\Lambda}\mathrm{He}(1^+ \to 0^+)$
Assigned γ line		
M. Bedjidian *et al.* (1976) [13]	1.09 ±0.03	-
M. Bedjidian *et al.* (1979) [14]	1.04 ±0.04	1.15 ±0.04
A. Kawachi (1997) [15]	1.114 ±0.030	-
Unassigned γ line		
A. Bamberger *et al.* (1973) [25] (^{6}Li target)	1.08 ±0.01	1.42 ± 0.02
A. Bamberger *et al.* (1973) [25] (^{7}Li target)	1.093 ±0.005	1.38 ± 0.05
M. Bedjidian *et al.* (1976) [13]	-	1.45 ± 0.05
M. May *et al.* (1983) [59]	1.108 ±0.010	-
Present experiment	-	1.406 ±0.004

Table A.1.2: Averaged γ-ray energy of ${}^{4}_{\Lambda}$H/${}^{4}_{\Lambda}$He. Unit is in MeV.

	${}^{4}_{\Lambda}\mathrm{H}(1^+ \to 0^+)$	${}^{4}_{\Lambda}\mathrm{He}(1^+ \to 0^+)$	$\Delta E_{\mathrm{ex}}[{}^{4}_{\Lambda}\mathrm{He}-{}^{4}_{\Lambda}\mathrm{H}]$
Assigned γ ray	1.09 ±0.02	1.406 ±0.004	+0.32 ±0.02
Assigned + Unassigned γ ray	1.093 ±0.004	1.407 ±0.004	+0.314 ±0.006

± 0.03 MeV (reported by M. Bedjidian *et al.* (1976) [13]), 1.04 ± 0.04 MeV (reported by M. Bedjidian *et al.* (1979) [14]), and 1.114 ± 0.030 MeV (reported by A. Kawachi (1997) [15]). On the other hand, the observation of the ${}^{4}_{\Lambda}$He γ ray was reported only once, which claimed the $(1^+, 0^+)$ energy spacing of $E_{\mathrm{ex}}({}^{4}_{\Lambda}\mathrm{He}(1^+))$=1.15 ± 0.04 MeV (reported by M. Bedjidian *et al.* (1979) [14]).

The descriptions of the previous experiments are shown in the followings.

Experiment-I (report by M. Bedjidian *et al.* (1976))

The first γ-ray measurement in the A=4 hypernuclei was reported by M. Bedjidian *et al.* in 1976 [13]. They reported the excitation energy of ${}^{4}_{\Lambda}\mathrm{H}(1^+)$ to be 1.09 ±0.03 MeV.

In the experiment performed at CERN, ${}^{4}_{\Lambda}\mathrm{H}^*$ was produced as a hyperfragment via the stopped K^- absorption on a ^{6}Li target and a ^{7}Li target. The γ-ray energy was measured by a NaI(Tl) counter with an energy resolution of 11% (FWHM) for the 1.1-MeV γ rays. Because the kinetic energy of π^- emitted from the two-body ${}^{4}_{\Lambda}\mathrm{H} \to {}^{4}\mathrm{He} + \pi^-$ weak decay channel is monochromatic and not overlap with that from other hyperfragments, they employed charged pion counter to tag the ${}^{4}_{\Lambda}$H decay. A telescope (range counter) for charged pion, consisting of MWPCs, a copper moderator and scintillation counters, was employed. This is because the previous experiment [25], which used also the stopped K^- reaction on the ^{6}Li and the ^{7}Li target and NaI counters, observed unassigned γ lines

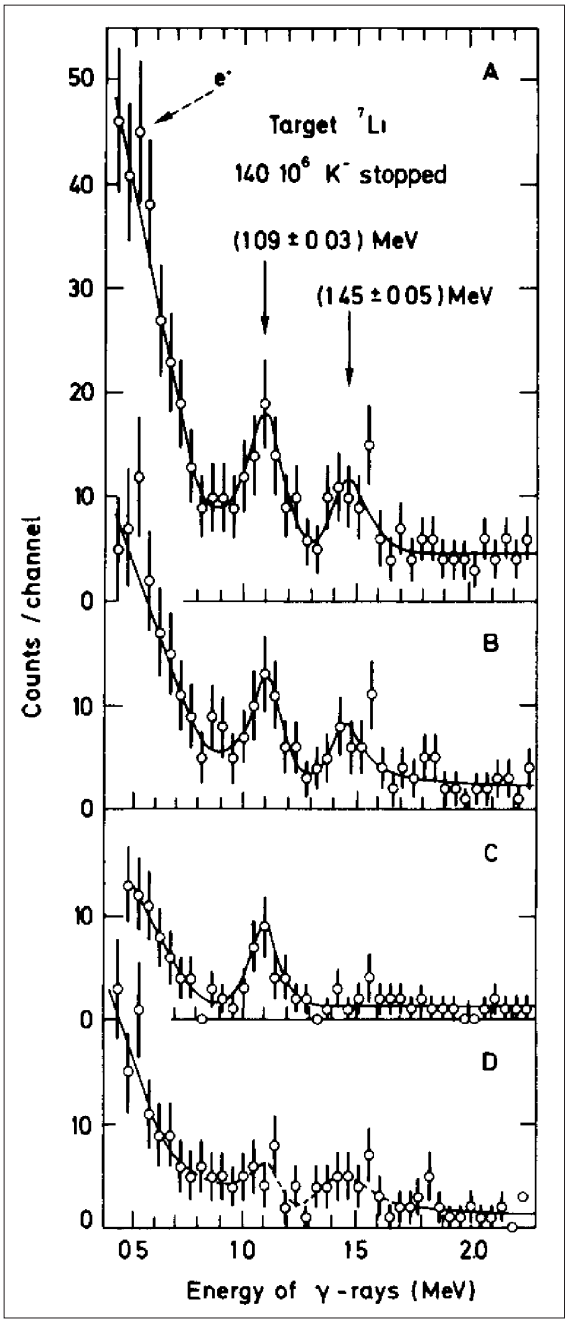

(A) Tagging π^-

1.45 ±0.05 MeV: unknown γ line

(B) Tagging π^- [selecting single particle in the telescope]

(C) Tagging π^- [selecting kinetic energy for the ${}^{4}_{\Lambda}H$ weak decay]

1.09 ±0.03 MeV: reported as ${}^{4}_{\Lambda}H$ ($1^+ \rightarrow 0^+$)

(D) Tagging π^- [selecting higher kinetic energy]

Figure A.2: γ-ray energy spectra reported by M. Bedjidian *et al.* (1976) [13]; (A) taking a coincidence between the NaI counter and the pion telescope including events in which multi particles were detected in the telescope, (B) same as (A) but multi particle events were rejected, (C) selecting a pion with a kinetic energy of 46–58 MeV, (D) selecting a pion with a kinetic energy of >58 MeV.

which would be attributed to ${}^{4}_{\Lambda}H^*$ or ${}^{4}_{\Lambda}He^*$. Figure A.2 shows the obtained γ-ray energy spectra. They reported a γ-ray peak at 1.09 MeV with a peak-to-background ratio of 4 ±1 as shown in Fig. A.2 (C), when a single charged pion with a kinetic energy of

46–58 MeV was selected (the kinetic energy of π^- from ${}^4_\Lambda$H weak decay is expected to be 53 MeV). This γ line was not clearly seen in the spectra with selecting a different kinetic energy region of >58 MeV. Therefore, they assigned the 1.09-MeV γ line as the ${}^4_\Lambda\mathrm{H}(1^+ \to 0^+)$ transition. A description for the 1.45-MeV γ line is given in A.3.

Experiment-II (report by M. Bedjidian *et al.* (1979))

Based on the result of the previous experiment [13], M. Bedjidian *et al.* performed γ-ray spectroscopy again by additionally introducing a π^0 counter [14]. Because the kinetic energy of π^0 emitted from the two-body ${}^4_\Lambda\mathrm{He} \to {}^4\mathrm{He} + \pi^0$ weak decay channel is monochromatic, they employed π^0 counter to tag the ${}^4_\Lambda$He decay. They reported the excitation energy of ${}^4_\Lambda\mathrm{He}(1^+)$ to be 1.15 $\pm$0.04 MeV, and also 1.04 $\pm$0.04 MeV for ${}^4_\Lambda\mathrm{H}(1^+)$.

Figure A.3 shows the experimental setup. Basically the experimental method is the same as the previous one. They used the stopped K^- reaction on the ^{6}Li and the ^{7}Li target, and measured γ rays by using NaI detectors taking a coincidence with the stopped K^- trigger. γ-ray spectra obtained only by a 4"×3" NaI detector, "NaI 1" as shown

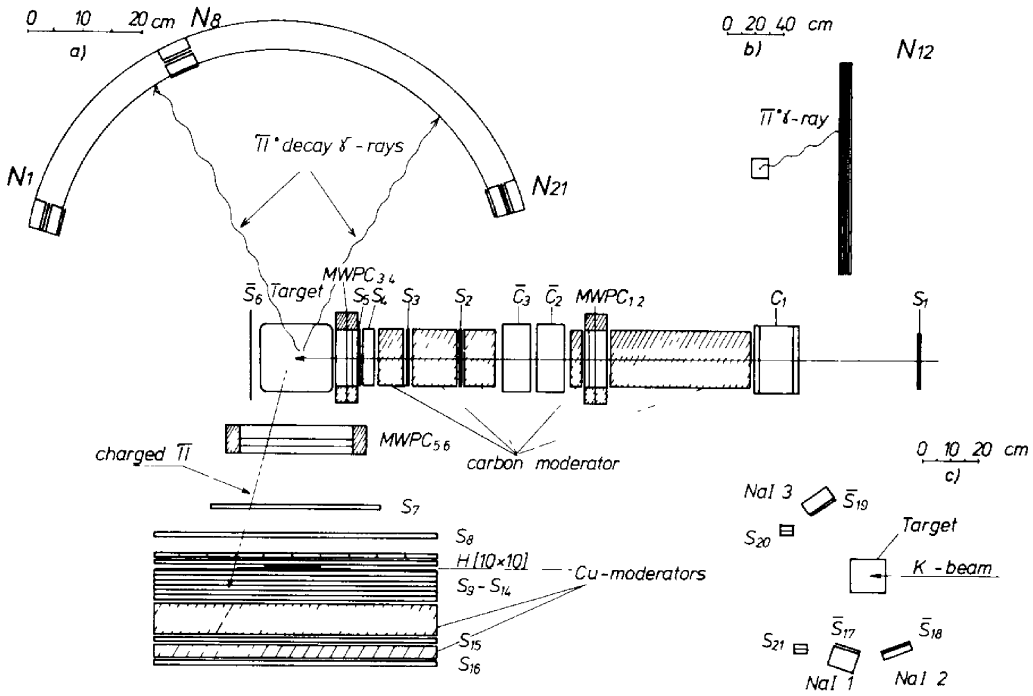

Figure A.3: Detector setup of the experiment described by M. Bedjidian *et al.* (1979) [14]. (a) shows a top view of the setup, where π^0 counter (labeled with N_{1-21}) and a charged pion telescope (shown in the lower consisting of MWPCs, Cu moderators and scintillation counters) were employed to tag π^0 and π^- from hypernuclear weak decay. (b) shows a side view of the π^0 counter. (c) shows positions of NaI detectors (side view).

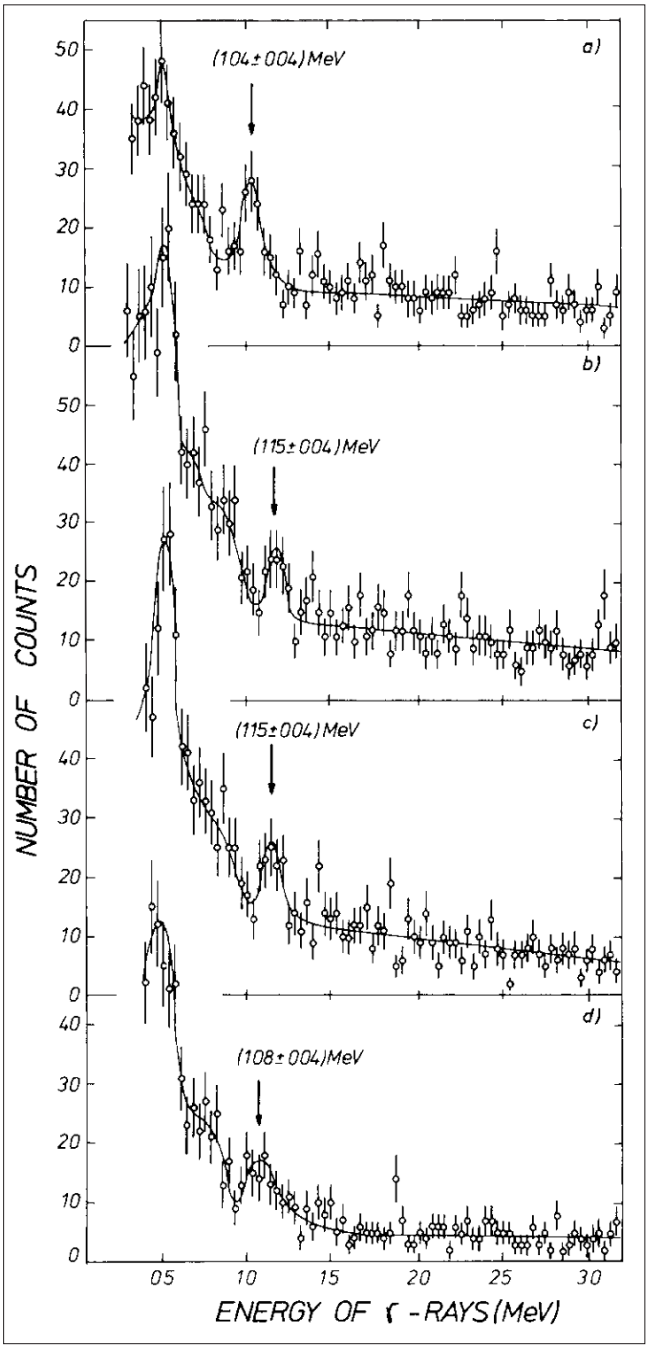

Figure A.4: γ-ray energy spectra reported by M. Bedjidian *et al.* (1979) [14]; (A) summed spectrum for the ^{6}Li and ^{7}Li target after selecting a charged pion with a kinetic energy (E_{kin}) of 48–58 MeV, (B) same as (A) but selecting π^0 with E_{kin} = 45–85 MeV, (C) spectrum of the ^{6}Li target only by selecting π^0 with E_{kin} = 200–400 MeV, (D) spectrum of the ^{7}Li target only by selecting π^0 with E_{kin} = 100–180 MeV.

in Fig. A.3 (C), were reported in the article. The energy resolution was 12% (FWHM) at 0.98 MeV. The π^0 counter, which is composed of double Pb-scintillator sandwiched

counters (N_{1-21}), was introduced to tag two γ rays from $\pi^0 \to \gamma\gamma$ decay. A kinetic energy of π^0 was deduced from an opening angle between the two γ rays. A higher kinetic energy leads to a smaller opening angle. The reported angular resolution was $\pm 3.5^\circ$ as a result of the horizontally segmented scintillation counters and a time difference of the scintillation light arriving to each edge of the counter. The charged pion telescope was also employed with almost the same configuration as the previous experiment [13].

Figure A.4 shows obtained γ-ray energy spectra. They found a γ line at 1.04 $\pm$0.04 MeV in the spectrum (A), selecting charged pion with a kinetic energy (E_{kin}) of 48–58 MeV. The γ line was assigned as the ${}^{4}_{\Lambda}\mathrm{H}(1^+ \to 0^+)$ transition, and its energy was consistent with the previous result of 1.09 $\pm$0.03 MeV. In the spectrum (B), selecting π^0 with E_{kin} = 45–85 MeV, a γ line at 1.15 $\pm$0.05 MeV was observed. (The kinetic energy of π^0 from ${}^{4}_{\Lambda}\mathrm{He}$ weak decay is expected to be 57 MeV.) The γ line was assigned as the ${}^{4}_{\Lambda}\mathrm{He}(1^+ \to 0^+)$ transition. This was the first and only experimental value for the $E_{\mathrm{ex}}({}^{4}_{\Lambda}\mathrm{He}(1^+))$ before the present work. The 1.15-MeV γ line was also seen in the spectrum (C), selecting π^0 with much higher E_{kin} of 200–400 MeV of unphysical origin. It was concluded that the appeared peak was induced by two π^0 from different sources; one came from the hyperon production such as stopped $K^- + p \to \Lambda + \pi^0$ and the other from the hypernuclear weak decay $[{}^{4}_{\Lambda}\mathrm{He} \to {}^{4}\mathrm{He} + \pi^0]$.

However, the statistical significance of the 1.15-MeV peak seems to be less than 3σ, due to a limited resolution of the NaI detectors as well as Doppler broadening and poor statistics. Furthermore, their identification of the ${}^{4}_{\Lambda}\mathrm{He}$ hyperfragment by means of using a kinetic energy of π^0 from an opening angle of two γ rays is not conclusive. These factors motivated us to perform a γ-ray measurement of ${}^{4}_{\Lambda}\mathrm{He}$ with our state of the art device. A comparison with the present work is described in Section 6.1.

Experiment-III (report by A. Kawachi (1997))

The most recent γ-ray spectroscopic experiment was performed at KEK. A. Kawachi reported $E_{\mathrm{ex}}({}^{4}_{\Lambda}\mathrm{H}(1^+))$ to be 1.114 $\pm$0.030 MeV [15].

The purpose of the experiment was to measure the production rate of light hyperfragments, ${}^{5}_{\Lambda}\mathrm{He}$, ${}^{4}_{\Lambda}\mathrm{He}$, and ${}^{4}_{\Lambda}\mathrm{H}^*$ via the stopped K^- reaction on several targets (^{7}Li, ^{9}Be, and ^{12}C). Toroidal Spectrometer was employed for tagging of π^- from the hypernuclear weak decay having a momentum of 90–140 MeV/c. Produced hyperfragments were identified with a typical momentum resolution of 3 MeV/c (FWHM) at 133 MeV/c, which corresponds to a momentum of π^- from the ${}^{4}_{\Lambda}\mathrm{H}$ weak decay. A total of 24 NaI detectors ($\phi 3" \times 3"^{L}$ and 3" square$\times 3"^{L}$ crystal) was installed near the target to detect γ rays from ${}^{4}_{\Lambda}\mathrm{H}^*$ with an energy resolution of 7–9% at 662 keV.

Figure A.5 shows obtained γ-ray energy spectra respective to the ^{7}Li (A), ^{9}Be (B)

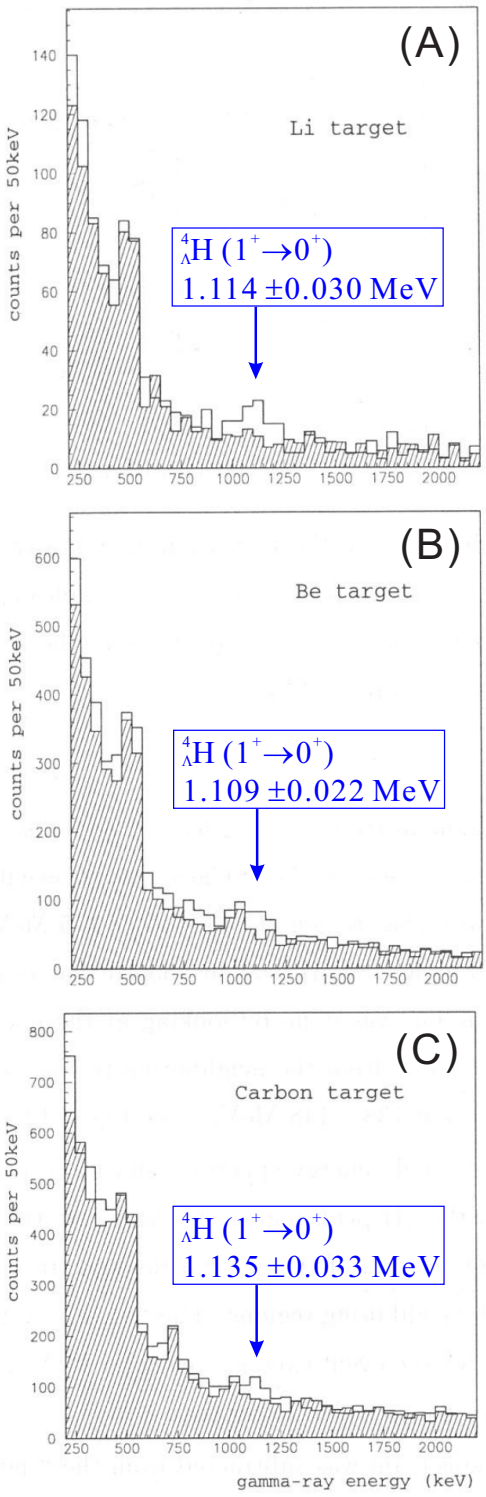

Figure A.5: γ-ray energy spectra reported by A. Kawachi (1997) [15]. (A) ,(B) and (C) show the spectra with the ^{7}Li, ^{9}Be and ^{12}C targets, respectively. Background distributions (hatched) was estimated by selecting side region of the π^{-} momentum.

Table A.2.1: γ-ray peak positions for ${}^{4}_{\Lambda}\mathrm{H}^{*}$ reported by A. Kawachi [15].

Target	Peak center [MeV]
^{7}Li	1.114 $\pm$0.030
^{9}Be	1.109 $\pm$0.022
^{12}C	1.135 $\pm$0.033
fitting three spectra with common centroid	1.114 $\pm$0.030

and ^{12}C (C) target, where the background indicated in hatched spectra was estimated by selecting side regions of the π^{-} momentum. Observed enhancement at 1.1 MeV in all of the γ-ray spectra corresponds to the ${}^{4}_{\Lambda}\mathrm{H}(1^{+} \rightarrow 0^{+})$ transition. Reported peak positions were listed in Table A.2.1. The excitation energy $[E_{\mathrm{ex}}({}^{4}_{\Lambda}\mathrm{H}(1^{+}))]$ was 1.114 $\pm$0.030 MeV after fitting three spectra with a common centroid parameter. The obtained value is consistent with the other two values reported by M. Bedjidian *et al.*, namely 1.09 $\pm$0.03 MeV and 1.04 $\pm$0.04 MeV.

A.3 On the unassigned γ-lines

It is to be noted that two previous experiments using a stopped K^{-} on ^{6}Li and ^{7}Li targets had reported hints of unassigned γ-ray peaks at 1.42 $\pm$ 0.02 MeV [25] and 1.45 $\pm$ 0.05 MeV [13], respectively. In addition, another old experiment reported an unassigned γ line at 1.08 MeV [59]. Taking into an account of the present result, we suggest updated assignment for these γ lines. A description of these experiments are shown in followings.

Report by Bamberger *et al.*

A. Bamberger *et al.* reported two unassigned γ lines at the energy of 1.09 MeV and 1.42 MeV [25]. The method of γ-ray measurement of this experiment was similar to that of the other older experiments [13, 14]; the stopped K^{-} reaction was used for the hyperfragment production with ^{6}Li and ^{7}Li target, and NaI detectors were used for detecting γ rays. Figure A.6 shows the γ-ray energy spectrum, where a coincidence between stopped K^{-} and γ ray was taken.

They reported that two bump structures were found in the γ-ray energy spectrum with the ^{6}Li target as shown in Fig. A.6 (A). Reported energies were 1.08 $\pm$ 0.01 MeV and 1.42 $\pm$ 0.02 MeV, respectively. They also found these bumps with the ^{7}Li target as shown in Fig. A.6 (B). The reported energies are listed in Table A.3.1. They discussed that ${}^{4}_{\Lambda}\mathrm{H}^{*}$ or ${}^{4}_{\Lambda}\mathrm{He}^{*}$ were the only candidates responsible for these bump structures, considering the Λ binding energies of the hyperfragments which can be produced from the ^{6}Li target. They did not assign these γ lines without any methods of identifying hyperfragments.

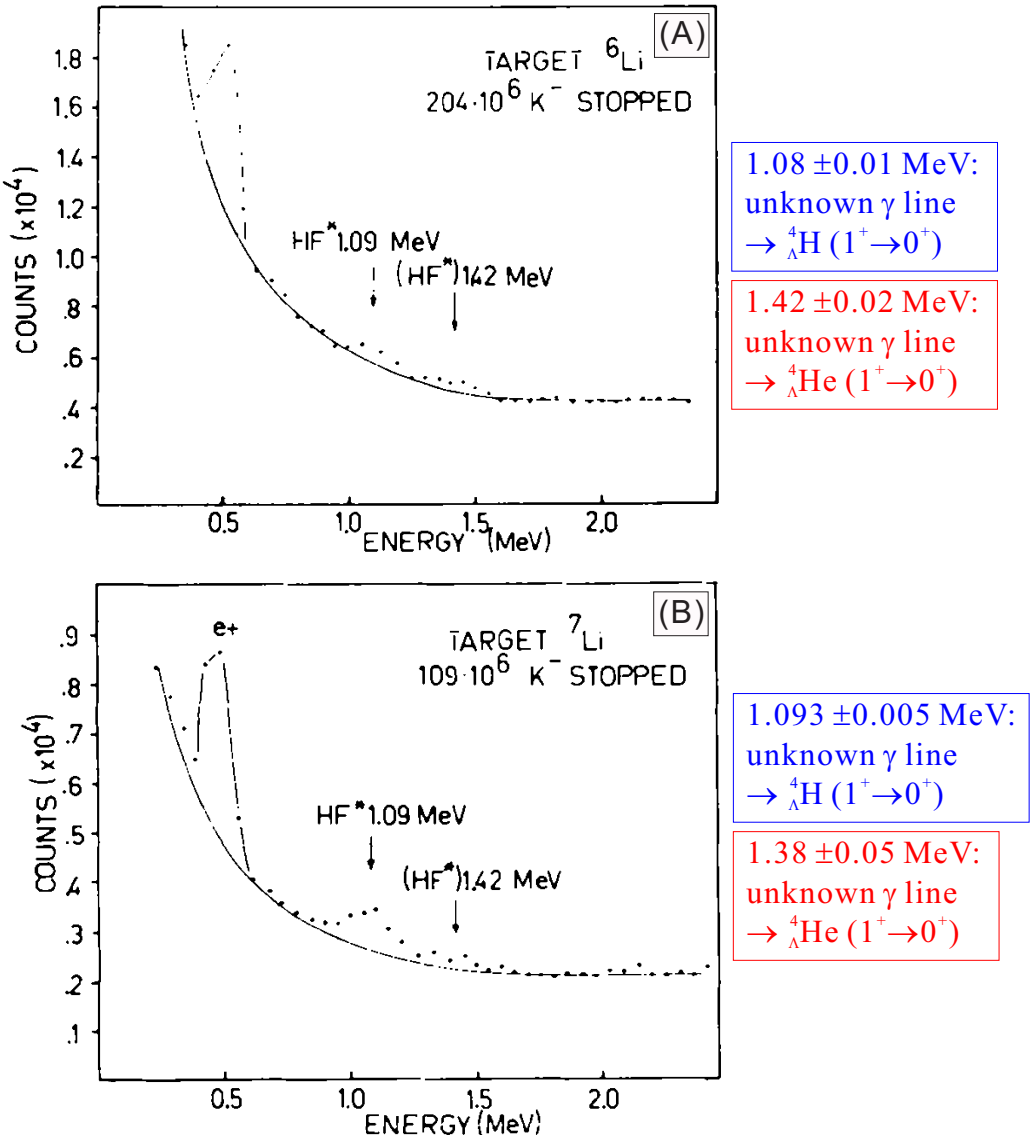

Figure A.6: γ-ray energy spectrum obtained in the experiment reported by A. Bamberger *et al.* [25], where a coincidence between stopped K^- and γ ray was taken. (A) and (B) show the spectra with the ^{6}Li target and the ^{6}Li target, respectively.

Table A.3.1: γ-ray energies reported by A. Bamberger *et al.* [25]

		1.09-MeV peak position [MeV]	1.42-MeV peak position [MeV]
^{6}Li target		1.08 ±0.01	1.42 ± 0.02
^{7}Li target		1.093 ±0.005	1.38 ± 0.05
Averaged energy	${}^{4}_{\Lambda}H(1^+ \to 0^+)$	1.09 ±0.02	-
Present experiment	${}^{4}_{\Lambda}He(1^+ \to 0^+)$	-	1.406 ±0.002 ±0.002

The energy position of the first bump was consistent with the averaged energy of the ${}^{4}_{\Lambda}\mathrm{H}(1^{+} \to 0^{+})$ transition (1.09 $\pm$0.02 MeV), and that of the second bump with our result of the 1.406 $\pm$0.002 $\pm$0.002 MeV for the ${}^{4}_{\Lambda}\mathrm{He}(1^{+} \to 0^{+})$ transition. Therefore, we speculate that the reported peaks correspond to the ${}^{4}_{\Lambda}\mathrm{H}(1^{+} \to 0^{+})$ and ${}^{4}_{\Lambda}\mathrm{He}(1^{+} \to 0^{+})$ transition, respectively.

Report by Bedjidian *et al.*

M. Bedjidian *et al.* reported an unassigned γ line at 1.45 MeV [13]. Their experiment was already mentioned in A.2. The γ rays from ${}^{4}_{\Lambda}\mathrm{H}$ were tagged by detecting π^{-} from the decay of ${}^{4}_{\Lambda}\mathrm{H}$, having a kinetic energy of 46–58 MeV, and the γ-ray energy was measured to be 1.09 $\pm$0.03 MeV. Figure A.7 shows the γ-ray energy spectrum obtained in this experiment, detecting π^{-} in the range counter without selecting its kinetic energy. A second bump structure at the energy of 1.45 $\pm$0.05 MeV is seen in this spectrum. This energy is consistent with the present result of 1.406 $\pm$ 0.002 $\pm$ 0.002 MeV for the ${}^{4}_{\Lambda}\mathrm{He}(1^{+} \to 0^{+})$ transition. It is possible that both ${}^{4}_{\Lambda}\mathrm{H}^{*}$ and ${}^{4}_{\Lambda}\mathrm{He}^{*}$ were produced as fragments following the stopped $K^{-}+N \to \Lambda\pi, \Sigma\pi$ reaction, and the π^{-} emitted in these reactions was detected by the range counter. Therefore, we think that the unassigned γ line at 1.45 MeV should be attributed to the ${}^{4}_{\Lambda}\mathrm{He}(1^{+} \to 0^{+})$ transition.

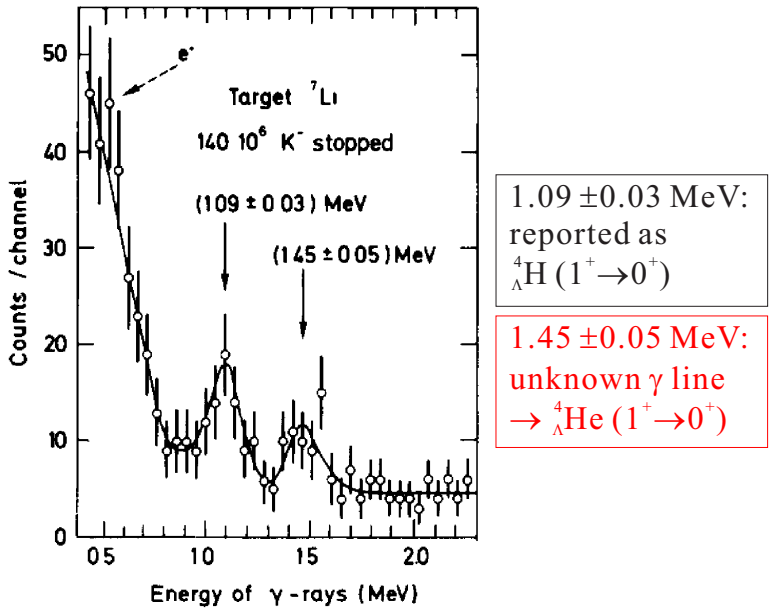

Figure A.7: A γ-ray energy spectrum obtained in the experiment reported by M. Bedjidian *et al.* [13], taking a triple coincidence among the stopped K^{-}, a charged pion, and a γ ray.

Report by M. May *et al.*

M. May *et al.* reported an unassigned γ line at 1.108 MeV [59]. They performed a γ-ray spectroscopic experiment via the in-flight ^{7}Li(K^-,π^-) reaction. Hypernuclear production was tagged by calculating the missing mass by using magnetic spectrometers to measure the momenta of the K^- and π^-. This method is the same as the present experiment. Taking a coincidence between the (K^-,π^-) reaction and the γ ray detected by eight NaI detectors, the γ-ray spectra were obtained as shown in Fig. A.8, where spectrum (a) is with the missing mass gate on the ${}^{7}_{\Lambda}$Li bound region ($-2 < E_{\rm ex} < 6$ MeV), (b) is on the unbound region ($6 < E_{\rm ex} < 22$ MeV), and (c) is on the highly unbound region ($22 < E_{\rm ex} < 39$ MeV). The threshold for the fragmentation decay, ${}^{7}_{\Lambda}$Li$\rightarrow{}^{4}_{\Lambda}H+{}^{3}$He, is at $E_{\rm ex} \cong 19$ MeV. Therefore, the γ ray from ${}^{4}_{\Lambda}$H* can be observed in the spectrum (c). A single peak was found at the energy of 1.108 ± 0.010 MeV. In their report [59],

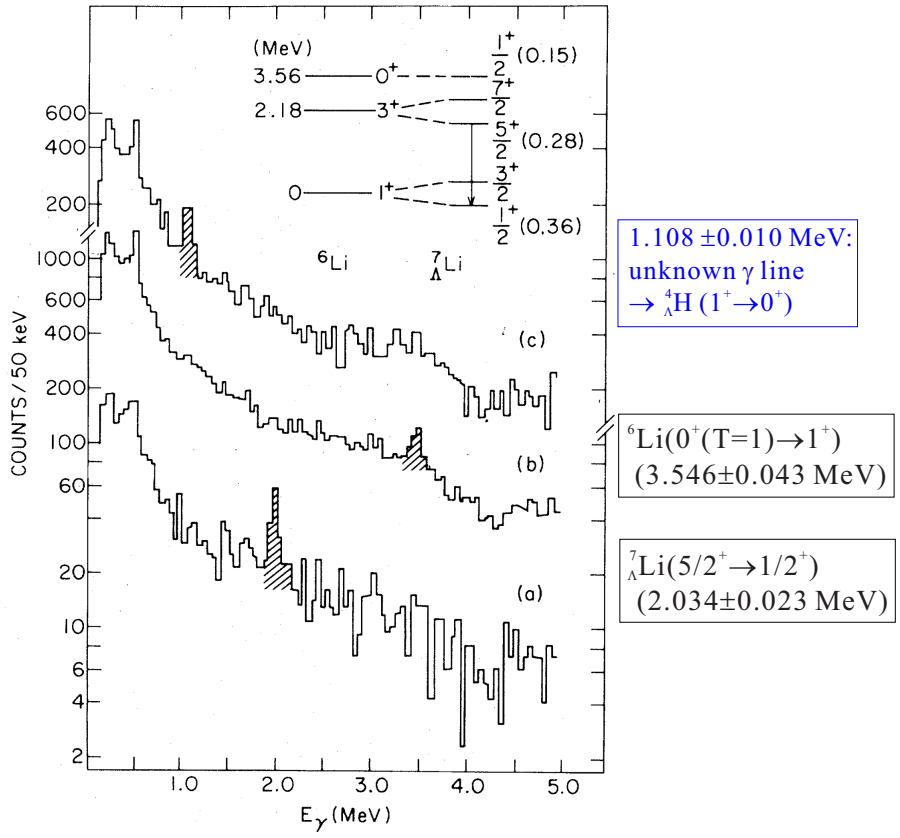

Figure A.8: γ-ray energy spectrum obtained in the experiment reported by M. May *et al.* [59], by taking a coincidence between the in-flight (K^-,π^-) reaction and the γ ray. The missing mass was calculated by measuring momenta of the beam K^- and scattered π^-. The γ-ray spectra with the missing mass gate are shown; (a) $-2 < E_{\rm ex} < 6$ MeV, (b) $6 < E_{\rm ex} < 22$ MeV, and (c) $22 < E_{\rm ex} < 39$ MeV.

they concluded that the peak was attributed to the sum of the two transitions, the ${}^{4}_{\Lambda}\mathrm{H}(1^{+} \to 0^{+})$ and the ${}^{4}_{\Lambda}\mathrm{He}(1^{+} \to 0^{+})$ transitions, because the known excitation energies of ${}^{4}_{\Lambda}\mathrm{H}^{*}$ and ${}^{4}_{\Lambda}\mathrm{He}^{*}$, 1.04 MeV and 1.15 MeV at that time, were too close to be resolved by the NaI detectors with the energy resolution of 0.084 MeV (FWHM). The present result suggests that the observed 1.108 MeV peak is attributed only to the ${}^{4}_{\Lambda}\mathrm{H}(1^{+} \to 0^{+})$ transition because of the 1.406-MeV transition energy of ${}^{4}_{\Lambda}\mathrm{He}$.

It is possible as well to observe γ rays from ${}^{4}_{\Lambda}\mathrm{He}$ in the spectrum (c) because the threshold for the decay, ${}^{7}_{\Lambda}\mathrm{Li} \to {}^{4}_{\Lambda}\mathrm{He} + {}^{3}\mathrm{H}$, is at $E_{\mathrm{ex}} \cong 19$ MeV. No peak structure was reported near the energy of 1.4 MeV in the spectrum (c). This fact indicates that the hyperfragment production rate of ${}^{4}_{\Lambda}\mathrm{He}^{*}$ is lower in the in-flight ${}^{7}\mathrm{Li}(K^{-}, \pi^{-})$ reaction.

Appendix B

Study of the CSB effect in p-shell hypernuclei

B.1 Emulsion experiments

B_Λ(g.s.) values of A<15 hypernuclei were measured by the emulsion method [9, 10]. The measured B_Λ(g.s.) values of p-shell mirror hypernuclei are summarized in Table B.1.1. No significant CSB effect was reported in p-shell hypernuclei except for ${}^{12}_{\Lambda}$C/${}^{12}_{\Lambda}$B (a description for A=12 hypernuclei will be given in the next section).

Table B.1.1: B_Λ differences in the ground state of the p-shell mirror hypernuclei measured by emulsion experiments [10]. [see Ref. [11] for $B_\Lambda({}^{12}_{\Lambda}\mathrm{C})$]. Unit is in MeV.

hypernuclei	B_Λ(g.s.)		ΔB_Λ(g.s.)	
	emulsion	reaction	emulsion	with reaction
${}^{7}_{\Lambda}$He	-	5.60 ± 0.17 [70, 71]	-	−0.44 ± 0.19
${}^{7}_{\Lambda}$Be	5.16 ± 0.08	-		
${}^{8}_{\Lambda}$Li	6.80 ± 0.03	-	+0.04 ± 0.06	-
${}^{8}_{\Lambda}$Be	6.84 ± 0.05	-		
${}^{9}_{\Lambda}$Li	8.50 ± 0.12	8.36 ± 0.16 [72]	−0.21 ± 0.22	−0.07 ± 0.24
${}^{9}_{\Lambda}$B	8.29 ± 0.18	-		
${}^{10}_{\Lambda}$Be	9.11 ± 0.22	8.60 ± 0.18 [12]	−0.22 ± 0.25	(−0.50 ± 0.21)
${}^{10}_{\Lambda}$B	8.89 ± 0.12	(8.1 ± 0.1)*[73]		+0.04 ± 0.21*
${}^{12}_{\Lambda}$B	11.37 ± 0.06	11.524 ± 0.019 [74]	(−0.57 ± 0.19)	(−0.72 ± 0.18)
${}^{12}_{\Lambda}$C	(10.80 ± 0.18)*	-	−0.03 ± 0.19*	−0.18 ± 0.18*

* A recent systematic study suggests that the quoted emulsion value of $B_\Lambda({}^{12}_{\Lambda}\mathrm{C})$ should be shifted by +0.54 MeV [12]. This shift is reflected also in ${}^{10}_{\Lambda}$B data because the $B_\Lambda({}^{12}_{\Lambda}\mathrm{C})$ value was used for their energy calibration.

B.2 Experiments via the $(e, e'K^+)$ reaction

Recently, reaction spectroscopy employing the $p(e, e'K^+)\Lambda$ reaction was successfully performed at Jefferson Lab. With respect to hypernuclei produced using the $n(K^-, \pi^-)\Lambda$ or the $n(\pi^+, K^+)\Lambda$ reaction, their mirror hypernuclei can be produced with the $p(e, e'K^+)\Lambda$ reaction on the same target. For example, the mirror hypernuclei ${}^{12}_{\Lambda}$B with the $(e, e'K^+)$ reaction and ${}^{12}_{\Lambda}$C with the (K^-, π^-) reaction can be produced with a ^{12}C target). The results of these experiments, therefore, provide the study of the CSB effect in ΛN interaction with important information. In addition, absolute mass scale can be calibrated by using the elementary $p(e, e'K^+)\Lambda$ and Σ^0 production. This is not the case in the (K^-, π^-) or (π^+, K^+) reaction experiments where an elementally Λ production can not be used because free neutron is not available as a target. A=7, 9, 10, and 12 mirror hypernuclei were studied via the $(e, e'K^+)$ reaction. The results of the experiments are summarized together in Table B.1.1. A description for these experiments are given below.

A=7 hypernuclei

Figure B.1 shows the B_Λ values of A=7 iso-triplet hypernuclei, ${}^{7}_{\Lambda}$He, ${}^{7}_{\Lambda}$Li* and ${}^{7}_{\Lambda}$Be [${}^{7}_{\Lambda}$He and ${}^{7}_{\Lambda}$Be are the mirror hypernuclei]. $B_\Lambda({}^{7}_{\Lambda}\mathrm{Be})$ was measured to be 5.16 $\pm$0.08 MeV by

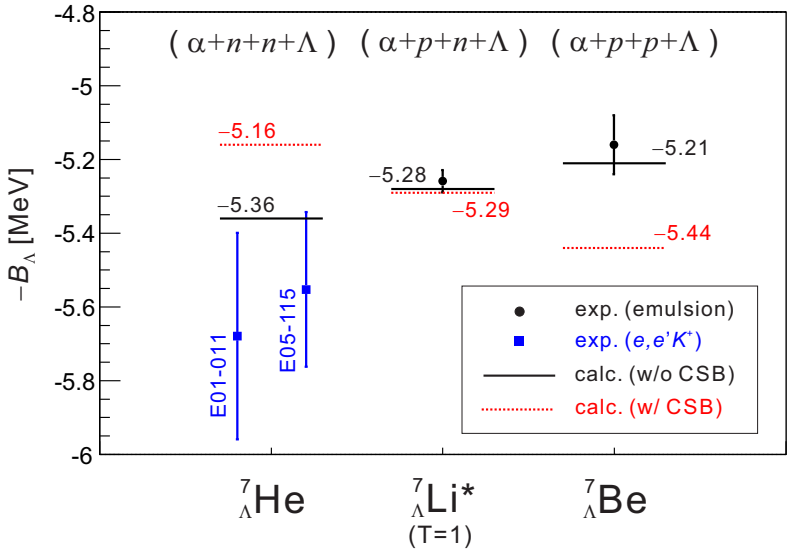

Figure B.1: B_Λ values of A=7 iso-triplet hypernuclei, ${}^{7}_{\Lambda}$He, ${}^{7}_{\Lambda}$Li* and ${}^{7}_{\Lambda}$Be. These values were measured by emulsion experiments [9] (black circles) and by the reaction spectroscopic experiments employing the $(e, e'K^+)$ reaction [70, 71] (blue boxes). E. Hiyama calculated B_Λ values with (dotted red lines) and without (solid black lines) a phenomenological ΛN CSB interaction [75].

the emulsion experiment [9]. That of ${}^{7}_{\Lambda}\mathrm{Li}^{*}$ was derived from the results of the emulsion experiment and of the γ-ray experiment [5] as 5.26 $\pm$0.03 MeV. No result was reported for ${}^{7}_{\Lambda}\mathrm{He}$ in the emulsion experiment because there are only $\sim$10 observed events and its B_Λ distribution was spread (they claimed that the reason was an existence of long-lived isomeric states) [9]. By employing the ${}^{7}\mathrm{Li}(e, e'K^+)$ reaction, it becomes possible to obtain $B_\Lambda({}^{7}_{\Lambda}\mathrm{He})$ with the missing mass method. The $(e, e'K^+)$ experiments, E01-011 and E05-115, were performed at Jefferson Lab and reported $B_\Lambda({}^{7}_{\Lambda}\mathrm{He})$ to be 5.68 $\pm$0.03 $\pm$0.25 MeV [70] and 5.55 $\pm$0.10 $\pm$0.11 MeV [71], respectively. A weighted average of $B_\Lambda({}^{7}_{\Lambda}\mathrm{He})$ is 5.60 $\pm$0.17 MeV. A difference in the measured B_Λ values is significantly large, $\Delta B_\Lambda = B_\Lambda({}^{7}_{\Lambda}\mathrm{Be}) - B_\Lambda({}^{7}_{\Lambda}\mathrm{He}) = -0.44 \pm 0.19$ MeV. However, a few-body calculation by E. Hiyama [75], which included only Coulomb interaction as the CSB origin, well reproduced the measured B_Λ values, indicating that no significant CSB effect other than Coulomb effect was found in the A=7 hypernuclear system. E. Hiyama also reported a result of a calculation with a phenomenological ΛN CSB interaction as shown together in Fig B.1, where parameters for the phenomenological CSB interaction was based on the (old) experimental data in the A=4 hypernuclear system. This calculation did not reproduced the measured B_Λ values.

A=9 hypernuclei

B_Λ(g.s.) values of A=9 mirror hypernuclei ${}^{9}_{\Lambda}\mathrm{Li}/{}^{9}_{\Lambda}\mathrm{B}$ were measured by the emulsion experiments [9]. The reported difference in B_Λ is $\Delta B_\Lambda = -0.21 \pm 0.22$ MeV, indicating no significant CSB effect.

The $B_\Lambda({}^{9}_{\Lambda}\mathrm{Li})$ was re-measured by a reaction spectroscopy experiment at JLab Hall-A using the ${}^{9}\mathrm{Be}(e, e'K^+){}^{9}_{\Lambda}\mathrm{Li}$ reaction [72]. The reported B_Λ was of 8.36 ± 0.16 MeV, leading to almost no CSB effect as $\Delta B_\Lambda = -0.07 \pm 0.19$ MeV. It is noted that the absolute mass calibration was made based on the $B_\Lambda({}^{12}_{\Lambda}\mathrm{B})$ value reported from the emulsion experiments [9].

A=10 hypernuclei

B_Λ(g.s.) values of A=10 mirror hypernuclei ${}^{10}_{\Lambda}\mathrm{Be}/{}^{10}_{\Lambda}\mathrm{B}$ were measured by the emulsion experiments [9]. The reported difference in B_Λ is $\Delta B_\Lambda = -0.22 \pm 0.25$ MeV, indicating no significant CSB effect.

The B_Λ values were remeasured by reaction spectroscopy experiments using the ${}^{10}\mathrm{B}(e, e'K^+){}^{10}_{\Lambda}\mathrm{Be}$ reaction [12] and the ${}^{10}\mathrm{B}(\pi^+, K^+){}^{10}_{\Lambda}\mathrm{B}$ reaction [73]. The reported B_Λ values are $B_\Lambda({}^{10}_{\Lambda}\mathrm{Be})$=8.60 $\pm$ 0.07 $\pm$ 0.11 MeV and $B_\Lambda({}^{10}_{\Lambda}\mathrm{B})$=8.1 $\pm$ 0.1 MeV. It should be noted that a recent systematic study suggests that the ${}^{10}_{\Lambda}\mathrm{B}$ data have a systematic

energy shift of +0.54 MeV in their energy calibration based on the quoted emulsion value of $B_\Lambda(^{12}_{\Lambda}\mathrm{C})$ (see the next section) [12]. The difference in B_Λ after +0.54 MeV correction is $\Delta B_\Lambda = B_\Lambda(^{10}_{\Lambda}\mathrm{B}) - B_\Lambda(^{10}_{\Lambda}\mathrm{Be}) = -0.04 \pm 0.21$ MeV, indicating that no significant CSB effect appears in A=10 hypernuclei.

A=12 hypernuclei

B_Λ(g.s.) values of A=12 mirror hypernuclei $^{12}_{\Lambda}\mathrm{B}/^{12}_{\Lambda}\mathrm{C}$ were measured by the emulsion experiments [9, 11]. The reported difference in B_Λ is $\Delta B_\Lambda = -0.57 \pm 0.19$ MeV. However, a recent systematic study suggests that the reported emulsion value of $B_\Lambda(^{12}_{\Lambda}\mathrm{C})$ should be shifted by +0.54 MeV by comparing the emulsion data and the (π^+, K^+) reaction data which are based on an emulsion value of $B_\Lambda(^{12}_{\Lambda}\mathrm{C})$ for their energy calibration [12]. Then, ΔB_Λ becomes -0.03 ± 0.19 MeV indicating almost no CSB effect.

The B_Λ values were remeasured by reaction spectroscopy experiments using the $^{12}\mathrm{C}(e, e'K^+)^{12}_{\Lambda}\mathrm{B}$ reaction [74]. The reported B_Λ was 11.524 ± 0.019 MeV, leading to no significant CSB effect as $\Delta B_\Lambda = -0.18 \pm 0.19$ MeV. Although there exist the (π^+, K^+) reaction data on $^{12}_{\Lambda}\mathrm{C}$ (see [73], for example), these do not provide (independently determined) a B_Λ value because the $B_\Lambda(^{12}_{\Lambda}\mathrm{C})$ value of emulsion data was used for their energy calibration. Therefore, these (π^+, K^+) reaction data provide only excitation energies.

B.3 Recent theoretical calculation

A. Gal calculated the CSB effects in the *s*- and *p*-shell mirror hypernuclei [64] with "D2 potential" (see the section 6.5 for the detailed description). The results of the calculation are summarized in Table B.3.1 together with the measured B_Λ difference. In his paper, a difference in B_Λ(g.s.) was calculated by taking into an account of a kinetic energy difference with the Σ mass difference (ΔT_{YN}), a change in the Coulomb effect by putting hyperons (ΔV_C), and an additional CSB effect, such as the Λ-Σ^0 conversion, (ΔV_{YN}). The result suggests two points; (1) the YN CSB effects (from ΔT_{YN} and ΔV_{YN}) on B_Λ(g.s.) appear largely in lighter hypernuclei, and (2) the effects of Coulomb interaction become larger in heavier hypernuclei. It is claimed that a ΛN-ΣN matrix element becomes smaller in *p*-shell hypernuclei than *s*-shell, leading to small Σ mixing probability and thus small contribution of both ΔT_{YN} and ΔV_{YN}. Therefore, the lighter hypernuclear system seems promising for the study of the CSB effect in ΛN interaction in terms of ΛN-ΣN mixing.

Table B.3.1: B_Λ differences in ground-state of the s- and p-shell mirror hypernuclei measured by the emulsion experiments [10, 9] and reaction spectroscopy (see Table B.1.1). The result of a theoretical calculation reported by A. Gal [64] are also listed, where three components of CSB effect are individually presented; ΔT_{YN} is from a kinetic energy difference with the Σ mass difference, ΔV_C is from a change in the Coulomb effect by putting hyperons, and ΔV_{YN} is from YN CSB interactions. Unit is in keV.

hypernuclei	exp. data ΔB_Λ(g.s.) emulsion	reaction	calculated ΔB_Λ(g.s.)	ΔT_{YN}	ΔV_C	ΔV_{YN}
${}^{4}_{\Lambda}$He$-{}^{4}_{\Lambda}$H	$+350 \pm 60$	$+270 \pm 110$	$+226$	$+39$	-45	$+232$
${}^{8}_{\Lambda}$Be$-{}^{8}_{\Lambda}$Li	$+40 \pm 60$	-	$+49$	$+11$	-81	$+119$
${}^{9}_{\Lambda}$B$-{}^{9}_{\Lambda}$Li	-210 ± 220	-70 ± 240	-54	$+10$	-145	$+81$
${}^{10}_{\Lambda}$B$-{}^{10}_{\Lambda}$Be	-220 ± 250	$+40 \pm 210$	-136	$+3$	-156	$+17$

Bibliography

[1] G. A. Miller, A. K. Opper, and E. J. Stephenson, Ann. Rev. Nucl. Part. Sci. **56**, 253 (2006).

[2] S.A. Coon and R.C. Barrett, Phys. Rev. C **36**, 2189 (1987).

[3] M. Danysz and J. Pniewski, Phil. Mag. **44**, 348 (1953).

[4] M. Ukai *et al.*, Phys. Rev. C **77**, 054315 (2008).

[5] H. Tamura *et al.*, Phys. Rev. Lett. **84**, 5963 (2000).

[6] M. Ukai *et al.*, Phys. Rev. C **73**, 012501 (2006).

[7] D.J. Millener, Nucl. Phys. A **754**, 48c (2005).

[8] Y. Akaishi, T. Harada, S. Shinmura, and K. S. Myint, Phys. Rev. Lett. **84**, 3539 (2000).

[9] M. Jurić *et al.*, Nucl. Phys. B **52**, 1 (1973).

[10] D.H. Davis, Nucl. Phys. A **754**, 3c (2005).

[11] P. Dluzewski, K. Garbowska-pniwska, J. Pniwski, T. Tymieniecka, and P. Ciok, Nucl. Phys. A **484**, 520 (1988).

[12] T. Gogami *et al.*, arXive **nucl-ex**, 1511.04801v1 (2015).

[13] M. Bedjidian *et al.*, Phys. Lett. B **62**, 467 (1976).

[14] M. Bedjidian *et al.*, Phys. Lett. B **83**, 252 (1979).

[15] A. Kawachi, Doctoral Thesis, University of Tokyo (1997), unpublished.

[16] A. Esser *et al.*, Phys. Rev. Lett. **114**, 232501 (2015).

[17] D.H. Davis, Contemp. Phys. **27-2,91**, 116 (1986).

[18] M.M. Block *et al.*, Proceedings of the International Conference on Hyperfragments at St. Cergue, Switzerland, 1963 (CERN Scientific Information Service) **64-1** (1963).

[19] R.H. Dalitz and L. Liu, Phys. Rev. **116-5**, 1312 (1959).

[20] R. H. Dalitz and F. Von Hippel, Phys. Lett. **10**, 153 (1964).

[21] A. Nogga, H. Kamada, and W. Glöckle, Phys. Rev. Lett. **88**, 172501 (2002), and references therein.

[22] H. Tamura *et al.*, J-PARC proposal E13 "Gamma-ray spectroscopy of light hypernuclei", http://j-parc.jp/researcher/Hadron/en/pac_0606/pdf/p13-Tamura.pdf (2006).

[23] H. Tamura, M. Ukai, T.O. Yamamoto, and T. Koike, Nucl. Phys. A **881**, 310 (2012).

[24] T.O. Yamamoto *et al.*, Phys. Rev. Lett. **115**, 222501 (2015).

[25] A. Bamberger *et al.*, Nucl. Phys. B **60**, 1 (1973).

[26] T. Harada, Private communication (2006).

[27] K. Agari *et al.*, Prog. Theor. Exp. Phys. **2012**, 02B009 (2012).

[28] T. Takahashi *et al.*, Prog. Theor. Exp. Phys. **2012**, 02B010 (2012).

[29] R. Honda, K. Miwa, Y. Matsumoto, N. Chiga, S. Hasegawa, and K. Imai, Nucl. Instr. Meth. A **787**, 157 (2015).

[30] T. Fukuda *et al.*, Nucl. Instrum. Methods A **361**, 485 (1995).

[31] K. Shirotori *et al.*, Phys. Rev. Lett. **109**, 132002 (2012).

[32] S. Agostinelli *et al.*, Nucl. Instr. Meth. A **506**, 250 (2003).

[33] J. Myrheim and L. Bugge, Nucl. Instr. Meth. **160**, 43 (1979).

[34] J. Myrheim and L. Bugge, Three Dimentional Computer Program (TOSCA) for Non-Linear Electromagnetic Fields, RL-81-070557 (1982).

[35] M. Daum *et al.*, Eur. Phys. J. C **23**, 43 (2002).

[36] T. Iijima *et al.*, Nucl. Instr. Meth. A **453**, 321 (2000).

[37] T. Nagae *et al.*, Phys. Rev. Lett. **80**, 1605 (1998).

[38] K. Miwa *et al.*, Phys. Rev. C **77**, 045203 (2008).

[39] M. Moritsu *et al.*, Nucl. Phys. A **914**, 91 (2013).

[40] Y. Ichikawa *et al.*, Prog. Theor. Exp. Phys. **2014**, 101D03 (2014).

[41] H. Sugimura *et al.*, Phys. Lett. B **729**, 39 (2014).

[42] T. Koike *et al.*, Proc. 9th Int. Conf. on Hypernuclear and Strange Particle Physics (HYP2006), October 10-14, 2006, Mainz, Ed. by J. Pochodzalla and Th. Walcher, Springer , 25 (2007).

[43] T. Koike *et al.*, Nucl. Instrum. Methods A **770**, 1 (2014).

[44] E. Hull, R. H. Pehl, *et al.*, IUCF Ann. Rep. , 143 (1993).

[45] H. Outa *et al.*, Nucl. Phys. A **639**, 215c (1998).

[46] H. Outa *et al.*, Nucl. Phys. A **754**, 157c (2005).

[47] Y. Igarashi *et al.*, IEEE Trans. Nucl. Sci. **57**, 618 (2010).

[48] R. Honda and K. Miwa, Proceedings of 3rd International Workshop on New PhotonDetectors, PoS Press , 031 (2012).

[49] Y. Igarashi *et al.*, IEEE Trans. Nucl. Sci. **52**, 2866 (2005).

[50] O. Hashimoto and H. Tamura, Prog. Part. Nucl. Phys. **57**, 564 (2006).

[51] J. F. Ziegler, The Stopping and Range of Ions in Matter, avaliable via www at the URL:http://www.srim.org/ (1977).

[52] R. Dalitz and A. Gal, Annals Phys. **116**, 167 (1978).

[53] Y. Sasaki, Master thesis, Tohoku University (2013a).

[54] A. Sasaki, Master thesis, Tohoku University (2013b).

[55] K. Tanida, Doctoral thesis, University of Tokyo (2000).

[56] M. Ukai, Doctoral thesis, Tohoku University (2004).

[57] K. Hosomi, Doctoral thesis, Tohoku University (2013).

[58] G.P. Gopal. *et al.*, Nucl. Phys. B **119**, 362 (1976).

[59] M. May *et al.*, Phys. Rev. Lett. **51**, 2085 (1983).

[60] M.M. Nagels. *et al.*, Phys. Rev. D **12**, 744 (1975).

[61] P.M.M. Maessen. *et al.*, Phys. Rev. C **40**, 2226 (1989).

[62] Th. Rijken. *et al.*, Phys. Rev. C **59**, 21 (1999).

[63] E. Hiyama, M. Kamimura, T. Motoba, T. Yamada, and Y. Yamamoto, Phys. Rev. C **65**, 011301 (2002).

[64] A. Gal, Phys. Lett. B **744**, 352 (2015).

[65] H. Polinder, R. Haidenbauer, and U.-G. Meiβner, Nucl. Phys. A **779**, 244 (2006).

[66] D. Gazda and A. Gal, arXive **nucl-th**, 1512.01049v2 (2015).

[67] H. Tamura *et al.*, J-PARC proposal P63 "Gamma-ray spectroscopy of light hypernuclei II " (2016).

[68] Y. Fujiwara, Y. Suzuki, and C. Nakamoto, Prog. Nucl. Part. Phys. **58**, 439 (2007).

[69] K. Miwa *et al.*, J-PARC proposal E40 "Measurement of the cross section of Σp scatterings", http://j-parc.jp/researcher/Hadron/en/pac_1101/pdf/KEK_J-PARC-PAC2010-12.pdf (2010).

[70] S.N. Nakamura *et al.*, Phys. Rev. Lett. **110**, 012502 (2013).

[71] T. Gogami, Doctoral thesis, Tohoku University (2014).

[72] G.M. Urciuoli *et al.*, Phys. Rev. C **91**, 034308 (2015).

[73] T. Hasegawa *et al.*, Phys. Rev. C **53**, 1210 (1996).

[74] L. Tang *et al.*, Phys. Rev. C **90**, 034320 (2014).

[75] E. Hiyama *et al.*, Phys. Rev. C **80**, 054321 (2009).